UNIVERSITY OF SÃO PAULO
POLYTECHNIC SCHOOL

Marcos Vinicius Gil Silveira

Development and evaluation of performance-based design methodologies for reinforced concrete deep beams: experimental and numerical investigations

São Paulo

2023

MARCOS VINICIUS GIL SILVEIRA

Development and evaluation of performance-based design methodologies for reinforced concrete deep beams: experimental and numerical investigations

Revised version

Doctoral Thesis submitted to the Polytechnic School at the University of São Paulo to obtain the degree of Doctor of Science. Concentration area: Structural Engineering. Supervisor: Prof. Dr. Luís Antônio Guimarães Bitencourt Júnior (USP). Co-supervisor: Prof. Dr. Sreekanta Das (University of Windsor).

São Paulo

2023

Este exemplar foi revisado e corrigido em relação à versão original, sob responsabilidade única do autor e com a anuência de seu orientador.

São Paulo, 16 de Agosto de 2023

Assinatura do autor: Marcos Silveira

Assinatura do orientador: Roberto Bitencourt Jr.

Catalogação-na-publicação

Silveira, Marcos Vinicius Gil
Development and evaluation of performance-based design methodologies for reinforced concrete deep beams: experimental and numerical investigations / M. V. G. Silveira -- versão corr. -- São Paulo, 2023.
85 p.

Tese (Doutorado) - Escola Politécnica da Universidade de São Paulo. Departamento de Engenharia de Estruturas e Geotécnica.

1.Generative Tie Method 2.Strut-and-Tie Performance-Based Optimization 3.Topology Optimization 4.Generative Design 5.Large-scale experimental test I.Universidade de São Paulo. Escola Politécnica. Departamento de Engenharia de Estruturas e Geotécnica II.t.

Name: SILVEIRA, Marcos Vinicius Gil.

Title: Development and evaluation of performance-based design methodologies for reinforced concrete deep beams: experimental and numerical investigations.

Doctoral Thesis submitted to the Polytechnic School at the University of São Paulo to obtain the degree of Doctor of Science.

Approved in: 2023/07/28

Examination Board

Prof. Dr.	Joshua Woods
Institution:	Queen's University
Decision:	_____
Prof. Dr.	Miguel Fernández Ruiz
Institution:	Universidad Politécnica de Madrid
Decision:	_____
Prof. Dr.	Maurício de Pina Ferreira
Institution:	Universidade Federal do Pará
Decision:	_____
Prof. Dr.	Fernando Rebouças Stucchi
Institution:	Universidade de São Paulo
Decision:	_____
Prof. Dr.	Luís Antônio Guimarães Bitencourt Júnior
Institution:	Universidade de São Paulo
Decision:	_____

Acknowledgment

I would like to express my deepest gratitude and appreciation to the following individuals and organizations who have contributed significantly to the completion of this Ph.D. thesis:

First and foremost, I am indebted to my supervisors, Professors Dr. Luís Bitencourt Jr. and Dr. Sreekanta Das. Their constant encouragement, valuable guidance, and unwavering support throughout this research journey have been instrumental in shaping the outcome of this thesis.

I am honored to acknowledge the grants and funding support received, which played a crucial role in enabling the successful execution of this research. In particular, I am grateful to the Canadian grants and institutions, namely the Emerging Leaders in the Americas Program (ELAP) and the Natural Sciences and Engineering Research Council of Canada (NSERC). Additionally, I extend my appreciation to the Brazilian grants and institutions, including the Coordenação de Aperfeiçoamento de Pessoal de Nível Superior (CAPES) and the Conselho Nacional de Desenvolvimento Científico e Tecnológico (CNPq).

I would like to extend my sincere thanks to the technical staff members, Mr. Matthew St. Louis and Mr. Jerome Finnerty, as well as all my colleagues from Dr. Das's research group at the Structural Engineering Laboratory, University of Windsor. Their assistance, expertise, and friendship during the experimental program of this thesis were indispensable.

I extend my gratitude to the esteemed members of the Examination Board, Dr. Joshua Woods, Dr. Miguel Fernández Ruiz, Dr. Maurício de Pina Ferreira, and Dr. Fernando Rebouças Stucchi. Their willingness to dedicate their valuable time and expertise to evaluate and contribute to this research is deeply appreciated.

To my partner, Juliana Wagner, I am deeply grateful for her unwavering love, understanding, and patience throughout this challenging journey. Her support has been my rock, providing the strength and motivation to overcome obstacles and persevere.

Last but certainly not least, I would like to express my heartfelt gratitude to my family. To my parents, Luzia and Nivaldo, thank you for your unwavering belief in me and for instilling in me the values of hard work and dedication. To my brothers, Rafael and Nivaldo Jr., thank you for your constant support and encouragement. To my nephew, José Augusto, thank you for bringing joy and inspiration into my life. And to my aunts, Maria Lúcia and Alice, thank you for your love and encouragement.

Without the support and contributions of these individuals and institutions, this thesis would not have been possible. I am truly grateful for their presence in my life and their impact on my academic journey.

Resumo

Esta pesquisa apresenta uma exploração abrangente do projeto e otimização de vigas-parede de concreto armado por meio da aplicação de abordagens baseadas em desempenho. O Artigo I introduz o Método das Bielas e Tirantes Baseado em Desempenho (OBTBD) como um método alternativo para o projeto de vigas-parede com grandes aberturas (descontinuidades geométricas). Por meio de investigações experimentais e numéricas, o OBTBD é comparado com os Campos de Tensão Elastoplástico (CTEP) e o Método das Bielas e Tirantes (MBT) utilizando várias amostras. As conclusões evidenciam os resultados promissores do método proposto, demonstrando sua efetividade na otimização do uso de materiais e no aprimoramento do desempenho estrutural. O Artigo II apresenta o Método dos Tirantes Generativos (MTG) como uma solução alternativa para o projeto de vigas-parede com descontinuidades de carregamento, superando algumas limitações dos métodos convencionais. O MTG é um procedimento não linear que utiliza a Análise de Elementos Finitos (AEF) baseada em CTEP para gerar de forma iterativa layouts otimizados de armaduras para elementos de concreto estrutural (CE). Por meio de investigações experimentais em escala real, é validada a adequação do MTG para o projeto de vigas-parede com descontinuidades de carregamento, afirmando sua eficácia e confiabilidade na obtenção de um desempenho estrutural superior. O Artigo III apresenta uma avaliação detalhada de vigas-parede em escala real com descontinuidades geométricas projetadas utilizando o MTG. O estudo enfatiza a importância da seleção de parâmetros apropriados para o projeto de vigas-parede de concreto armado com o MTG, como o nível admissível de perda de resistência à compressão devido à atuação de tensões de tração elevadas no concreto. A análise comparativa demonstra que os espécimes projetados com o MTG superam o espécime projetado com o MBT (estudado no Artigo I), exibindo melhores índices de desempenho e ductilidade mais evidente. O Artigo IV explora a integração da Otimização Topológica e do MTG por meio de uma abordagem baseada em Design Generativo proposta para o projeto de vigas-parede de CE com descontinuidades geométricas. Simulações computacionais utilizando AEF e testes experimentais em escala real forneceram informações valiosas sobre estratégias de otimização, destacando a eficácia dos espécimes projetados com o MTG em termos de ductilidade e otimização de materiais. Os resultados sugerem o potencial do método baseado em Design Generativo para elementos estruturais de concreto com descontinuidades. Esta pesquisa faz uma contribuição significativa para o campo do projeto de vigas-parede de concreto armado, introduzindo metodologias práticas, inovadoras e orientadas

pelo desempenho. A pesquisa oferece soluções valiosas para aprimorar o desempenho estrutural e a eficiência no projeto de vigas-parede de CE.

Palavras-chave: Método dos Tirantes Generativos, Otimização de Bielas e Tirantes Baseada em Desempenho, Otimização Topológica, Ensaios experimentais em escala real, Design Generativo.

Abstract

This research comprehensively explores the design and optimization of reinforced concrete deep beams through the application of performance-based approaches. Research Paper I introduces the Strut-and-Tie Performance-based Optimization (STPBO) framework as an alternative method for the design of deep beams with large openings (geometric discontinuities). Through experimental and numerical investigations, the STPBO approach is compared with the Elastic-plastic Stress Fields (EPSF) and Strut-and-Tie (STM) methods using various specimens. The findings illustrate the promising outcomes of the proposed method, demonstrating its effectiveness in optimizing material usage and enhancing structural performance. Research Paper II presents the Generative Tie Method (GTM) as an alternative solution for designing deep beams with loading discontinuities, overcoming some limitations of conventional methods. The GTM is a nonlinear procedure that utilizes finite element analysis (FEA) based on EPSF to iteratively generate optimized reinforcement layouts for structural concrete (SC) members. Through extensive large-scale experimental investigations, the suitability of the GTM for designing deep beams with loading discontinuities is validated, affirming its efficacy and reliability in achieving superior structural performance. Research Paper III presents a detailed evaluation of large-scale deep beams with geometric discontinuities designed using GTM. The study emphasizes the significance of selecting appropriate parameters for reinforced concrete deep beam design with GTM, such as the admissible level of compressive strength loss due to high tensile strain acting in the concrete. The comparative analysis demonstrates that GTM-designed specimens outperform the STM-designed specimen (studied in Research Paper I), exhibiting improved performance ratios and enhanced ductility. Research Paper IV explores the integration of Topology Optimization and GTM through a proposed generative design framework for the design of SC deep beams with geometric discontinuities. Computational simulations using FEA and large-scale experimental testing provided valuable insights into optimization strategies, highlighting the efficacy of the GTM-designed specimens in terms of ductility and material optimization. The findings suggest the potential of the generative design framework for structural concrete members with discontinuities. This research significantly contributes to the reinforced concrete deep beam design field by introducing practical, innovative, and performance-driven methodologies. The research offers valuable solutions to enhance structural performance and efficiency in SC deep beam design.

Keywords: Generative Tie Method, Strut-and-Tie Performance-Based Optimization, Topology Optimization, Generative Design, Large-scale experimental test, Generative Design.

Table of contents

1. General Introduction

The design of structural concrete (SC) discontinuous members, known as D-regions, necessitates careful consideration owing to their unique characteristics. According to the commentary section of the current American Concrete Institute Building Code Requirements for Structural Concrete (ACI 318-19) [1], discontinuities in structural concrete members manifest in the stress distribution due to variations in the geometry of the member or the existence of concentrated loads or reactions. Discontinuities resulting from sudden alterations in geometry are referred to as geometric discontinuities. Structural elements exhibiting this type of discontinuity include elements with openings, beam-column joints, frame corners, shear walls, and deep beams. On the other hand, discontinuities arising from concentrated loads are known as loading discontinuities. Examples of structural members with this type of discontinuity include pile caps, corbels, and elements subjected to concentrated loads [1].

The primary approach employed for D-region design is the strut-and-tie method (STM). The methodology is based on the premise that D-regions can be analyzed and designed effectively using hypothetical pin-jointed trusses [1]. These trusses are composed of compressive and tensile elements connected by nodal regions. The use of the truss analogy in structural concrete design dates back to early 20th-century developments, exemplified by Ritter & Mörsch's model for shear beam design [2]. Reineck et al. [2] emphasize the historical significance of this approach within the structural concrete field. Distinguished SC design codes, such as the Canadian standard [3], ACI 318-19 [1], *fib* model code 2010 [4], and the Brazilian standard [5], incorporate provisions and guidelines specifically for the design of D-regions using the STM approach.

The STM has obtained significant attention in the design of SC D-regions in recent decades, particularly following the influential research conducted by Schlaich et al. [6]. An extensive presentation of numerous SC members designed using the STM approach is provided by Schlaich et al. [6]. Following that, numerous studies have been conducted regarding the application of the STM in the design of SC D-regions [7–19]. The case study proposed by Schlaich et al. [6] titled "*Deep beam with a large hole*" stands out for its intricate stress fields, warranting particular attention. Therefore, scaled-down model experiments were employed to investigate this model, as documented in the following references [7,15]. In this doctoral research, the examination of the aforementioned model is extended through an in-depth investigation utilizing experimental and numerical techniques across Research Paper I, Research Paper III, and Research Paper IV.

Despite extensive research and widespread adoption of structural design standards [1,3–5], the application of the STM presents a notable challenge in formulating idealized trusses. Consequently, researchers are actively engaged in investigating and developing frameworks that incorporate optimization techniques to aid engineers in the conceptual design of the equivalent truss employed in STM applications. According to Liang et al. [20], considerable attention has been devoted to the application of topology optimization (TO) and performance-based optimization (PBO) to achieve this objective. As described by Zhang et al. [21], TO is a mathematical methodology employed in engineering to optimize the distribution of materials within a specified design space. The application of Evolutionary Structural Optimization (ESO) and Bidirectional Evolutionary Structural Optimization (BESO) approaches to STM problems [22–25] involves the strategic insertion and/or removal of elements, combined with performance evaluation. By systematically selecting efficient elements within a discrete design domain, the load transfer path for an SC D-region can be progressively elucidated [20].

Notwithstanding the high popularity of the STM for designing D-regions, acknowledging the presence of alternative design approaches is of considerable importance. According to Ruiz and Muttoni [26,27], the Stress Fields Method (SFM) has demonstrated capability in addressing similar design challenges as the STM. While the STM utilizes discrete forces and employs a truss analogy to design and evaluate struts, ties, and nodes, the SFM analyzes stress distribution. The research conducted by Drucker [28] during the early 1960s, as emphasized by Muttoni et al. [29], significantly advanced the design of structural concrete members by developing stress fields using the Theory of Plasticity. Drucker [28] conducted an investigation on a simply supported beam, utilizing rigid-plastic constitutive models to derive discontinuous stress fields. Furthermore, alternative constitutive models within the SFM have been explored.

Ruiz and Muttoni [26] introduced the Elastic-Plastic Stress Field (EPSF), which incorporates primary stress field hypotheses and elastic-plastic constitutive models. Furthermore, they presented a practical methodology to develop stress fields or truss models using a nonlinear FEA solver named *jconc* (available in [30]). The development of the FEAsolver was undertaken in the same research to showcase the EPSF approach effectively. The formulation of *jconc* neglects the tensile strength of concrete, assuming a post-cracking state for concrete. An elastoplastic constitutive model and the Modified Compression-field Theory (MCFT) proposed by Vecchio and Collins [31] are employed to characterize the behavior of concrete elements. The formulation of the MCFT for the reduction in concrete's compressive strength caused by transverse tensile strains (cracking) substantially impacts the

outcomes obtained through *jconc* [27]. Finally, *jconc* employs truss elements to model the reinforcement bars, restricting them to experience only axial forces while utilizing an elastoplastic constitutive model.

The application of TO has garnered substantial attention within the context of the STM [20,32–34], specifically in aiding the designer in conceiving the equivalent trusses. Moreover, considerable attention has been given to exploring the potential of TO in supporting designers during the structural shape conception phase, as evidenced by previous investigations [35–39]. Notably, collaborative efforts between architecture and engineering have been recognized as pivotal in the construction industry, as emphasized by Beghini et al. [38]. The referred research proposes an innovative approach that employs a customized structural TO framework to facilitate the generation of integrated design ideas [38].

Generative Design (GD) has also emerged as a computer-aided creation approach in the domain of the construction design industry. According to Alsakka et al. [40], GD methods employ computational capabilities to generate alternative designs that satisfy a defined set of objectives and criteria. These criteria encompass various factors, including performance, materials, manufacturing techniques, and costs. As noted by Sivam [41], early investigations into GD were pioneered by Frazer in the early 1970s [42]. Shea et al. [43] state that GD systems aim to establish new design processes capable of producing unprecedented and feasible elements by effectively utilizing the current computing and manufacturing resources. Additionally, Shea et al. [43] describe the GD method as a collaborative partner in the design process, capable of generating design ideas in response to robust and rigorous computational models of design constraints and performance criteria.

According to Sun and Ma [44], GD entails the exploration of multiple design variants and the assessment of their performance. Unlike traditional optimization processes concentrating on a single optimal design, GD aims to generate various design solutions by manipulating multiple variants. Noteworthy studies in the construction industry addressing a diverse range of problems have been highlighted. Sydora & Stroulia [45] conducted investigations into the application of GD techniques in the field of interior design. Gan [46] focused on GD in the context of modular construction design. Gonzalez-Delgado et al. [47] achieved significant advancements in the structural design of wind turbines using GD. Zhang et al. [48] explored GD in the initial stages of residential building designs. Additionally, Caetano et al. [49] undertook a comprehensive literature review, critically examining the terminologies

surrounding computational design - including GD - incorporating multiple definitions proposed by various authors.

1.1 Aims and Objectives

The primary objective of this Ph.D. research is to develop and evaluate automated and performance-based design methodologies for structural concrete members with geometric and loading discontinuities. The proposal and evaluation of the Strut-and-Tie Performance-based Optimization (STPBO) framework as an alternative method for designing reinforced concrete deep beams with large openings [6] can be found in Research Paper I. Experimental and numerical investigations are conducted in large-scale specimens designed with the STPBO, the EPSF, the STM. Comparisons are performed between the material usage and structural performance of the specimens. Research Paper II introduces the Generative Tie Method (GTM) by demonstrating its application in designing deep beams with loading discontinuities. The GTM is a nonlinear procedure that employs iterative FEA to generate the reinforcement layout of SC members. Research Paper II reveals a comprehensive performance evaluation of GTM-designed deep beams with loading discontinuities [50], highlighting the importance of selecting appropriate design parameters.

Research Paper III focuses on the application of GTM for designing the deep beam with a large opening, which was originally proposed by Schlaich et al. [6] and investigated in Research Paper I. Furthermore, Research Paper III presents a comparative analysis between GTM-designed specimens and the STM-designed specimen from Research Paper I, highlighting enhanced performance ratios and improved ductility in the GTM-designed specimens. Moreover, Research Paper IV explores the integration of TO and the GTM through the development of a GD framework for the design of structural concrete deep beams with loading and geometric discontinuities. To evaluate the effectiveness of the proposed GD framework, computational simulations, and large-scale experimental testing are conducted. The results demonstrate promising outcomes, presenting the potential of this integrated approach for the design of complex-shaped SC members.

Based on the aims outlined above, the core objectives of this thesis are as follows:

- Develop automated and performance-based design methodologies for structural concrete members with geometric and loading discontinuities.

- Introduce and demonstrate the application of the Strut-and-Tie Performance-based Optimization framework as an alternative method for designing reinforced concrete deep beams with large openings.
- Evaluate the potential of the STPBO through comprehensive experimental and numerical investigations, allowing for a comparison of material utilization and structural performance among specimens designed using various methodologies, including EPSF and STM.
- Introduce and demonstrate the application of the Generative Tie Method for designing deep beams with loading discontinuities.
- Evaluate the performance of GTM-designed deep beams with loading discontinuities through comprehensive experimental and numerical investigations, emphasizing the importance of selecting appropriate design parameters.
- Apply GTM for designing deep beams with large openings and compare the results with the STM-designed specimen, focusing on performance ratios and ductility.
- Investigate the integration of TO and GTM by proposing a GD framework capable of designing structural concrete deep beams that account for both loading and geometric discontinuities.
- Conduct computational simulations and large-scale experimental testing to evaluate the effectiveness of the proposed GD framework.

1.2 Thesis Overview

This doctoral thesis follows a paper-based structure presenting the research as a series of self-contained papers that can be read independently. However, together they form a cohesive body of work that advances the understanding of the design and optimization of reinforced concrete deep beams using performance-based design methodologies. The purpose of this section is to establish connections between the four research papers included in this thesis, each of which explores different aspects of the topic.

In Research Paper I, STM and SFM are explored in the design of specimens inspired by the "*Deep beam with a large hole*" example from [6]. The first specimen (SIa) was designed according to the truss model proposed by [6]. The STM guidelines provided both by [1] and by [6] were followed with the help of the software CAST [18]. The specimen named SIb was designed under the EPSF approach. The three steps approach presented in [26] and later explored in [27] was followed. A novel approach is proposed associating performance-based

optimization, STM, and EPSF called Strut-and-Tie Performance-based Optimization (STPBO). The design of the last specimen (SIc) was done as an example of the STPBO application. A full-scale experimental program was conducted on SIa, and the test data was collected using the digital image correlation (DIC) technique. Numerical simulations were performed on the tested specimen using a proposed FEA technique that integrates the MCFT [31] with Damage Theory. The validation of this numerical approach against experimental data was carried out, following which FEA predictions were conducted. A comparative analysis of the behavior of the three specimens is presented based on these simulations.

Research Paper II presents a detailed proposal of a method to design structural concrete members named the Generative Tie Method (GTM). The proposed framework is based on a nonlinear process, which uses FEA results to make design decisions. The FEA strategy used in the GTM is based on the EPSF approach proposed by [26,27]. The adopted FEA solver, named *jconc* (available in [30]), uses the main premises of the SFM and also the loss of compressive strength prediction model from the MCFT [31]. Four deep beams with the main geometrical characteristics from the specimens studied in [50–52] were designed with the help of the GTM. A large-scale experimental investigation was carried out around the performance of these four specimens. Birrcher et al. [51] suggested a minimum web reinforcement ratio of 0.3% for deep beams to improve the cracking control, deviating from the ACI recommendation of 0.25% [1]. Experimental results from Research Paper II demonstrated that the allowed cracking level can be controlled with the help of GTM.

Research Paper III presents an evaluation of the deep beams examined in Research Paper I, employing the GTM proposed in Research Paper II. The FEA approach used in Research Paper I was improved by the incorporation of the bond-slip model from the *fib* Model Code 2010. The importance of selecting appropriate design parameters within the GTM is emphasized for achieving ductile behavior. Comparisons between the specimens investigated in Research Paper III and those in Research Paper I revealed that GTM-designed specimens exhibited superior ductility and efficient material usage compared to the STM-designed deep beam.

Research Paper IV explores and advances the design of RC deep beams through a proposed GD framework that combines TO and the GTM developed in Research Paper II. Four distinct specimens are generated by applying different levels of optimization and GTM parameters to the "*Deep beam with a large hole*" example proposed by Schlaich et al. [6]. The effectiveness of this approach is thoroughly examined through computational simulations using

FEA and large-scale experimental testing. Performance comparisons using GD techniques are conducted among optimized large-scale specimens, as well as the specimens investigated in Research Paper I and Research Paper III. The results highlight the promising potential of integrating TO and the GTM within the GD framework, providing significant advancements in designing complex-shaped structural concrete members.

In the thesis, every research paper is structured with dedicated sections, including an abstract, keywords, a list of abbreviations, an introduction, materials and methods, discussions, conclusions, and a reference list. However, the references utilized in the thesis sections, namely General Introduction, Thesis Overview, and General Conclusions, are consolidated and presented in the References section. The specimens examined in each research paper are designated "S" followed by the corresponding research paper number in Roman numerals and concluded with a letter tag. For instance, "SIVa" denotes the first specimen investigated in Research Paper IV. Figure 1 illustrates the organizational arrangement of the specimens investigated within the thesis.

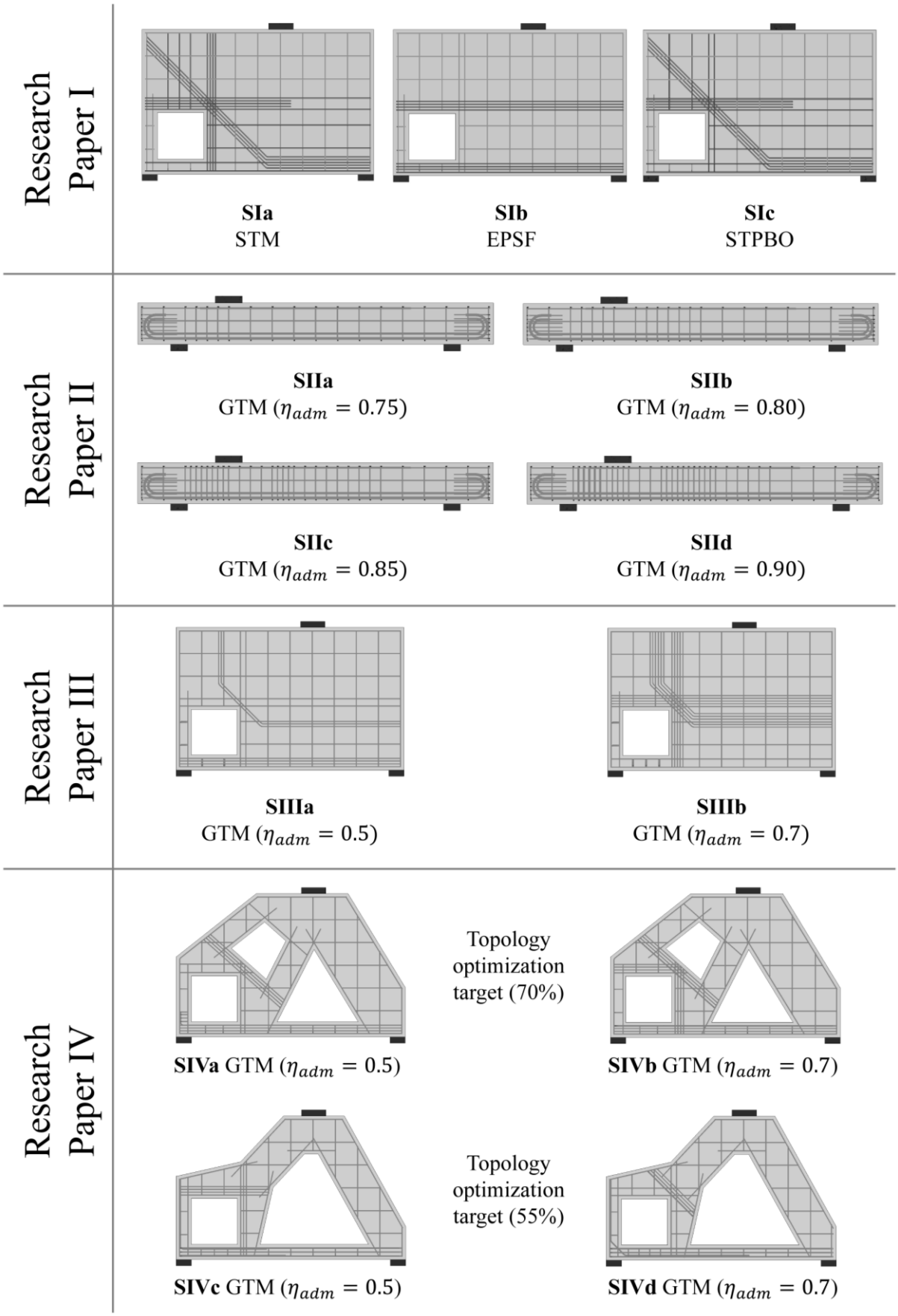

Figure 1 – Schematic representation of the analyzed specimens in the present research.

2. Research Paper I

This chapter is presented in the format of a journal paper. The following paper entitled "*A performance-based optimization framework applied to a classical STM-designed deep beam*" [32] was published in the Elsevier Structures Journal. Research Paper I can be accessed via the following link https://doi.org/10.1016/j.istruc.2022.05.035.

Structures 41 (2022) 488–500

Contents lists available at ScienceDirect

Structures

journal homepage: www.elsevier.com/locate/structures

A performance-based optimization framework applied to a classical STM-designed deep beam

Marcos V.G. Silveira [a], Luís A.G. Bitencourt [a,*], Sreekanta Das [b]

[a] Dept. of Structural and Geotechnical Engineering, University of São Paulo, São Paulo, SP 05508-010, Brazil
[b] Dept. of Civil and Environmental Engineering, University of Windsor, Windsor, ON N9B 3P4, Canada

ARTICLE INFO

Keywords:
Strut-and-tie method
Stress fields method
Strut-and-tie performance-based optimization
D-regions
Deep beam
Digital image correlation
Large-scale test

ABSTRACT

The outcomes of experimental and numerical investigations on the design of a classical deep beam with a large opening are presented in this paper. Two structural members were designed using the strut-and-tie method (STM) and the elastic–plastic stress fields method, respectively. In this study, a performance-based optimization framework, called strut-and-tie performance-based optimization, was developed. The method and its application are presented in this paper. The method applies a performance-based optimization process in an STM-designed structural member. The finite element method was used to measure the performance along the optimization process. A large-scale experimental test was conducted on the first specimen. The modified compression-field theory (MCFT) and the digital image correlation technique were used to investigate the failures of the tested specimen. In addition, a numerical simulation strategy that combines damage theory with MCFT was used. The numerical results showed good agreement with the experimental results of the STM-designed specimen. Finally, the same numerical approach was utilized to predict the behavior of the other two members. Comparisons in terms of the use of materials and structural performance demonstrated that the proposed method for the design of deep beams is promising.

1. Introduction

The presence of discontinuous regions (also known as D-regions) in some structural concrete members has led the structural codes and standards to recommend specific approaches to their design. Typical examples of D-regions are pile caps, beam-column joints, frame corners, corbels, deep beams, holes, and support regions. According to the current ACI-318 code [1], the strut-and-tie method (STM) can be used as an alternative to design structural members with D-regions since their complex behavior cannot be described by the classical Euler-Bernoulli beam theory (see reference [2]).

The STM considers the performance of an equivalent truss to study the behavior of discontinuous regions. In this truss analogy, the elements under compression are called struts and are usually made of concrete. In addition, the role to sustain the tension stresses is assigned to the ties and the connections between struts and ties are called nodes. Reineck [3] highlights that the truss analogy has been used since the beginning of structural concrete (SC) developments. Evidence of that is a model based on the truss analogy proposed by Ritter & Mörsch for the design of beams under shear (early 20th century) [3]. According to Ruiz & Muttoni [4], STM is based on the lower-bound limit of the theory of plasticity [5].

The STM has gained great attention for the design of SC D-regions over the last decades, especially after Schlaich et al. [6]. This special report presented a wide range of examples of SC members designed by STM. The case named *"Deep beam with a large hole"* [6] is explored in this paper. Well-conducted experimental investigations of STM-designed members can be found in the literature [7–15]. The "*Deep beam with a large hole*" firstly proposed by Schlaich et al. [6] was experimentally explored through scaled-down models by some authors [7,15]. Other remarkable contributions to the development of the STM theory can be found in references [16–21]. However, the application of the truss concept depends on the experience of the designers. Over the last two decades, various studies have been conducted for developing consistent approaches for generating truss models.

The use of topology optimization (TO) and performance-based optimization (PBO) to accomplish this goal has received considerable attention. As stated by Liang et al. [22], the systematic elimination of inefficient materials from a known discrete design domain can progressively reveal the load transfer path for an SC D-region. In this context, the authors propose a method able to help in the conception of

* Corresponding author.
E-mail address: luis.bitencourt@usp.br (L.A.G. Bitencourt).

https://doi.org/10.1016/j.istruc.2022.05.035
Received 14 March 2022; Received in revised form 25 April 2022; Accepted 9 May 2022

Nomenclature

Abbreviations and Symbols	Description
3DCP	3D concrete printing
BESO	Bidirectional evolutionary structural optimization
CCC	Nodes subjected to compressive stress in all directions
CCT	Nodes subjected to compressive stress in two directions and tensile stress in the other direction
CFE	Coupling finite element
CST	Constant strain triangle
CTT	Nodes subjected to compressive stress in one direction and tensile stress in the other two directions
DIC	Digital imagen correlation
D-regions	Discontinuous regions
EPSF	Elastic-plastic stress fields
ESO	Evolutionary structural optimization
FE	Finite element
FEA	Finite element analysis
LVDT	Linear variable differential transformer
MDR	Minimum distributed reinforcement
NL-FEA	Nonlinear finite element analysis
MCFT	Modified compression-field theory
OD	Optimization domain
PBO	Performance-based optimization
RC	Reinforced concrete
SC	Structural concrete
SFM	Stress fields method
STM	Strut-and-tie method
STPBO	Strut-and-tie performance-based optimization
TO	Topology optimization
TTT	Nodes subjected to tensile stress in all directions
$f_c^{'}$	Specified concrete compressive strength
f_{c2max}	Actual compressive strength according to the MCFT
f_{cd}	Design value of concrete compressive strength
f_{yd}	Design value of the reinforcement yield strength
f_y	Specified reinforcement yield strength
P_{cra}	Applied load when the first measurable crack (0.1 mm of width) appears
P_{cru}	Applied load when concrete is crushing
P_d	Design load or factored load
PI	Performance index
P_k	Service load
P_{STM}	Theoretical load capacity according to the STM
P_u	Ultimate or maximum applied load
P_y	Applied load when reinforcement reaches the yielding
W_0	Total weight of reinforcement in the initial model
W_i	Total weight of reinforcement in the analyzed model
β_i	The binary variable used to control the rebar stress level in the optimized solutions
ε_1	Principal tensile strain
$\varepsilon_{1\,exp}$	Experimental principal tensile strain
λ	Reinforcement stress safety factor
σ_{ij}	Maximum stress acting on the rebar in the analyzed model
σ_{0j}	Maximum stress acting on the rebar in the initial model
σ_{adm}	Admissible reinforcement stress

strut-and-tie truss-like models, in which the goal of minimizing material quantity is controlled by displacement requirements. As more material is removed, the structural members become susceptible to higher displacements.

The formulation of TO under the evolutionary structural optimization (ESO) and bidirectional evolutionary structural optimization (BESO) approaches [23–26] applied to STM problems is often governed by the insertion and/or removal of elements and measurement of resultant performances. Based on the relative level of stress, elements with low levels of stress have their stiffness contribution decreased on the subsequent step. However, the reverse can also happen with elements that are highly necessary for load carrying. This iterative process can be guided by the performance index (*PI*) [22]. The choice of *PI* and consequently the way to calculate its variables are very important tasks on the PBO application (see [27,28]). The variables required for the calculation of *PI* are usually obtained from finite element analyses (FEA). Although TO and PBO have been widely explored in the design of SC members, the optimized shapes produced by them have been criticized from a practical engineering point of view. However, according to Jewett and Carstensen [29], due to emerging concrete construction technologies, the classic way to build and design RC members has been reviewed. Further studies regarding the use of emerging concrete technologies can be found in the following publications [13,30–32].

Even though ACI-318 [1] and most of the SC codes and standards around the world recommend the use of STM to design D-regions, there are other methods available. According to Ruiz & Muttoni [4], the stress fields method can also produce similar outcomes from the STM. Both methods were initially developed based on the lower-bound theorem of plasticity. The STM uses discrete forces (truss analogy) to design and check struts, ties, and nodes, whereas the stress fields method deals with the stresses in 2D or 3D elements.

In the current study, applications of both STM and SFM are investigated for designing specimens inspired by the "*Deep beam with a large hole*" proposed by Schlaich et al. [6]. The STM guidelines provided by ACI-318 [1] and by Schlaich et al. [6] are both followed with the help of the software named *CAST* [19] for the design of the first specimen (SI.a). The EPSF approach proposed by Ruiz & Muttoni [4] and later explored by Muttoni et al. [33] is followed in the design of SI.b. Finally, the current study proposes a novel approach called strut-and-tie performance-based optimization (STPBO) method. This framework incorporates PBO, STM, and EPSF. The last specimen (SI.c) is designed as an example of the STPBO application.

A full-scale experimental program is conducted on the specimen SI.a and the test data are collected using the digital image correlation (DIC) technique. The experimental principal tensile strains extracted from DIC are used to check the concrete compressive strength from the MCFT perspective [34]. The main goal is to use reliable experimental results for the calibration of a numerical model based on nonlinear finite element analysis (NL-FEA). Once the numerical model is calibrated, FE predictions are conducted and comparisons between the behavior of the three specimens are undertaken. The outcomes are presented in this paper.

2. Design of the specimens

Schlaich et al. [6] presented several design examples using the strut-and-tie method (STM). The three specimens studied in this research were inspired by the "*Deep beam with a large hole*" example [6]. The specimens were scaled down by the factor of 0.4 by the length and by the height. A scale factor of 0.6 was used for the width. The geometry of the three specimens is illustrated in Fig. 1.

The design load (P_d) was scaled down from the original model [6] ($P_{d_o} = 3000kN$). As the stress generated by the point load depends on the length and the width, the design load for the scaled-down specimen can be defined by $P_d = 0.4 \times 0.6 \times P_{d_o} = 720kN$. The equation 5.3.1a from ACI-318 [1] is used to represent the load combination, which means that the service load (P_k) is taken as 514.3 kN. The specified concrete compressive strength ($f_c^{'}$) adopted on the design was *40 MPa*. The

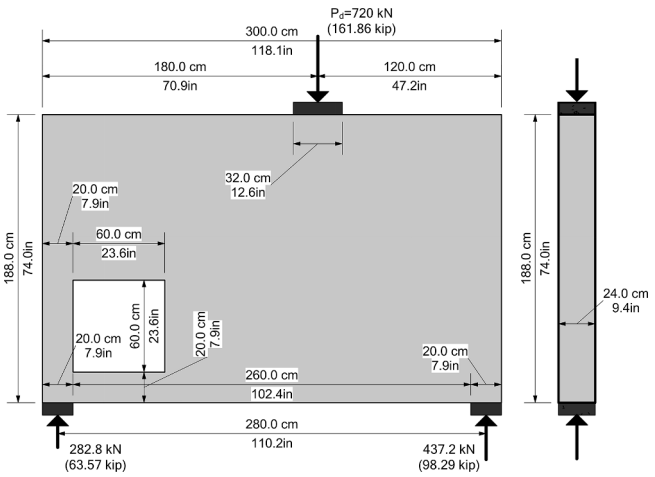

Fig. 1. Geometry of the specimens.

maximum diameter of the coarse aggregates adopted was 12.7 mm (1/2 in). The reinforcement cage was built by 10 M of 400 W grade [35,36] with a specified yield strength of 400 MPa (f_y). All the specimens are designed in accordance with ACI-318 [1] in theoretical design conditions. This means that the strength reduction factors, as well as the factor to represent the effective concrete strength under sustained compression (0.85), are considered in the design of the specimens. However, in order to have fair comparisons between theoretical and experimental results the partial factors are removed in section 4. Furthermore, the strengths of materials are updated in section 4 based on experimental results. Thus, the strength values obtained from the experimental program without safety factors are used in the calculation of the theoretical load capacity according to the STM (P_{STM}).

2.1. Design of SI.a using strut-and-tie method

Two methods were applied to obtain the truss-like model. Fig. 2 presents the results for both methods. The blue color represents compression the and the red color represents tensile stresses. Fig. 2a) shows the results of the truss-like TO approach called *LayOpt* [37]. The number of iteration steps and the simplification parameter used were 40 and 46%, respectively. No biased optimization was expected since the ratio between tensile and compression stress was set to one. A simplified truss model proposed by Schlaich et al. [6] is overlapping (black lines) the truss model obtained from *LayOpt* in Fig. 2a). An elastic stress fields investigation was conducted on the studied specimen in order to have a different view of the problem. Fig. 2b) shows the stress fields obtained from a linear elastic FEA using *jonc* [38]. About 4000 constant strain triangle (CST) finite elements with the modulus of elasticity of 30 GPa were used. Another truss model also proposed by Schlaich et al. [6] is overlapping (black lines) the linear elastic stress fields in Fig. 2b).

The combination of the truss-like TO approach of *LayOpt* [37] with the linear elastic FEA conducted in *jconc* [38] converges to the final model adopted by Schlaich et al. [6]. According to Schlaich et al. [6], the merger of the two trusses appears to be better than either of them. Finally, the truss model adopted in the current study is the same adopted by Schlaich et al. [6]. The adopted design truss is modeled on the *CAST* software [19,39,40] (Fig. 3).

The design of the specimen was completed using the recommendations from ACI-318 [1] (Chapter 23). All the specimens studied in this paper have surrounding cages satisfying the minimum distributed reinforcement (MDR) established by ACI-318 [1]. The designed MDR cages for the three specimens were composed of two layers (one for each deep face of the beam) of 10 M 400 W rebar [35] spaced by 291 mm (11.5 in). Table 1 shows the stress limit for each of the various STM components calculated according to ACI-318 [1].

The designed reinforcement layout of specimen SI.a is presented in Fig. 4. The MDR is depicted in this figure in a lighter shade in contrast to the main ties. All the reinforcement bars in the test specimen were bent and hooked according to the Canadian standard [36]. The anchorage for each tie was designed using clauses 23.10 and 25.4 from ACI-318 [1]. The reinforcement detailing of N04, N05, and N09 was done in accordance with Klein [41] and section 23 from ACI-318 [1]. Fig. 5 presents a side view and a top view of the N04 nodal region. The details presented in Fig. 5 were also adopted for nodes N09 and N05.

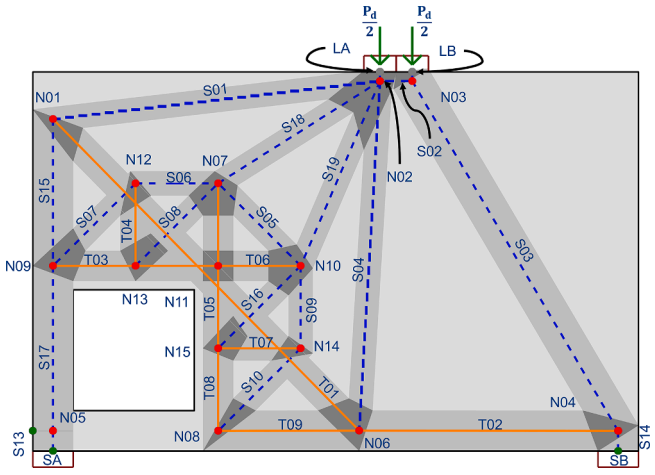

Fig. 3. STM truss modeled in *CAST* software and adopted on the design of SI.a.

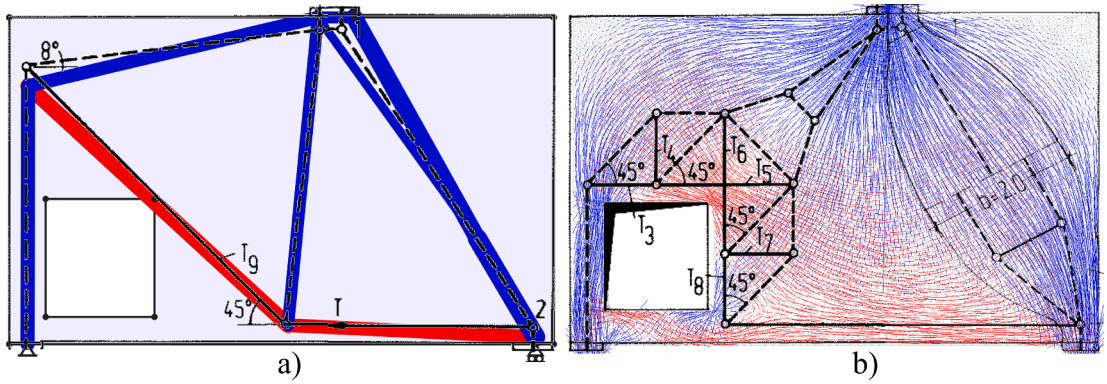

Fig. 2. Strut-and-tie model conception: a) truss-like topology optimization through *LayOpt* [37] overlapped by one of the trusses proposed by Schlaich et al. [6]; b) elastic stress fields obtained by linear elastic analysis through *jconc* [38] overlapped by another truss proposed by Schlaich et al. [6].

Table 1
Design stress limit of STM elements according to ACI-318 [1].

STM Type	Strength Reduction Factor	Effectiveness Factor	Stress Limit (MPa)
Nodes CCC	0.75	0.850	25.5
Nodes CCT	0.75	0.680	20.4
Nodes CTT or TTT	0.75	0.510	15.3
Boundaries struts	0.75	0.850	25.5
Internal struts	0.75	0.638	19.1
Reinforcement ties	0.75	1.000	300.0

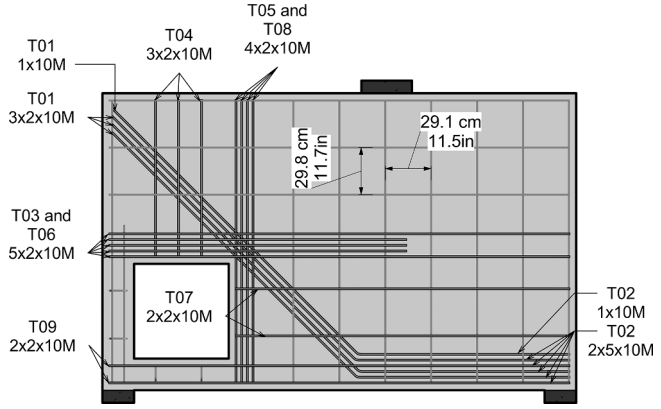

Fig. 4. Reinforcement detailing for SI.a.

2.2. Design of SI.b using elastic–plastic stress fields

Ruiz & Muttoni [4] developed a 2D FE-based software using the main stress fields hypotheses and elastic–plastic constitutive models [38]. In the software formulation, the steel reinforcements are represented by truss elements (only axial deformation is allowed) and can be considered elastic or elastic–plastic. The concrete is represented by constant strain triangle (CST) finite elements and its tensile strength is neglected, assuming that concrete does not share any tensile stress after cracking. The reduction in the concrete compressive strength due to the effects of transverse tensile strains is accounted for by the modified compression-field theory (MCFT) [34]. Eq. (1) was adapted from [34]. In Eq. (1), f'_c is the concrete compressive strength, usually determined through the standard cylinder test [42]. In Eq. (1), f_{c2max} is the actual compressive strength after the weaking and softening of concrete caused by the principal transverse tensile strain (ε_1). Thus, the concrete compressive strength and stiffness for each analysis step are calculated based on the principal transverse tensile strain (ε_1) obtained from the previous step. The constitutive models of concrete and reinforcement bars adopted in the referred FEA software (*jconc*) can be found in more detail in Ruiz & Muttoni [4].

$$f_{c2max} = \frac{f'_c}{0.8 + 170 \times \varepsilon_1} \leq f'_c \tag{1}$$

The design approach named elastic–plastic stress fields (EPSF) was proposed by Ruiz & Muttoni [4] and can be seen as a three-step procedure. The first one is the FEA on the first trial model. The first trial reinforcement layout can be defined using the experience of the designer and following the MDR requirements. In the second step, the user can develop a strut-and-tie model and then uses the forces obtained in the first step to design the components. From the EPSF perspective, the designer can use the stress obtained from the first FEA and update the reinforcement area in such a way that the maximum stress acting on the rebar in the analyzed model (σ_{ij}) remains under the design value of the reinforcement yield strength (f_{yd}). The third step is to check the

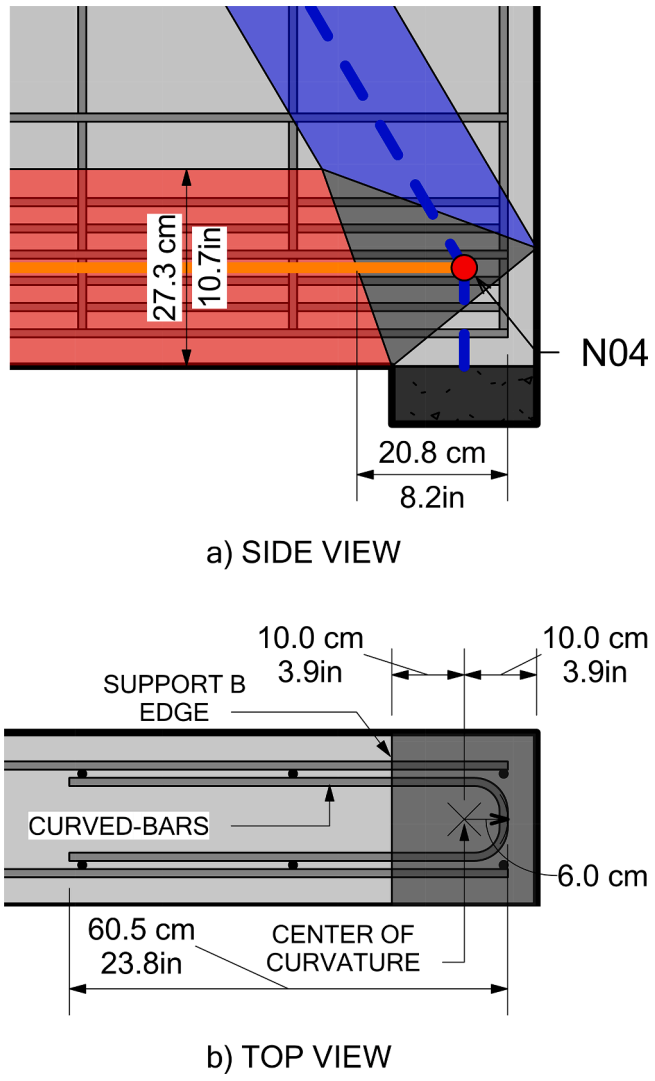

Fig. 5. Reinforcement detailing of node N04.

reinforcement layout, using the elastic–plastic constitutive model for the rebar and the MCFT for the concrete.

This procedure was applied to the second deep beam of the current study, SI.b. Fig. 6 shows the reinforcement layout obtained from the application of the EPSF. The reinforcement bars included by the EPSF approach are depicted in a darker tone of gray than the MDR (Fig. 6). The reinforcement detailing of the nodal regions above the supports and the upper left corner of the hole was adopted in SI.b similar to that

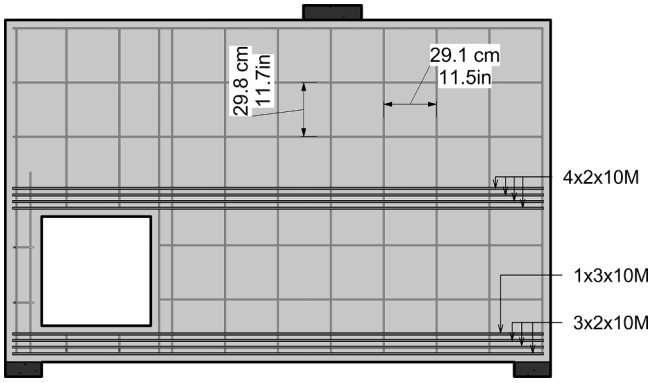

Fig. 6. Reinforcement detailing for SI.b.

shown in Fig. 5.

2.3. Strut-and-tie performance-based optimization (STPBO)

As mentioned earlier, PBO and TO have been widely used by structural designers to conceive strut-and-tie models. However, the application of PBO in this paper is based on the structural performance of members designed using STM. Hence, the approach presented herein is named the Strut-and-tie performance-based optimization (STPBO). According to ACI-318 [1], the MDR helps to provide a ductile behavior, and to avoid shrinkage and temperature undesirable effects in SC members. However, the inclusion of the MDR after the STM design process can generate over-designed reinforcement layouts. For this reason, the PBO application is made on the member already designed by the STM aiming to take advantage of the mandatory use of the MDR. Consequently, no optimization is applied to concrete elements and the MDR cage in the proposed approach. Finally, it is important to mention that the MDR requirements and the checks conducted in the STM design process regarding the struts and nodal regions are maintained.

The process proposed here considers the optimization of the reinforcement cage, which has a negligible influence on the specimen deflection. Thus, instead of aiming to minimize the displacements [13,22,26,29,31,43–46], the present process aims at maximizing the maximum stress. The increase of the maximum stress in the rebar can represent a more homogenous stress distribution in the reinforcement cage. However, the reinforcement stress cannot be deliberately increased, hence the optimization process needs to control it. Therefore, the maximum admissible reinforcement stress parameter (σ_{adm}) was created. This value must be chosen by the designer and shall be lower than the design value of the reinforcement yield strength (f_{yd}), as presented in Eq. (2). The reinforcement stress safety factor (λ) influences the performance index (*PI*), which is defined by Eq. (3).

$$\sigma_{adm} = \lambda \times f_{yd} \lambda \leq 1 \tag{2}$$

$$PI = \frac{\sigma_{ij} W_0}{\sigma_{0j} W_i} \beta_i \tag{3}$$

In Eq. (3), σ_{0j} is the maximum stress acting on the reinforcement bars in the initial model (STM and MDR). The maximum stress acting in the rebar of the analyzed model is represented by σ_{ij}. W_0 and W_i are the total weight of reinforcement in the initial model and the analyzed model, respectively. Variable β_i was created to control the optimized solutions in terms of rebar stress level. Eq. (4) expresses β_i as a fuction of σ_{adm}.

$$\beta_i = \begin{cases} 1, \sigma_{ij} \leq \sigma_{adm} \\ 0, \sigma_{ij} > \sigma_{adm} \end{cases} \tag{4}$$

Thus, when the maximum stress acting in the rebar in the analyzed model (σ_{ij}) overcomes the admissible reinforcement stress σ_{adm}, *PI* is set as 0 (zero). Until then, β_i is set to 1 (one) and does not change the value of *PI*.

To summarize, the STPBO method aims at maximizing *PI* presented in Eq. (3), which leads to minimizing the reinforcement weight (W_i) and maximizing stress on the rebar (σ_{ij}), yet keeping this value under σ_{adm} (Eq. (2)). Fig. 7 presents the flowchart of the STPBO approach. Note that materials properties and the loads must be used in design conditions. Therefore, the main steps of this approach can be summarized as:

1) *STM design:* The designer adopts a strut-and-tie model. The various optimization processes presented above can be used along with the strut-and-tie model. The choice of the truss-like model could be decisive to cover some key points [4,33]. One of them is the absence of the inclined reinforcement placed on the upper-right corner of the hole, as given in the strut-and-tie model proposed by Schlaich et al. [6].

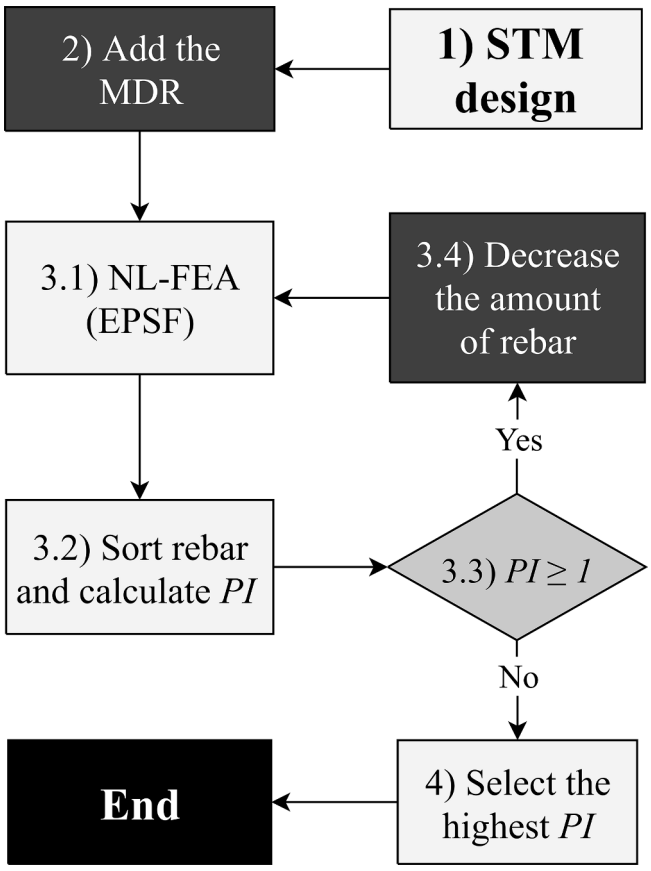

Fig. 7. Flowchart of the proposed Strut-and-tie performance-based optimization (STPBO).

2) *Add the MDR:* This step aims at covering the minimum distributed reinforcement (MDR). Regardless of the STM reinforcement layout, the deep beam reinforcement detailing must include the MDR. Nonetheless, MDR is required by the structural codes and standards to prevent shrinkage and temperature effects besides avoiding brittle failures. In this research, the MDR for the entire set of specimens was designed according to ACI-318 [1] (see section 2.1).
3) *Iterative process:* This step was divided into four sub-steps. For the first one (sub-step 3.1. NL-FEA by EPSF) an NL-FEA is required. The *jconc* solver [38] requires just a few parameters with a clear physical meaning. However, the implementation of the main hypothesis of the SFM and the use of the MCFT [34,47,48] to treat the loss of the concrete compressive strength due to transversal tensile strains, led to a satisfactory level of accuracy, as presented in references [4,33,49]. Based on the accuracy, quickness, simplicity, and compatibility with structural engineering practical problems, the *jconc* was assigned to be the NL-FEA tool on the STPBO approach proposed herein. Furthermore, the choice of using *jconc* [4,33] to measure the performance of the element should overcome the three first limitations presented by Brena & Morrison [49]. More information about the numerical strategy used by *jconc*, can be found in the previous section (2.2).

Sub-step 3.2 organizes all the reinforcement bars (trusses FEs) that belong to the same physical rebar (continuous reinforcement) together. After that, the present operation sorts all the physical reinforcement bars by the maximum stress along its length. To finish this sub-step, *PI* is calculated to be used in the next step. The logical test presented on the 3.3 sub-step was created to monitor the optimization efficiency. If the value of *PI* (Eq. (3)) is greater than or equal to 1 (one), sub-step 3.4 is activated. Otherwise, the entire process is ended through the completion

of step 4. The 3.4 sub-step is responsible for reducing the number of rebar into the most underused reinforcement position. Basically, sub-step 3.4 selects the rebar position subjected to the lowest stress belonging to the optimization domain (OD) and decreases its amount. Although this change must be updated in the finite element mesh file, no re-meshing is required, since the algorithm is not able to create new reinforcement bars. However, a new NL-FEA is required afterward. This loop is repeated, changing the *PI* until σ_{max} overcomes σ_{adm}, switching *PI* to zero.

4) *Select the best PI:* This process is triggered to select the maximum value of *PI*. Therefore, by the end of the flowchart given in Fig. 7, a new design model with less reinforcement consumption, and better rebar stress distribution is expected.

2.3.1. Design through the STPBO: SI.c

To illustrate the STPBO method, an application was carried out using specimen SI.a as the initial model. Design values (f'_c, f_y, and P_d), the geometry of the specimen, MDR, corner reinforcement, and boundary conditions were kept the same from specimen SI.a. In order to ensure the presence of the MDR and the corner reinforcements, these reinforcement bars were blocked on the optimization process. Fig. 8 shows the reinforcement bars that were part of the optimization domain (OD) in red.

A simple rule was followed to prioritize the reduction in the number of rebar on existing reinforcement positions to one rebar before they are eliminated completely. Table 2 resumes the optimization problem definition. Specimen SI.c was designed according to STPBO by adopting σ_{adm} equal to 300 MPa, which corresponds to $\lambda = 1$ in Eq. (2).

Fig. 9 shows the progress of *PI* during the optimization. The number of iterations coincides with the number of reinforcement bars removed. FEA showed that the maximum stress acting on the rebar in the analyzed model (σ_{ij}) increased beyond 300 MPa (σ_{adm}), once all reinforcement in the R4 position was removed (iteration 12). That resulted in a *PI* equal to zero, ending the optimization process. The highest *PI* was then the one obtained at iteration 11. Therefore, specimen SI.c used 111.0 kg of reinforcements and reached 299.0 MPa of σ_{ij}, hence, reaching a *PI* equal to 1.47. The reinforcement layout of SI.c is presented in Fig. 10. For the reinforcement layers without labels in this figure, two 10 M reinforcement bars were used (one rebar per deep beam face). The reinforcement detailing of the nodal regions above the supports and the upper left corner of the hole was adopted in SI.c similar to that shown in Fig. 5. More information about the design and reinforcements detailing for all specimens studied in this research can be found in the Supplementary material. It should be highlighted that besides *jconc* [4,38], a BIM-based (Building information modeling) software [50] was used to obtain the reinforcement weight, to facilitate the calculation of the performance index (*PI*).

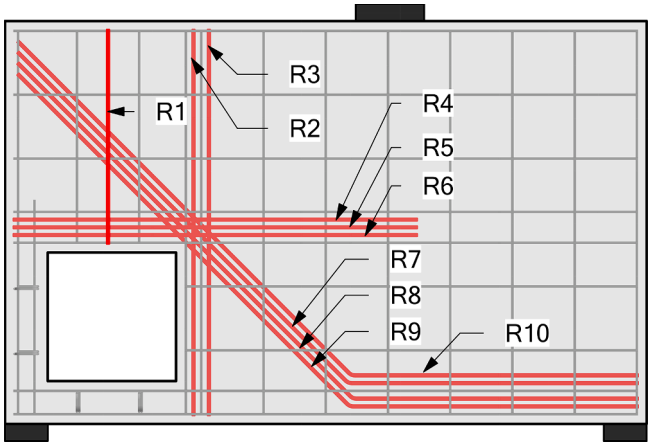

Fig. 8. Optimization domain for the design of SI.c under the STPBO approach.

Table 2
STPBO problem definition for the design of SI.c.

Goal function	Constraints	Rule systems
Maximize $PI = \frac{\sigma_{ij} W_0}{\sigma_{0j} W_i} \beta_i$ **Optimization domain (OD)** R1 to R10	• MDR; • Corner reinf.; • Concrete shape; • Boundary conditions; • Load conditions; • Materials properties (design values); • $\sigma_{ij} \leq \sigma_{adm}$ (constraint coupled to the goal function through β_i).	• Calculations by NL-FEA through EPSF (jconc); • The elimination of rebar occurs • Before eliminating the rebar position completely, the optimization process shall firstly reduce the number of rebar to one on that position.

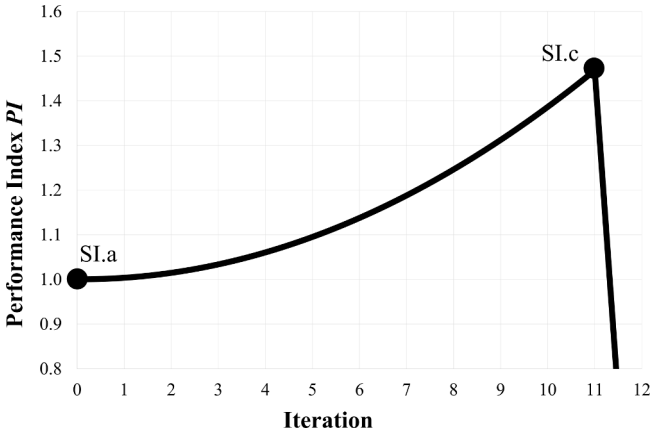

Fig. 9. Performance index history in the design of SI.c.

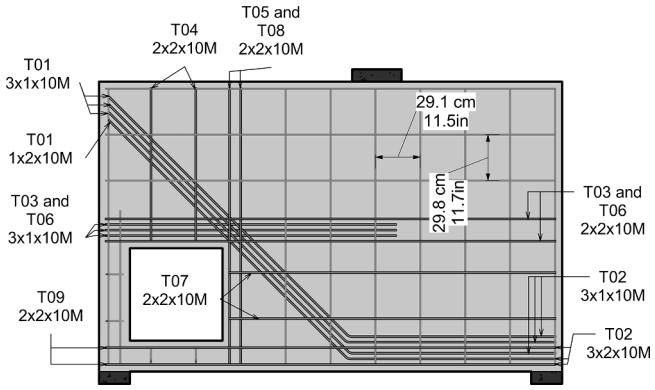

Fig. 10. Reinforcement detailing for SI.c.

3. Experimental program

Specimen SI.a was tested using a large-scale test setup in the structural laboratory of the University of Windsor, Ontario, Canada. All the reinforcement bars used in this experimental program were 10 M of grade 400 W (see Canadian standard [35]). The material tests [51] on the rebar exhibited the yield stress of 495.1 MPa, ultimate stress of 730.5 MPa, and modulus of elasticity of 269.2 GPa. According to the procedures established in reference [42], a concrete compressive strength of 43.2 MPa was obtained through the cylinder test.

3.1. Test setup

As a very high load was needed (close to 2000 kN) and the specimen

dimensions were very large, a brand-new test framework was designed and built for the experimental work. Therefore, a set of two "I" steel beams was designed especially for this test. This new steel set was tied against two strong concrete walls through their holes. The specimen and the bottom instrumentation were placed into the gap formed by the strong floor and the new set of "I" beams. Finally, the loading actuator, the load cell, and the steel plates (see Fig. 11) filled the remaining height gap. Ten 5-mm strain gauges at five different locations of reinforcement bars were placed (see Fig. 11a)). Three linear variable differential transformers (LVDT) were used for measuring the displacements. Two of them (left and right LVDT) were positioned to capture the deflection of the bottom surface of the specimen. The third one was positioned in the z-direction, to monitor a possible out-of-plane displacement (in the width direction).

Fig. 11b) shows that a slotted hollow steel tube was mounted on the left strong wall. The out-of-plane LVDT was placed on this steel tube. The entire set of instrumentations was connected to a computerized data acquisition system (DAQ). In addition to the physical instrumentation, the test setup also used the digital image correlation (DIC) technique as a non-contact measurement of displacements, strains, and cracks. The left and right cameras were positioned overlapping the capture range of each other, as presented in the setup top view (Fig. 11b)). The DIC system was set to take pictures every 4 s during the test. For each photo taken by the DIC system, one row in a sheet was created registering the physical and digital instrumentation together. The photograph presented in Fig. 11c) was taken during the test.

3.2. Specimen preparation

Supplementing the reinforcements presented in Figs. 4 and 5, spacing and lifting hooks were included, as Fig. 12 shows. Plywood was used for the formwork and timber strips were used to stiffen the formwork. The square hole in the specimen was created by inserting Styrofoam sheets, which were removed once concrete hardened. The specimen was cast in the horizontal position for constructability reasons (see Fig. 13). Before the concrete gets hard, the top surface (Fig. 13b) was toweled to facilitate the use of DIC. The specimen was cured at room

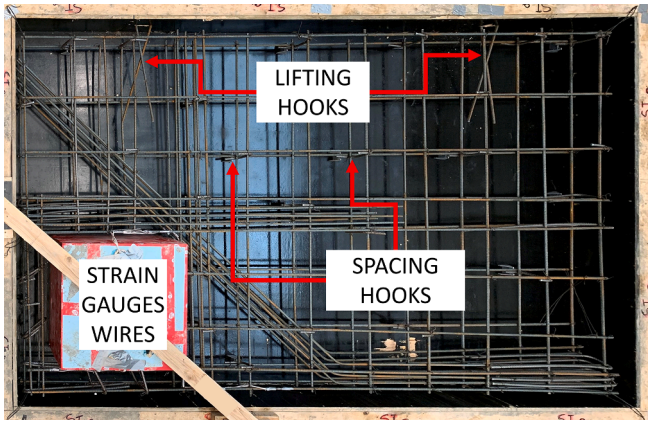

Fig. 12. SI.a formwork before the casting.

temperature in the laboratory environment. During the concrete curing, the specimen was covered by wet burlap sheets. Lastly, a speckle painting (suitable for DIC) was applied to the top surface of the specimen.

3.3. Experimental results

After the characterization of the materials, the STM model used on the design of specimen SI.a (see Fig. 3) was updated with experimental results and without considering partial factors. Thus, the theoretical load capacity according to the STM (P_{STM}) was obtained equal to 1188.2 kN. The limiting factor for the calculation of P_{STM} was the yielding of the tie T09 (see Fig. 3). Fig. 14 presents the relationship between the applied point load and the vertical displacement acquired from the left LVDT (see Fig. 11). For an applied load of 1311.7 kN, the reinforcement reaches the yielding (P_y) in the experimental test. This behavior was measured by one of the strain gauges fixed to the S4 position (see Fig. 11). The ultimate applied load (P_u) of 1831.6 kN was obtained from the laboratory test. However, at the load of 1367.1 kN (P_{cru}), a local

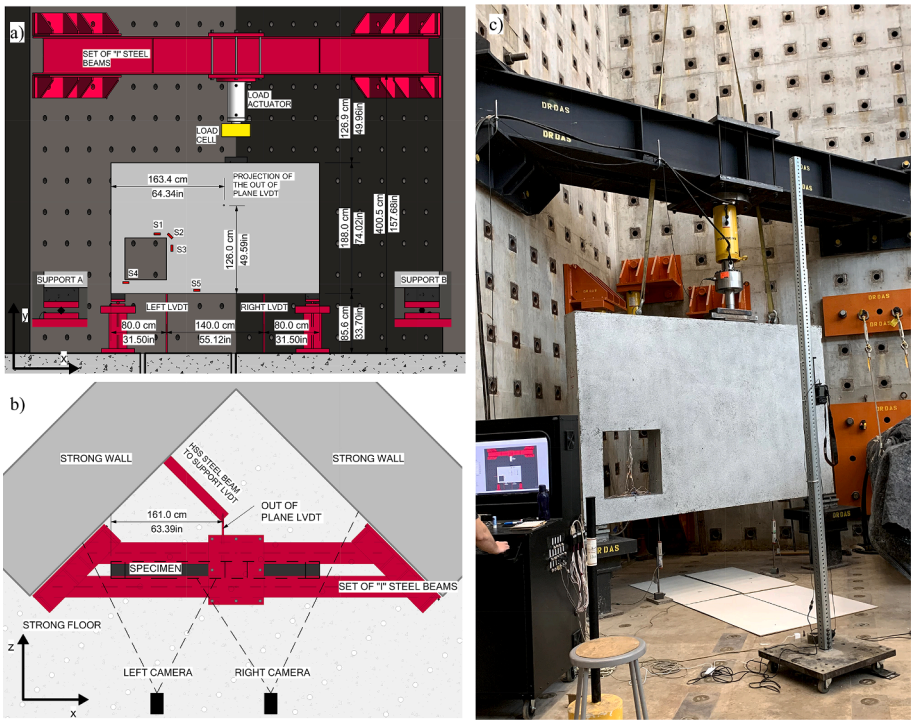

Fig. 11. SI.a Test setup: a) frontal elevation; b) top view; and c) photography.

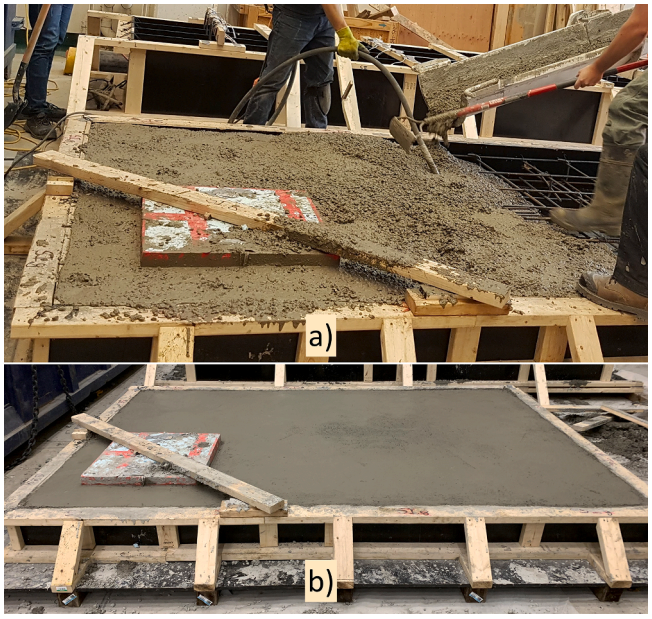

Fig. 13. SI.a concrete casting.

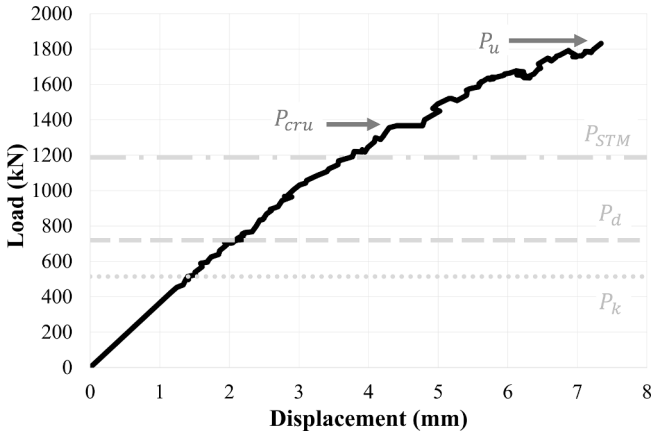

Fig. 14. Experimental deflection of SI.a at the left LVDT point of inspection.

concrete crushing was observed at the right support region (see node N04 in Fig. 3). The detachment of a concrete portion belonging to the cover was notable between P_{cru} and P_u.

Fig. 14 shows that both concrete local crushing load (P_{cru}) and ultimate load (P_u) recorded are much higher than the factored design load (P_d) and the service load (P_k). The absence of yielding plateau until P_{cru} reveals a quasi-brittle behavior. This was also confirmed from the crack pattern obtained using the DIC technique. The software *GOM correlate* [52,53] was used to analyze the data obtained from the DIC system. According to Corr et al. [54], with the development of macrocracks, the DIC minor strain measurement becomes less meaningful. However, the minor strain map can reveal the crack pattern history. Fig. 15 presents the crack pattern obtained from the DIC data at the load of P_{cru}. The lowest strain is presented in green and the highest one is shown in red.

The crack widths were measured where they started to be formed using the procedure presented in references [54,55]. Six major cracks are labeled in Fig. 15. The widths of these cracks at various stages of loading are presented in Table 3.

Cracks 1, 2, 3, and 6 became measurable (about 0.1 mm of width) under the load of 425.7 kN (P_{cra}). The maximum width of crack 6 was found to be 0.4 mm when the specimen was experiencing the local concrete crushing (P_{cru} = 1367.1 kN). The largest crack width was 1.4

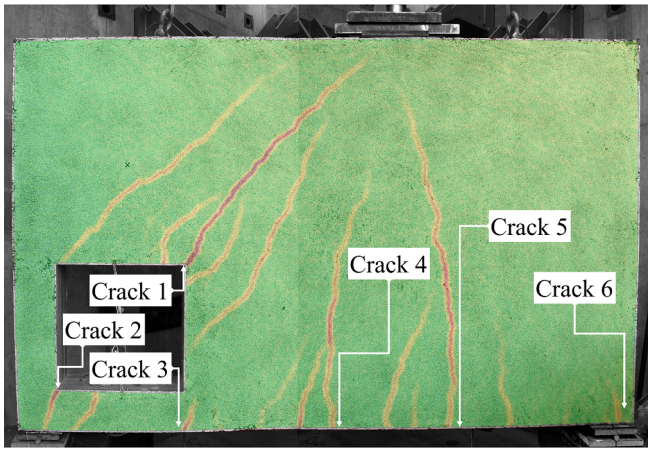

Fig. 15. Crack pattern under the load of 1367.1 kN (P_{cru}).

Table 3
Crack width history.

Load		Crack Width (mm)					
Meaning	**Value (kN)**	**1**	**2**	**3**	**4**	**5**	**6**
P_{cra} (test)	425.7	0.1	0.1	0.1	0.0	0.0	0.1
P_k (design)	514.3	0.2	0.1	0.1	0.0	0.0	0.1
P_d (design)	720.0	0.4	0.2	0.3	0.0	0.0	0.2
P_{STM}(design/test)	1188.2	0.6	0.4	0.6	0.4	0.3	0.3
P_y (test)	1311.7	0.6	0.7	0.6	0.4	0.3	0.4
P_{cru} (test)	1367.1	0.6	0.7	0.6	0.4	0.3	0.4
P_u (test)	1831.6	0.9	1.4	1.0	0.4	0.5	–

mm at the crack 2 position when the ultimate load was applied (P_u = 1831.6 kN). Crack 2 appeared at the location of strain gauge S4 (see Fig. 11). Strain gauges S4 and S1 revealed reinforcement yielding when the load of 1311.7 kN was applied. No other strain gauges showed reinforcement yielding during the test. Fig. 16 shows the local concrete crushing that occurred at the right support region.

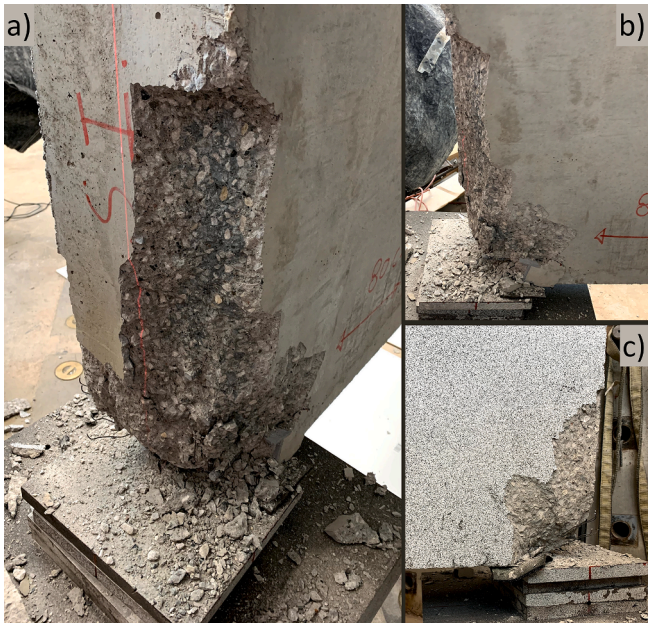

Fig. 16. Right support region after the test.

4. Discussions

The data obtained from the experimental program in specimen SI.a showed a brittle performance. No suitable failure warnings were produced before the failure of the specimen. The difficulty of predicting load capacity by the STM, even in possession of experimental results and without partial factors should also be observed. In that regard, four main points are highlighted: 1) The specimen did not show a yield plateau (remarkable deflections before the failure); 2) The reinforcement reached the yielding (P_y = 1311.7 kN) very close to the concrete crushing (P_{cru} = 1367.1 kN); 3) The prediction of the load capacity according to the STM (P_{STM} = 1188.2 kN) and the value obtained from the experimental test (P_y = 1311.7 kN) differed by 9.4 %. In addition, the yielding position was also not well predicted by the STM; 4) There is no evidence of yielding plateaus on the load–deflection response (see Fig. 14). Previous studies on the same deep beam shape [7,15] exhibited very similar load–deflection responses.

Brena & Morrison [49] presented a list of four reasons explaining the over-designed and brittle performance of deep beams designed by STM: 1) STM is based on the lower-bound solution; 2) The truss analogy does not take into account the contribution of the MDR; 3) The stress redistribution is noticeable on this type of element; 4) The concrete tensile strength is usually neglected in the STM design approach. The same publication [49] received discussions both from Souza and Muttoni et al. These authors highlight the role of the MDR on the over-strength of STM-designed structures. Souza also suggests an interactive approach based on NL-FEA. Note that this approach is similar both to the one proposed by Ruiz & Muttoni [4] and to that proposed by Silveira & Souza [56]. Both Brena & Morrison [49] and the discussions proposed by both Souza and Muttoni et al. [49] corroborate and substantiate the STPBO method proposed in this paper.

4.1. Investigation on the concrete local crushing

Usually, the compressive concrete strength is obtained from cylinder tests, which basically analyze the concrete piece under uniaxial compressive stress. However, after testing 30 RC panels under a variety of biaxial states of stress, Vecchio & Collins [34] found that concrete is softer and weaker under the state of plane stress than under the uniaxial cylinder test. A complete theory named the modified compression-field theory (MCFT) was presented by Vecchio & Collins [34]. The MCFT substantially evolved over the last decades (see references [34,47,48]). As concrete had a local crushing at a CCT nodal region (N04), the concrete loss of strength formulation from MCFT was applied to this investigation similarly to Kuchma et al. [10]. The orange curve presented in Fig. 17 was built from Eq. (1) [34] using the principal tensile strain ($\varepsilon_{1\,exp}$) extracted from the DIC experimental results. Therefore, the actual concrete compressive strength is plotted in the y-axis and the applied load is plotted in the x-axis.

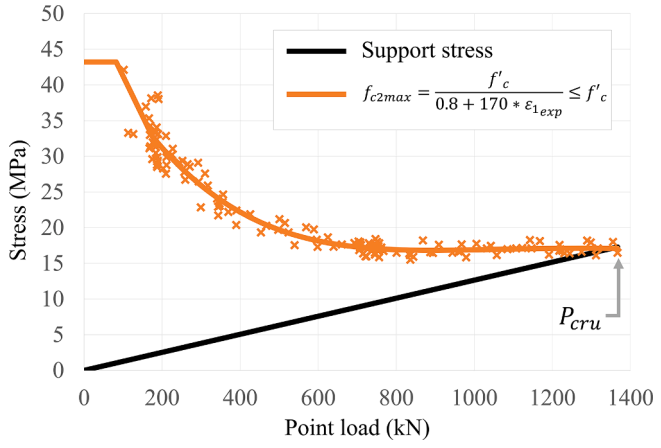

Fig. 17. Concrete loss of compressive strength (MCFT) at the nodal region N04.

Fig. 17 also plots the principal compressive stress on the right support (y-axis) versus the applied load (x-axis). The fact that the orange and the black curves merge right before the load of 1367.1 kN (P_{cru}) should be highlighted. The tensile strain over the surface at this loading stage in the N04 region captured by the DIC was used on the MCFT formulation (Eq. (1)) leading to an actual compressive strength of 0.38 $\times f_c^{'}$ or 16.5 MPa. The compressive stress acting in this region obtained from the test was about 17.3 MPa (4.6% of error). Thus, from the MCFT point of view, it is possible to say that the superficial transversal tensile strain was large enough to decrease the compressive strength and match the acting stress at the N04 region under the load of P_{cru}.

4.2. Numerical investigation

2D numerical analyses of the three structural members were carried out for comparison purposes. The experimental results from specimen SI.a were used to validate the numerical strategy. The reinforcement steel bars were modeled as truss finite elements with an elastic–plastic constitutive model, as shown in Fig. 18b) and Fig. 18d), respectively. A damage constitutive model with two independent scalar damage variables for tension and compression, as proposed by Bitencourt et al. [57] was used to model the concrete behavior (see Fig. 18c). The concrete was discretized using constant strain triangle (CST) elements, as presented in Fig. 18a). Perfect adherence between concrete and reinforcement bars elements was modeled using the coupling finite elements (CFE) technique proposed by Bitencourt et al. [58]. As shown before, the local concrete crushing was well described by the MCFT [34] equation for the loss of concrete compressive strength due to the transversal tensile strain. Therefore, the referred FE technique [57,58] was used in the current study associated with the MCFT equation presented in Fig. 17. The properties of materials used in the numerical simulations were taken from the experimental program (see section 3).

4.2.1. Performance prediction by FEA

The FEA showed the yield load (P_y) of 1373.6 kN and ultimate load (P_u) of 1761.6 kN for specimen SI.a. The differences in these two load values obtained from the test are 4.7% and 3.8%, respectively. Considering the complexity of the specimen and the stress distributions, these differences are small and thus, a good correlation between the FE model and test data was obtained. The load–displacement response for each FE simulation is presented in Fig. 19. Notably, the three specimens showed stiffness responses similar before the design load (720 kN). Beyond the application of the design load, both SI.b and SI.c showed more ductile behavior compared to specimen SI.a. Despite having less reinforcement than specimen SI.b, specimen SI.c showed lower deflection levels. The results of the entire series I are presented in Table 4.

The index proposed by Herranz et al. [59], which is the ratio between the ultimate load (P_u) and the reinforcement weight in kilograms (kg), was used to quantify the reinforcement use efficiency in the current study. Better performance of SI.c was obtained when compared to the other two specimens, SI.a and SI.b. The use of the STPBO process for designing the current deep beam led to an increase in reinforcement use efficiency. When compared to the experimental results of the STM-designed deep beam (SI.a) the increase was 10.5%. However, when compared to the FEA results for the same specimen (SI.a) the increase was even larger (14.9%). The numerical prediction for the crack pattern was done based on the results of the concrete tensile damage. Fig. 20 shows the concrete tensile damage ranged from 0.94 to 1 for each specimen under their yielding load (P_y) as presented in Table 4. Fig. 21 depicts the stress fields under the ultimate load (P_u) predicted for the three specimens. As expected, the tensile stress acting on cracked concrete elements did not play an important role in the specimen equilibrium. Once again a good agreement was noticed between the

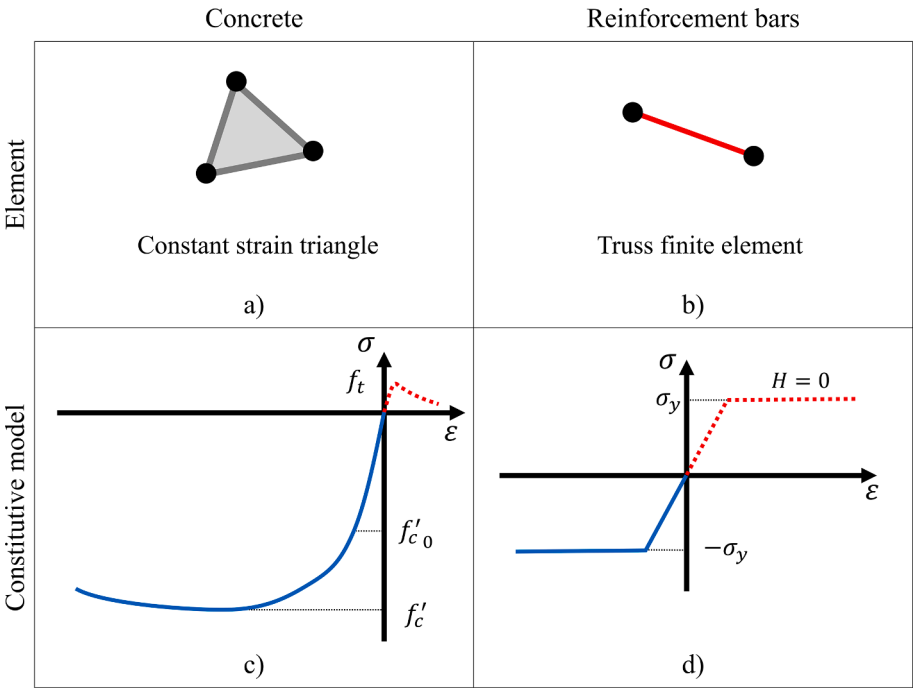

Fig. 18. Numerical strategy a) concrete finite element; b) reinforcement bars finite element; c) concrete constitutive model; d) reinforcement bars constitutive model.

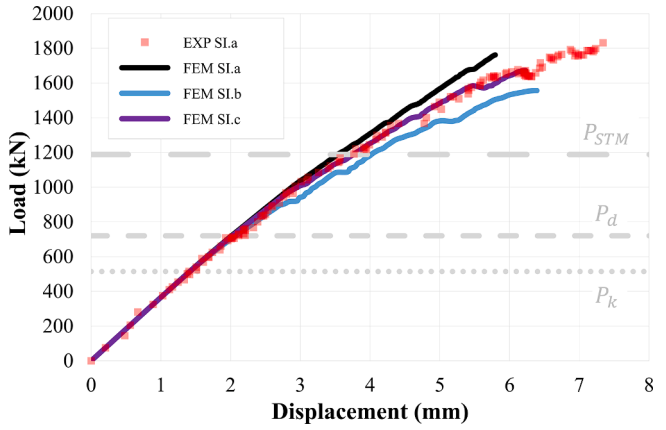

Fig. 19. Load × displacement in the left LVDT position for experimental and numerical results.

Table 4
Comparison of performance of Series I specimens.

Sp.	$W_{reinf.}$ (kg)	P_y (kN)	P_u (kN)	$P_u/W_{reinf.}$ (kN/Kg)	% (SI.a EXP)	% (SI.a FEA)
SI.a (EXP)	134.3	1311.7	1831.6	13.6	0.0	4.0
SI.a (FEA)	134.3	1373.6	1761.7	13.1	−3.8	0.0
SI.b (FEA)	119.0	1213.3	1556.4	13.1	−4.1	−0.3
SI.c (FEA)	111.0	1242.3	1672.2	15.1	10.5	14.9

experimental results (Fig. 15) and the numerical prediction (Figs. 20 and 21).

From Fig. 20, it can be observed that SI.b has the most intensive cracking level under the P_y on the upper right corner of the hole. In turn, SI.a and SI.c have rebar perpendicularly oriented with the main crack direction (T01), and SI.b has just x- and y-oriented rebar to restrain this crack formation. A high level of stress concentration on the rebar of this region can be observed in the stress fields performed by specimen SI.b (see Fig. 21). Another remarkable difference from the stress fields performed by SI.b to the one performed by SI.a and SI.c is the compressive stress concentration that occurred near the left support. Fig. 21 reveals an inclined strut in SI.b, carrying a relevant level of compressive stress from the bottom of the hole to the left support. These stress concentrations could not be found in the stress fields of SI.a and SI.c. Given that SI.a and SI.c have similar reinforcement layouts, differing just by the amount of each rebar position, the stress fields formed at SI.a and SI.c were also similar. The main difference, however, can be found in the tensile distribution among the reinforcement bars. The stress fields exhibited by SI.a under P_u (Fig. 21) showed stress concentrations in some rebar spots. Hence, the vast majority of the MDR in SI.a shared no relevant tensile stress according to the numerical predictions. Conversely, the STPBO-designed specimen (SI.c), when compared to SI.a, presented better distribution in the tensile stress among the reinforcement bars as shown in Fig. 21.

The failure modes for SI.a and SI.c predicted by the numerical simulations showed good agreements with the test data of specimen SI.a. The incorporation of the MCFT (Eq. (1)) into the FEA strategy was found to be crucial to describe the compressive local failure as shown in Figs. 16 and 17. The SI.b failure mode predicted by FEA was, however, fairly different from the other two specimens. A shear failure for specimen SI.b was experienced by the left support region. The combination of the high level of compressive stress acting on the inclined concrete strut mentioned before, with the tensile stress acting at the yielding level on nearby rebar was crucial to the shear failure.

5. Conclusions

The main goal of this paper is the proposal of a novel design approach called the strut-and-tie performance-based optimization (STPBO) method which uses STM and PBO methods. The results of material consumption and structural performance were compared within specimens designed by very well-known methods. A large-scale specimen was designed and built using the STM. The specimen was

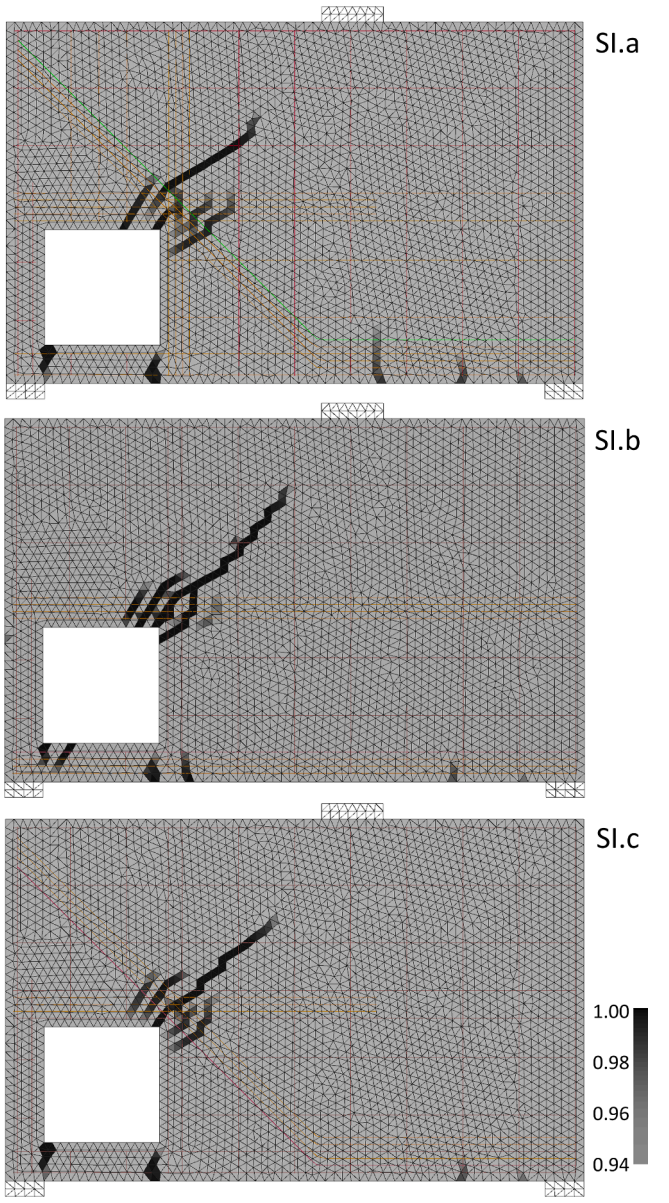

Fig. 20. Numerical prediction of the crack pattern under the yielding load (P_y).

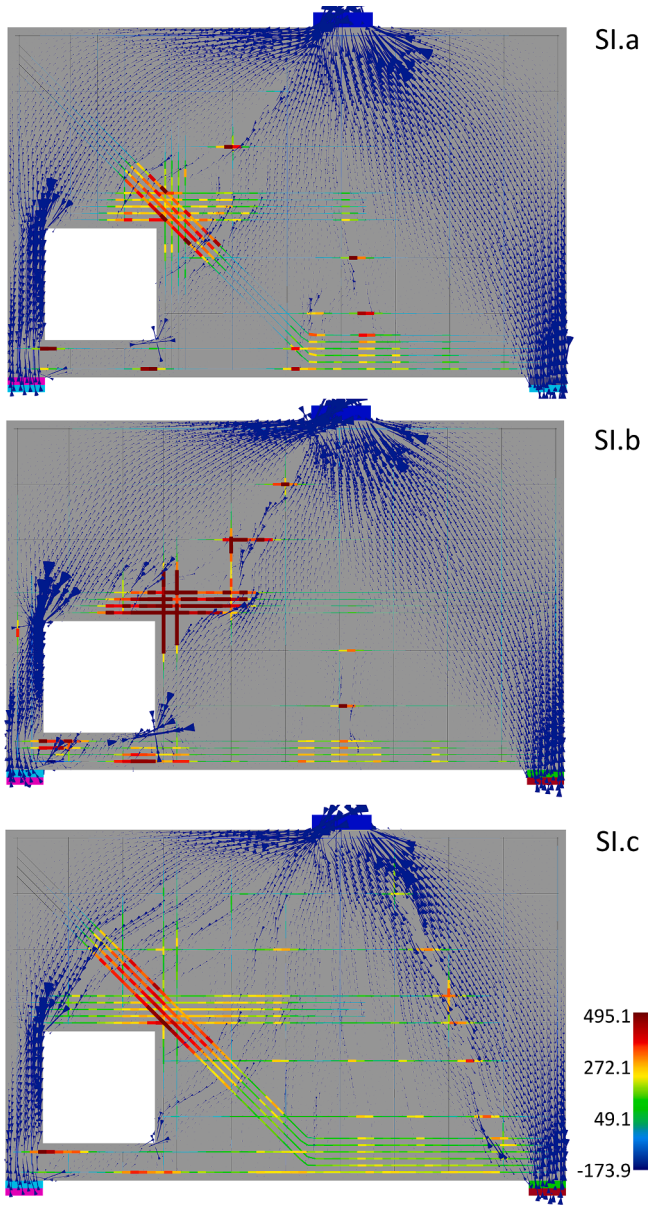

Fig. 21. Numerical prediction of the stress fields under the ultimate load (P_u).

tested and the results were used as reference values. The main conclusions of this investigation can be summarized as follows:

1. The use of STM complying with the ACI-318 [1] requirements for the design of the deep beam with a large hole [6] led to an over-reinforced solution. The neglect of the structural contribution of the MDR in the STM was considered the main cause of the use of more reinforcement than necessary.
2. The experimental compressive concrete failure in a CCT node (right support region) occurred much earlier than predicted by the STM complying with ACI-318 [1]. The referred failure happens in the test when node N04 is experiencing a stress level of 38% of the $f_c^{'}$ (standard cylinder test). Whereas the ACI-318 [1] establishes the use of the factor of 0.8 for this type of node.
3. The brittle behavior experimentally performed by the specimen designed using the STM guidelines from ACI-318 [1] was caused by the use of more reinforcement than necessary and the difficulty in predicting the behavior of critical nodes by the STM (e.g. N04).
4. The loss of compressive strength witnessed in cracked concrete subjected to high tensile strains normal to the compressive direction was well represented by the modified compression-field theory (MCFT). The strain obtained experimentally from the digital image correlation (DIC) technique was used in the equation proposed by Vecchio & Collins [34]. This application has shown good agreement between the strength prediction and the actual local concrete failure. The difference was only 4.6%.
5. The reinforcement layout highly influences the stress distribution and hence, the failure mode on this type of deep beam. The absence of the inclined reinforcement at the upper right corner of the hole led specimen SI.b (EPSF-designed) to experience a different failure location and mode. The numerical predictions showed higher crack widths in SI.b than SI.a and SI.c at the referred position under the failure load (P_u). The framework proposed by Ruiz & Muttoni [4] showed to be a good solution in terms of design automation of D-regions. However, design rules capable of creating new rebar should be incorporated into the EPSF approach, enabling the control of cracking levels in strategic positions, as proposed by Silveira et al [60].
6. The proposed method named strut-and-tie performance-based optimization, applied to the design of specimen SI.c, resulted in less

employment of material and significant improvements in the structural performance. The relationship between the ultimate load (P_u) and the amount of reinforcement ($W_{reinf.}$) increased by 14.9% when compared to the experimental results of the STM-designed specimen (SI.a).

7. An investigation based on NL-FEA that combines damage theory with MCFT was performed in this research. This approach showed consistent agreements with the experimental large-scale test results.

Furthermore, other strut-and-tie truss models for the deep beam studied should be explored under the STPBO approach. More experimental large-scale investigations are required, especially in SI.b and SI.c (see reinforcement detail in Supplementary material). Also recommendable is the application of the STPBO method to different types of SC members. Automations in the process are advisable once the proposed approach is further explored.

Declaration of Competing Interest

The authors declare that they have no known competing financial interests or personal relationships that could have appeared to influence the work reported in this paper.

Acknowledgments

The authors wish to acknowledge the Emerging Leaders in the Americas Program (ELAP) for the scholarship provided to Mr. Marcos V. G. Silveira. This study was financed in part by the Coordenação de Aperfeiçoamento de Pessoal de Nível Superior – Brasil (CAPES) – Finance Code 001. As well, the cost of all the experimental work was supported by NSERC through Dr. Sreekanta Das. Dr. Luís A.G. Bitencourt Jr. would also like to extend his acknowledgments to the financial support of the National Council for Scientific and Technological Development. CNPq (Proc. N°: 310401/2019-4). The authors further recognize the help of structural laboratory technical staff members Mr. Matthew St. Louis and Mr. Jerome Finnerty. Moreover, the help from Mr. Bruno Paini, a Ph.D. student at the University of Windsor, was crucial to the experimental program of this research. The authors would also like to express their gratitude to Dr. Rafael Alves de Souza who provided relevant insights for this research. Lastly, the authors would like to thank Autodesk, Inc. for the support on the license courtesy of Revit® software.

Appendix A. Supplementary data

Supplementary data to this article can be found online at https://doi.org/10.1016/j.istruc.2022.05.035.

References

[1] American Concrete Institute 2019;10(14359/51716937).
[2] Hsu TTC. Unified Theory of Reinforced Concrete. Taylor & Francis; 1993. https://books.google.com.br/books?id=eZtzfC7TZTQC.
[3] Reineck K-H, Ed. Examples for the Design of Structural Concrete with Strut-and-tie Models. American Concrete Institute; 2002.
[4] Ruiz MF, Muttoni A. On development of suitable stress fields for structural concrete. ACI Struct J 2007;104:495–502. https://doi.org/10.14359/18780.
[5] Nielsen MP, Hoang LC. Limit analysis and concrete plasticity. 3rd ed. CRC Press; 2010.
[6] Schlaich J, Schaefer K, Jennewein M. Toward a Consistent Design of Structural Concrete. PCI J 1987. https://doi.org/10.15554/pcij.05011987.74.150.
[7] Maxwell BS, Breen JE. Experimental Evaluation of Strut-and-Tie Model Applied to Deep Beam with Opening. ACI Struct J 2000;97. https://doi.org/10.14359/843.
[8] Chen BS, Hagenberger MJ, Breen JE. Evaluation of Strut-and-Tie Modeling Applied to Dapped Beam with Opening. ACI Struct J 2002;99. https://doi.org/10.14359/12113.
[9] Ley MT, Riding KA, Widianto S, Bae JE Breen. Experimental Verification of Strut and Tie Model Design Method. ACI Struct J 2007;104. https://doi.org/10.14359/18957.
[10] Kuchma D, Sukit Y, Nagle T, Hart J, Lee HH. Experimental Validation of Strut-and-Tie Method for Complex Regions. ACI Struct. J. 2008;105. https://doi.org/10.14359/19941.
[11] Ismail KS, Guadagnini M, Pilakoutas K. Shear behavior of reinforced concrete deep beams. ACI Struct J 2017;114(87–99). https://doi.org/10.14359/51689151.
[12] Zhou L, Liu Z, He Z. Elastic-to-Plastic Strut-and-Tie Model for Deep Beams. J Bridg Eng 2018. https://doi.org/10.1061/(ASCE)BE.1943-5592.0001206.
[13] Jewett JL, Carstensen JV. Experimental investigation of strut-and-tie layouts in deep RC beams designed with hybrid bi-linear topology optimization. Eng Struct 2019. https://doi.org/10.1016/j.engstruct.2019.109322.
[14] Mohammedali TK, Jalil AM, Abdul-Razzaq KS, Mohammed AH. STM experimental verification for reinforced concrete continuous deep beams. Int J Civ Eng Technol 2019;10:2227–39.
[15] Chen H, Wang L, Zhong J. Study on an optimal strut-and-tie model for concrete deep beams. Appl Sci 2019;9. https://doi.org/10.3390/app9173637.
[16] Marti P. Basic Tools of Reinforced Concrete Beam Design. J Am Concr Inst 1985;82:46–56. https://doi.org/10.14359/10314.
[17] Schlaich J, Schaefer K. Design and detailing of structural concrete using strut-and-tie models. Struct Eng London 1991.
[18] K.-H. Reineck, A.C.I. Convention, A.C.I.F. Convention, S. and T.M. American Concrete Institute. Subcommittee 445-1, Examples for the Design of Structural Concrete with Strut-and-tie Models, American Concrete Institute, 2002. https://books.google.com.br/books?id=795RAAAAMAAJ.
[19] Tjhin TN, Kuchma DA. Computer-Based Tools for Design by Strut-and-Tie Method: Advances and Challenges. ACI Struct J 2002;99. https://doi.org/10.14359/12298.
[20] Souza R, Kuchma D, Park J, Bittencourt T. Adaptable Strut-and-Tie Model for Design and Verification of Four-Pile Caps. ACI Struct J 2009;106. https://doi.org/10.14359/56352.
[21] Mezzina M, Palmisano F, Raffaele D. Designing Simply Supported R.C. Bridge Decks Subjected to In-Plane Actions: Strut-and-Tie Model Approach. J Earthq Eng 2012;16:496–514. https://doi.org/10.1080/13632469.2011.653866.
[22] Liang QQ, Xie YM, Steven GP. Topology Optimization of Strut-and-Tie Models in Reinforced Concrete Structures Using an Evolutionary Procedure. ACI Struct J 2000;97.
[23] Xie YM, Steven GP. Technical note a simple approach to Structural Optimization. Comput Struct 1993;49:885–96.
[24] Huang X, Xie YM. Convergent and mesh-independent solutions for the bi-directional evolutionary structural optimization method. Finite Elem Anal Des 2007;43:1039–49. https://doi.org/10.1016/j.finel.2007.06.006.
[25] Huang X, Xie YM. A new look at ESO and BESO optimization methods. Struct Multidiscip Optim 2008;35:89–92. https://doi.org/10.1007/s00158-007-0140-4.
[26] Liang QQ, Uy B, Steven GP. Performance-based optimization for strut-tie modeling of structural concrete. J Struct Eng 2002. https://doi.org/10.1061/(ASCE)0733-9445(2002)128:6(815).
[27] Q.Q. Liang, Performance-Based Optimization of Structures: Theory and Applications, 1st ed., CRC Press, London, 2005. 10.1002/0470867353.
[28] Liang QQ. Performance-Based Optimization: A Review. Adv Struct Eng 2007;10:739–53. https://doi.org/10.1260/136943307783571418.
[29] Jewett JL, Carstensen JV. Topology-optimized design, construction and experimental evaluation of concrete beams. Autom Constr 2019;102:59–67. https://doi.org/10.1016/j.autcon.2019.02.001.
[30] Liu J, Gaynor A, Chen S, Kang Z, Suresh K, Takezawa A, et al. Current and future trends in topology optimization for additive manufacturing. Struct Multidiscip Optim 2018. https://doi.org/10.1007/s00158-018-1994-3.
[31] Carstensen JV. Topology optimization with nozzle size restrictions for material extrusion-type additive manufacturing. Struct Multidiscip Optim 2020. https://doi.org/10.1007/s00158-020-02620-5.
[32] Vantyghem G, De Corte W, Shakour E, Amir O. 3D printing of a post-tensioned concrete girder designed by topology optimization. Autom Constr 2020;112:103084. https://doi.org/10.1016/j.autcon.2020.103084.
[33] Muttoni A, Ruiz MF, Niketic F. Design versus assessment of concrete structures using stress fields and strut-and-tie models. ACI Struct J 2015;112:605–15. https://doi.org/10.14359/51687710.
[34] Vecchio FJ, Collins MP. The Modified Compression-Field Theory for Reinforced Concrete Elements Subjected to Shear. ACI J 1986;83. https://doi.org/10.14359/10416.
[35] Canadian Standards Association, Carbon steel bars for concrete reinforcement CSA G30.18-09, 2019.
[36] Canadian Standards Association, Design of Concrete Structures CSA A23.3-14, 2014.
[37] H.E. Fairclough, T.J. Pritchard, L. He, M. Gilbert, LayOpt: A truss layout optimization web application, (2020). https://www.layopt.com (accessed July 24, 2020).
[38] A. Muttoni, O. Burdet, N. Kostic, M.F. Ruiz, i-concrete project, Syst. Stress Fields Dev. Concr. Struct. (n.d.). https://i-concrete.epfl.ch/ (accessed July 28, 2020).
[39] Tjhin TN, Kuchma DA. Integrated analysis and design tool for the strut-and-tie method. Eng Struct 2007;29:3042–52. https://doi.org/10.1016/j.engstruct.2007.01.032.
[40] Jung-Woong P, Sukit Y, Tjen T, Daniel K. Automated Finite-Element-Based Validation of Structures Designed by the Strut-and-Tie Method. J Struct Eng 2010;136:203–10. https://doi.org/10.1061/(ASCE)0733-9445(2010)136:2(203).
[41] Klein GJ. Curved-Bar Nodes: a detailing tool for strut-and-tie models. Concr Int 2008;30:42–7. https://doi.org/10.14359/19949.
[42] ASTM International. C39/C39M-18: Standard Test Method for Compressive Strength of Cylindrical Concrete Specimens. Am Soc Test Mater 2018. https://doi.org/10.1520/C0039_C0039M-18.

[43] Liang QQ, Xie YM, Steven GP. Generating Optimal Strut-and-Tie Models in Prestressed Concrete Beams by Performance-Based Optimization. ACI Struct J 2001;98. https://doi.org/10.14359/10191.
[44] Ali MA, White RN. Automatic generation of truss model for optimal design of reinforced concrete structures. ACI Struct J 2001. https://doi.org/10.14359/10286.
[45] Picelli R, Townsend S, Brampton C, Norato J, Kim HA. Stress-based shape and topology optimization with the level set method. Comput Methods Appl Mech Eng 2018;329:1–23. https://doi.org/10.1016/j.cma.2017.09.001.
[46] Smarslik M, Ahrens MA, Mark P. Toward holistic tension- or compression-biased structural designs using topology optimization. Eng Struct 2019;199:109632. https://doi.org/10.1016/j.engstruct.2019.109632.
[47] Vecchio FJ, Collins MP. Compression response of cracked reinforced concrete. J Struct Eng (United States) 1993. https://doi.org/10.1061/(ASCE)0733-9445(1993)119:12(3590).
[48] Bentz EC, Vecchio FJ, Collins MP. Simplified modified compression field theory for calculating shear strength of reinforced concrete elements. ACI Struct J 2006;10(14359/16438).
[49] Brena SF, Morrison MC. Factors Affecting Strength of Elements Designed Using Strut-and-Tie Models. ACI Struct J 2007;104. https://doi.org/10.14359/18616.
[50] Autodesk, Revit | BIM Software | Autodesk Official Store, (2020). https://www.autodesk.com/products/revit/overview (accessed August 6, 2020).
[51] ASTM International. A370–19e1: Standard Test Methods and Definitions for Mechanical Testing of Steel Products. Am Soc Test Mater 2019. https://doi.org/10.1520/A0370-19E01.
[52] GOM, GOM Correlate | GOM, (n.d.). https://www.gom.com/3d-software/gom-correlate.html (accessed June 30, 2020).
[53] M.F. Smrkić, J. Košćak, D. Damjanović, Application of 2D digital image correlation for displacement and crack width measurement on RC elements, Gradjevinar. (2018). 10.14256/JCE.2407.2018.
[54] Corr D, Accardi M, Graham-Brady L, Shah S. Digital image correlation analysis of interfacial debonding properties and fracture behavior in concrete. Eng Fract Mech 2007;74:109–21. https://doi.org/10.1016/j.engfracmech.2006.01.035.
[55] Zohreh Heydariha J, Das S, Banting B. Effect of grout strength and block size on the performance of masonry beam. Constr Build Mater 2017;157:685–93. https://doi.org/10.1016/j.conbuildmat.2017.09.130.
[56] Silveira MVG, de Souza RA. Analysis and design of reinforced concrete deep beams using the stress fields method. Acta Sci Technol 2017;39:587. https://doi.org/10.4025/actascitechnol.v39i5.28409.
[57] Bitencourt LAG, Manzoli OL, Trindade YT, Rodrigues EA, Dias-da-Costa D. Modeling reinforced concrete structures using coupling finite elements for discrete representation of reinforcements. Finite Elem Anal Des 2018;149:32–44. https://doi.org/10.1016/j.finel.2018.06.004.
[58] Bitencourt LAG, Manzoli OL, Prazeres PGC, Rodrigues EA, Bittencourt TN. A coupling technique for non-matching finite element meshes. Comput Methods Appl Mech Eng 2015;290:19–44. https://doi.org/10.1016/j.cma.2015.02.025.
[59] Herranz JP, Santa Maria H, Gutierrez S, Riddell R. Optimal Strut-and-Tie Models Using Full Homogenization Optimization Method. ACI Struct J 2012;109. https://doi.org/10.14359/51684038.
[60] Silveira MVG, Paini B, Bitencourt Jr LAG, Das S. Design and experimental investigation of deep beams based on the Generative Tie Method. Eng Struct 2022;255:113913. https://doi.org/10.1016/j.engstruct.2022.113913.

3. Research Paper II

This chapter is presented in the format of a journal paper. The following paper entitled "*Design and experimental investigation of deep beams based on the Generative Tie Method* " [53] was published in the Elsevier Engineering Structures Journal. Research Paper II can be accessed via the following link https://doi.org/10.1016/j.engstruct.2022.113913.

Engineering Structures 255 (2022) 113913

Contents lists available at ScienceDirect

Engineering Structures

journal homepage: www.elsevier.com/locate/engstruct

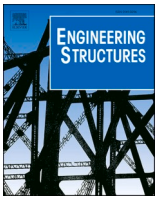

Design and experimental investigation of deep beams based on the Generative Tie Method

Marcos V.G. Silveira [a], Bruno Paini [b], Luís A.G. Bitencourt Jr [a,*], Sreekanta Das [b]

[a] Dept. of Structural and Geotechnical Engineering, University of São Paulo, São Paulo, SP 05508-010, Brazil
[b] Dept. of Civil and Environmental Engineering, University of Windsor, Windsor, ON N9B 3P4, Canada

ARTICLE INFO

Keywords:
Generative tie method (GTM)
Deep beams
Shear strength
Elastic–plastic stress fields (EPSF)
Modified compression-field theory (MCFT)

ABSTRACT

The high level of shear stress present in reinforced concrete deep beams has been the subject of interest for a considerable number of studies due to the uncertainties involved. Several structural codes and standards around the world have recommended using the strut-and-tie method (STM) to design such elements. The STM is proven efficient and accurate, however, the successful application of the method relies decisively on the skills of the designer to conceive truss-like models. In this paper, a framework named Generative Tie Method (GTM) is proposed as an alternative approach to overcome some limitations of the available methods for the design of deep beams. The GTM uses performance ratios obtained from finite element analysis (FEA) as decision-making criteria on the reinforcement layout design of structural concrete members. The FEA strategy used in this approach is based on the elastic–plastic stress fields. The concrete compressive strength loss ratio is obtained using the modified compression-field theory. A large-scale experimental investigation using the digital image correlation technique was carried out on four deep beams designed by the proposed method. The suitable structural performance presented by the specimens demonstrated that the application of the GTM is promising even under unusual design requirements.

1. Introduction

The high compressive strength and the low tensile capacity of concrete are material characteristics that become the design of structural concrete (SC) members a challenging task. Over the past decades, researchers and engineers have been looking for a comprehensive way to understand the structural behavior of SC members. The Euler-Bernoulli beam model has been widely applied to some SC members, such as slender beams, columns, and slabs. However, some special elements cannot be designed by this simplified model. According to the American Concrete Institute (ACI) structural code [1], any SC member which has any load and/or geometric discontinuities must be treated as a discontinuous region (D-region). Typical examples of D-regions are pile caps, beam-column joints, frame corners, corbels, deep beams, holes, and support regions.

Beams with the shear span (a) divided by the effective depth (d) less than 2.5 - shear span-depth ratio (a/d) less than 2.5 - are part of the D-regions group. The ACI structural code [1] recommends the application of the Strut-and-Tie Method (STM) to design this type of beam, also called a deep beam. However, this recommendation is not found exclusively in the ACI structural code [1]. Standards such as the Canadian structural standard [2], the Brazilian structural code [3], the European structural code [4], among other structural standards and codes around the world have been included guidelines based on the STM for deep beams, especially after the study conducted by Schlaich et al. [5].

The combination of Topology Optimization (TO) and STM to aid structural designers in the development of truss-like models has been extensively explored by many researchers over the last two decades [6–13]. In addition, researches using optimization techniques to optimize the reinforcement layout of D-regions have been also gained attention lately [14–17]. The framework proposed by Amir & Sigmund [14] is able to optimize the reinforcement layout of a given SC member from a ground reinforcement layout. The approach is damage-based and uses an embedded reinforcement approach to represent the reinforcement bars. Another outstanding publication is the *Fédération internationale du béton* (*fib*) bulletin number 100 [17]. The *fib* bulletin presents the current state-of-the-art of the STM and the SFM to design and assess structural concrete members. An extensive number of design and assessment examples are also conducted exploring several methods and levels of approximation.

Even though there are several recommendations for the design of

* Corresponding author.
E-mail address: luis.bitencourt@usp.br (L.A.G. Bitencourt Jr).

https://doi.org/10.1016/j.engstruct.2022.113913
Received 4 November 2021; Received in revised form 8 January 2022; Accepted 15 January 2022
Available online 1 February 2022

Nomenclature

List of abbreviations and symbols

Abbreviations and Symbols	Description
DIC	Digital image correlation
D-regions	Discontinuous regions
EPSF	Elastic-plastic stress fields
FEA	Finite element analysis
GTM	Generative tie method
MCFT	Modified compression-field theory
MDR	Minimum distributed reinforcement
NL-FEA	Nonlinear finite element analysis
SC	Structural concrete
SFM	Stress fields method
STM	Strut-and-tie method
TO	Topology optimization
ULS	Ultimate limit state
a	Shear span
a/d	Shear span-depth ratio
b_w	Width of a beam
C_{LS}	Current load step in the GTM
CW_i	Maximum crack width at P_i
CW_s	Maximum crack width at P_s
CW_{test}	Maximum crack width at P_{test}
d	Effective depth of a beam
f'_c	Specified concrete compressive strength
f_{c2max}	Actual compressive strength according to the MCFT
f_{cd}	Design value of concrete compressive strength
$f_c^{'}exp$	Experimental concrete compressive strength
I_c	Cracking index
I_h	Hardening index
I_s	Shear index
I_u	Ultimate index
n_a	Available number of rebar in the GTM
N_{LS}°	Number of load steps in the GTM
n_r	Required number of rebar in the GTM
P_c	Current/analyzed load according to the GTM
P_{crack}	Applied load while the first measurable crack (0.1 mm of width) appears
P_d	Design load or factored load
P_{EPSF}	Ultimate or failure applied load predicted through EPSF
P_i	Applied load
P_s	Service load
P_{test}	Experimental ultimate or failure applied load
P_y	Yielding load or applied load while reinforcement reaches the yielding
V_{crack}	Critical shear force at P_{crack}
V_{EPSF}	Critical shear force predicted through EPSF
V_i	Critical shear force at P_i
V_{test}	Critical shear force at P_{test}
$W_{reinf.}$	Weight of steel reinforcement used in each specimen
ε_1	Principal tensile strain in concrete
η	Minimum value of the adimensional factor which decreases the concrete compressive capacity according to the MCFT
η_{adm}	Admissible value of the loss of compressive strength in the concrete according to the GTM
σ_{adm}	Admissible reinforcement stress according to the GTM
σ_s	Maximum stress acting at the rebar in the analyzed model according to the GTM
φ_a	Available rebar diameter in the GTM
φ_r	Required rebar diameter in the GTM
$\varnothing_{strut}$	Strut angle at P_{test}

deep beams, there are also many uncertainties involved. According to Barros et al. [18], the shear prediction based on the Brazilian structural code [3] may generate unsafe design results. After experiencing frequent diagonal cracking problems in deep beams of several bridges, the Texas Department of Transportation (TxDOT), conducted an extensive experimental program on the structural performance of deep beams [19–21]. One of the main findings of this study [19–21] concerns the serviceability of deep beams. According to Birrcher et al. [19,21], an increase in the minimum web reinforcement (also known as minimum distributed reinforcement) ratio in the ACI structural concrete code [1] is recommended to mitigate the opening of wide cracks due to the high level of shear stress at service load.

The presence of high levels of tensile strain in shear critical elements decreases the concrete compressive strength [22], leading to brittle and premature failures. The STM guidelines of structural codes [1–4] recommend using factors that reduce the compressive strength of concrete (f_{cd}) based on the STM element type. A thorough investigation on the shear strength prediction of SC members named Modified Compression-Field Theory (MCFT) is proposed by Vecchio & Collins [22]. Rather than an indirect prediction (based on the STM element type), the MCFT proposes a directly tensile-dependent prediction of the concrete compressive strength loss due to the high level of tensile strain.

This paper presents a new method for designing SC members under particular conditions named the Generative Tie Method (GTM). The method is a nonlinear process, which uses Finite Element Analysis (FEA) results to make decisions throughout the design process. The FEA strategy used in the GTM is based on the Elastic-Plastic Stress Fields (EPSF) approach proposed by [23,24]. The FEA solver, *jconc* (available in [25]), was used in this study. This FEA solver uses the main premises of the Stress Fields Method (SFM) [26] and also the loss of compressive strength proposed by Vecchio & Collins [22] (MCFT). Four concrete deep beams with the main geometrical characteristics from the specimens studied by Birrcher et al. [19,21] were designed with the help of the GTM. A large-scale experimental investigation on the performance of these four specimens was carried out to explore the features of GTM.

2. The proposal of the Generative Tie Method (GTM)

The Generative Tie Method (GTM) aims to simplify and automate the design process of SC members. The method is a nonlinear process that uses results from finite element analysis (FEA) iteratively to decide the reinforcement layout of a given SC member. The Generative Tie Method can be simplified in a five-step procedure, as shown in Fig. 1.

2.1. Step 1: Input

The goal of the input step is to build the first trial numerical model (Trial 1), which is then analyzed using the Finite Element Method (FEM) in Step 2. Various structural codes and standards recommend minimum distributed reinforcement (MDR) to prevent brittle behavior and to avoid shrinkage and temperature cracks. Hence, the first trial model used in Step 1 must include such minimum reinforcement (MDR). At this stage, the structural designer can influence the final reinforcement layout. However, models developed or generated in subsequent trials may generate very different results when compared to the first trial in Step 1. Besides the geometrical modeling, the designer also defines the load and boundaries conditions in Step 1 for the Trial 1 model. As usual, nonlinear processes divide the loading into many increments. Hence, in addition to the design load (P_d), the designer must inform the number of load steps in the nonlinear process (N_{LS}°). In such a way that the current

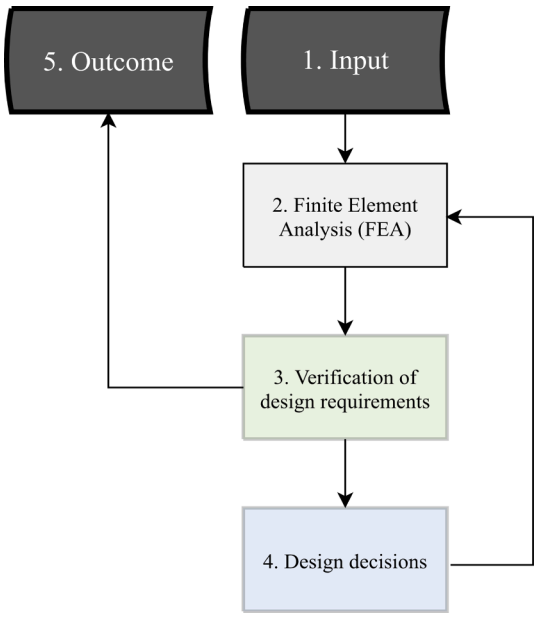

Fig. 1. A simplified flowchart for the Generative Tie Method (GTM).

load or analyzed load (P_c) on the GTM can be expressed in function of P_d, N°_{LS} and the current load step, C_{LS} (see Equation (1)).

$$P_c = \frac{P_d}{N^{\circ}_{LS}} \times C_{LS} \tag{1}$$

2.2. Step 2: Finite element analysis (FEA)

Step 2 undertakes a nonlinear numerical analysis of the current model using FEM. The numerical formulation proposed by Ruiz & Muttoni [23], called the Elastic-plastic Stress Fields (EPSF), and the FEA solver developed by Muttoni et al. [25], named *jconc* are used in this step. In *jconc,* the main Stress Field Method (SFM) hypotheses are combined with elastic–plastic constitutive models and applied to both concrete and steel reinforcement bars. The reinforcement bars are represented by truss finite elements, which means that only axial deformations are allowed in these elements. Elastic-plastic constitutive laws can be used for the reinforcement bars, with or without strain hardening. In this study, strain hardening was not considered to represent the reinforcement bars. The concrete tensile strength was neglected, assuming that concrete after cracking does not share any tensile load or stress. The formulation from the Modified Compression-Field Theory (MCFT) proposed by Vecchio & Collins [22] to represent the compressive strength loss due to the tensile transversal strain is used associated with an elastic–plastic constitutive model to represent the behavior of concrete. A perfect bond between the reinforcements and concrete elements was considered. Further details on the FEA approach used in this study can be found in literature [22–25].

2.3. Step 3: Verification of the design requirements

The design requirements recommended by structural codes and standards are verified in this step. These checks are performed by controlling three variables: the analyzed or current load (P_c), the stress levels acting in concrete, and reinforcement elements. The necessity of a load increasing in the following step (Step 4) is checked by the first logical test (Is $P_c = P_d$?). Two verifications are needed to check the level of stress in concrete. The first one is based on the numerical strategy adopted and explained in the previous step (Step 2). One of the main EPSF hypotheses (which the software is based on) is that concrete is working after cracking in the ultimate limit state (ULS), and thus, no tensile stress is developed in concrete elements. Hence, no solution (in terms of numerical convergence) can be found if there is no reinforcement positioned in the tensile stress regions. On the other hand, the concrete compressive stress level check is performed by one of the MCFT equations [22]. The MCFT prediction of the compressive strength loss of concrete under a high level of transversal tensile strain is adapted from [22] and presented in Equation (2).

$$f_{c2max} = 3.1(f'^{\,2/3}_{c}) \times \eta \leq f'_c$$

$$\eta = \frac{1}{0.8 + 170 \times \varepsilon_1} \tag{2}$$

In this equation, f'_c is the specified concrete compressive strength, usually verified from the standard cylinder test, and f_{c2max} is the actual compressive strength after concrete becomes weaker and softer due to the principal transversal tensile strain (ε_1). Therefore, in the EPSF approach, the actual compressive strength depends on the adimensional factor (η), which hence depends on the level of transversal tensile strain (ε_1). That is different from the STM approach, which usually assumes that the concrete compressive strength remains constant irrespective of the tensile strain in ULS. ACI 318–19 [1] also considers that the compressive strength value is not dependent on the tensile strain (Table 23.4.3). As the GTM uses the EPFS approach on the FEA analysis, the maximum value of the loss of compressive strength in the concrete (η) can be controlled by the choice of η_{adm} (defined by the designer). Hence, the compressive stress level in concrete elements is checked by Equation (2). If the compressive stress in concrete is higher than the actual compressive strength f_{c2max}, no numerical solutions can be found. That means the designer may need to change parameters such as the, specified concrete compressive strength (f'_c), first trial reinforcement layout, or the cross-section geometry of the member. On the other hand, once the FEA solver finds a valid solution, the compressive stress level in concrete elements is already assessed. The level of stress on the reinforcement bars on the GTM is controlled through the adoption of the admissible reinforcement stress (σ_{adm}), which usually can be taken less or equal to the design value of the reinforcement yield strength (f_{yd}). Finally, the only way to achieve Step 5 (Step 5: Outcome) is by fully satisfying the following criteria: design load, level of stress in the concrete, and level of stress in the reinforcement.

2.4. Step 4: Design decisions

Based on the results of the previous step, this step (Step 4) makes the decisions on whether or not to change the reinforcement layout. These changes can be done either by increasing the section of existing reinforcement bars or by creating a new one. The increase in the cross-sectional area of an existing rebar layer is done either by increasing the rebar diameter or by including additional reinforcements on the same rebar layer. This decision is dictated by the level of stress on the existing rebar layers (verification undertaken in Step 3), considering the availability of rebar diameters and free space in the specimen cross-section. The logical tests used to accomplish this task are shown in Fig. 2, where φ_r is the required rebar diameter, φ_a is available rebar diameter, n_r is the required number of rebar and n_a is the available number of rebar. After increasing the number of existing reinforcement bars, the finite element mesh may change, in order to comply with these changes. No re-meshing is required if no rebar is added. The area increase of existing reinforcement bars can be made directly on the mesh file by changing the equivalent cross-section.

The last decision-making function in this step is the creation of new reinforcement bars. This action is driven by the allowed level of tensile strain acting in the concrete. The logical test of this function is to check whether $\eta > \eta_{adm}$ is true (see Fig. 2). If the adimensional factor which decreases the concrete compressive capacity based on the transversal tensile strain (η) is lower than the η_{adm} (adopted by the designer) the

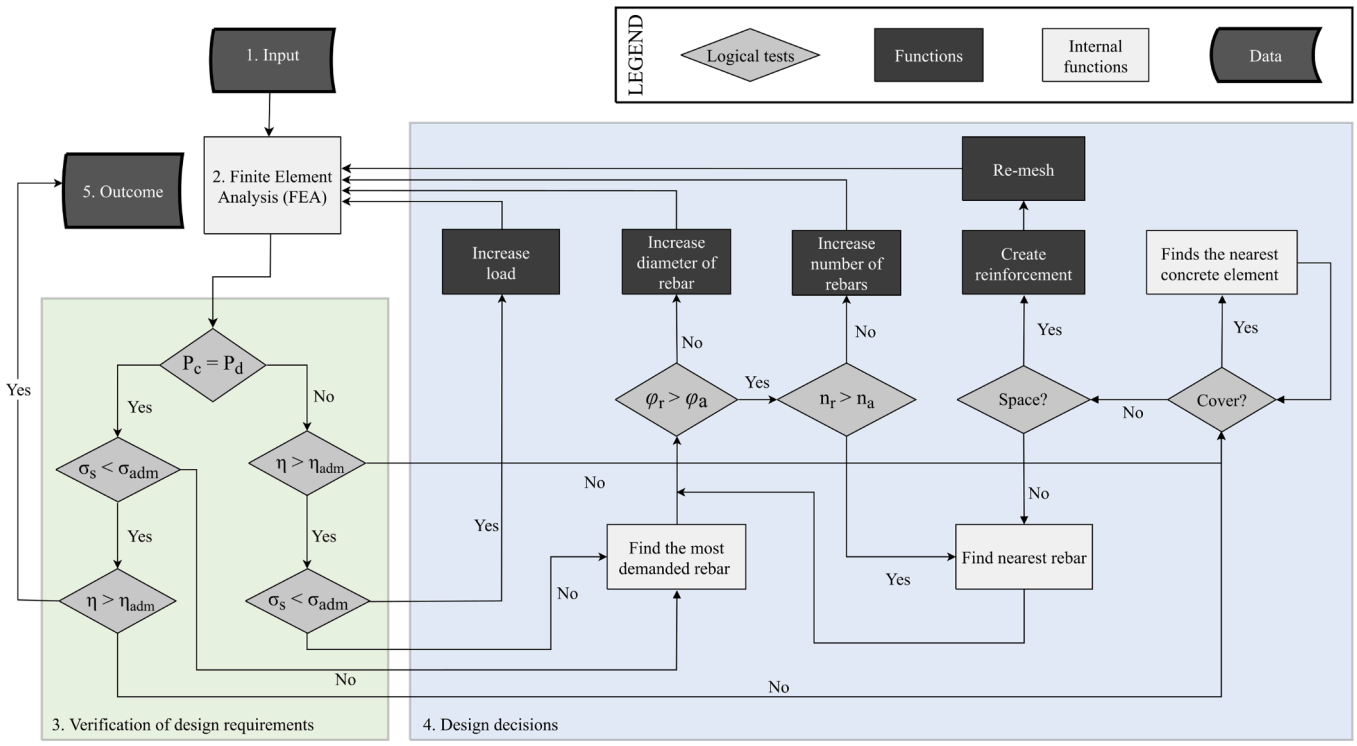

Fig. 2. The Generative Tie Method (GTM) complete algorithm.

creation function is triggered (see Equation (1)). By default, the orientation of this new rebar is aligned with the principal tensile strain direction of the analyzed concrete element. However, the designer may allow or lock directions in this function in order to avoid unpractical reinforcement layouts. The algorithm combines the principal tensile strain direction with the allowed directions informed by the designer. After the creation of new reinforcement bars and before the new FEA, a new mesh generation is required. Once both concrete and reinforcement design requirements are satisfied (see Fig. 2), the current step increases the load and goes back to the FEA (Step 2) and then goes to Step 3 again. The GTM keeps going back and forth between Step 2 and Step 4 until all Step 3 checks are completely satisfied.

2.5. Step 5: Outcome

The outcome is reached only through Step 3 (see Fig. 2). And this happens after the current/analyzed load matches with the design load, and the reinforcement bars and concrete elements show safe stress levels. The compilation of these three conditions is presented in Equation (3).

$$\begin{cases} P_c = P_d \\ \quad and \\ \sigma_s < \sigma_{adm} \\ \quad and \\ \eta > \eta_{adm} \end{cases} \tag{3}$$

In Equation (3), P_c is the current/analyzed load according to GTM, P_d is the design load, σ_s is the maximum stress acting at the rebar in the analyzed model according to the GTM, σ_{adm} is the admissible reinforcement stress according to the GTM, η is the minimum value of the dimensionless factor which decreases the concrete compressive capacity according to the MCFT, and η_{adm} is the admissible value of the loss of compressive strength in the concrete according to the GTM.

3. Design of deep beams based on the Generative Tie Method

The design of four deep beam specimens was carried out in order to apply the GTM. The specimens were inspired by the series of deep beams studied by Birrcher et al. [21] with the shear span-depth ratio (a/d) of 1.2. A scale factor of 2 was applied to the specimens in order to reduce the size of specimens. The details of the specimens are shown in Fig. 3 a) and b). The design load (P_d) adopted for the studied specimens was 720 kN. The specified concrete compressive strength (f'_c) was assumed to be 40 MPa. The concrete equivalent plastic strength was obtained from the equation used by Ruiz & Muttoni [23]. The maximum aggregate size of 12.7 mm (1/2 in) was considered. The reinforcement cage was built by 10 M, 20 M, 25 M, and 30 M of 400 W steel bars [2,27] with specified reinforcement yield strength (f_y) of 400 MPa. The maximum allowed tensile strain in the concrete was the only design parameter that varied between these four specimens. The η_{adm} ranging from 0.75 to 0.9 sought to study the effect of this variable on the designed reinforcement layout. The values of η_{adm} used for these specimens are presented in Table 1.

The minimum distributed reinforcement (MDR) was designed according to ACI 318–19 [1]. The reinforcement details are presented in Fig. 3 c) and Fig. 3 d). The deep beams were modeled using the 2D mesh generator named *imesh* [25]. To avoid unpractical reinforcement layouts, the creation of new rebar was allowed only in the directions of existing reinforcements (longitudinal and transversal) as illustrated in Fig. 3 c) and d). No inclined reinforcements were allowed to be created.

For all studied specimens, the design load of 720 kN was divided into 72 increments of 10 kN ($N^{\circ}_{LS} = 72$). The creation of an additional stirrup on the design of the first deep beam (SII.a) is presented in Fig. 4. Under the applied load of 650 kN, specimen SII.a exhibited the value of η as 0.73 in a concrete finite element, see Fig. 4 c). As shown in Fig. 2, the creation of new rebar is requested when $\eta \leq \eta_{adm}$. The angle of the main tensile strain direction located in this over-solicited element was found to be 37° with the horizontal axis. Therefore, the main strain direction is closer to the horizontal than the vertical direction. Hence, according to the GTM algorithm, the chosen direction for the creation of the new

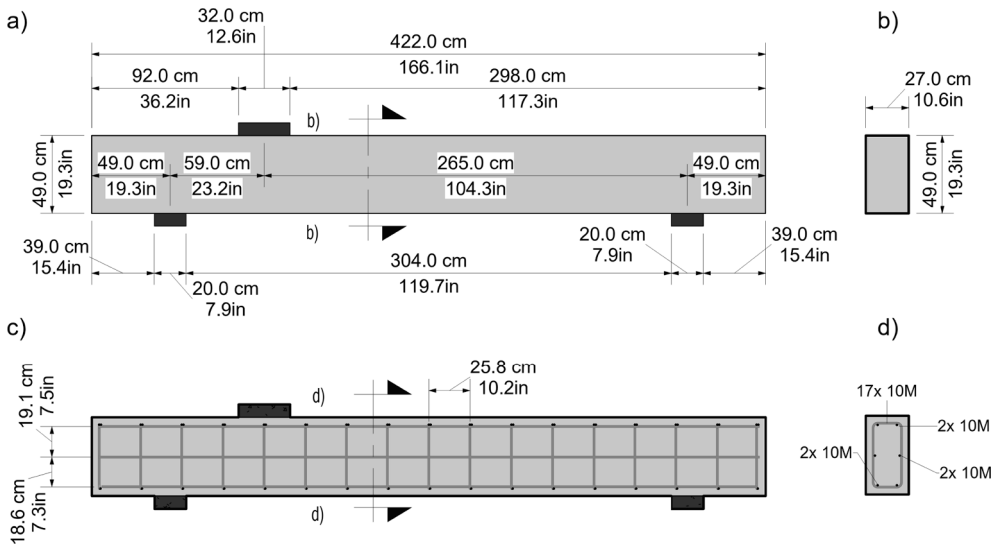

Fig. 3. Studied deep beam: a) side view; b) cross-section; c) side view of the minimum distributed reinforcement detailing; and d) cross-section of the minimum distributed reinforcement detailing.

Table 1
Design parameters for the studied deep beams.

Specimen	η_{adm}
SII.a	0.75
SII.b	0.80
SII.c	0.85
SII.d	0.90

rebar would be horizontal. However, at this load (650 kN) the GTM had already heavily reinforced the flexural bars (horizontal reinforcements) in such a way that there was no more space for placing horizontal new reinforcement bars. Hence, the GTM algorithm had to increase the specimen's strength through the creation of new vertical rebar (closed stirrup). In Fig. 4 d), this new rebar is highlighted. The presence of such new vertical rebar changed the stress fields, given that the newly included rebar is sharing a considerable level of tensile stress (see Fig. 4 e)). This action caused the decrease of the concrete main tensile strain. The η map after the change presented in Fig. 4 f) shows a value of 0.81 for the minimum η in the analyzed region, which ensures that the loss of compressive strength is under control (greater than η_{adm}).

After a new finite element analysis (FEA) on the new model (with the new stirrup), Step 3 (*Step 3: Verification of* the design requirements) was undertaken again and then the analyzed load was increased through Step 4 (*Step 4*: Design decisions), see Fig. 1 and Fig. 2. All this workflow

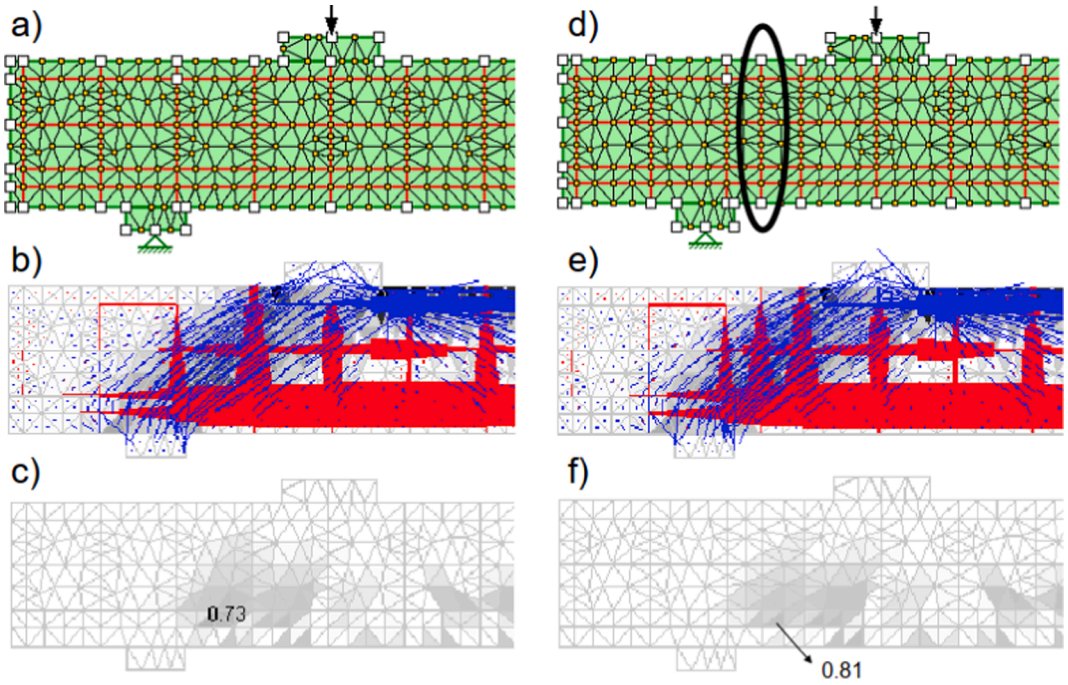

Fig. 4. GTM application on the design of SII.a. a) finite element mesh for the first trial model; b) stress distribution on the first trial under the applied load of 650 kN; c) map of η on the first trial model under the applied load of 650 kN; d) finite element mesh for the GTM-changed model; e) stress distribution on the GTM-changed model under the applied load of 650 kN; and f) map of η on the GTM-changed model under the applied load of 650 kN.

is repeated until the analyzed load reaches the design load ($P_d = 720$ kN). The application of GTM for the three other specimens (SII.b, SII.c, and SII.d) was carried out using the same approach, however, different η_{adm} values were chosen as shown in Table 1. The key information of the design decisions done by GTM along the design of the four studied specimens can be found in

Table 2. Steps with no design decisions were merged into one row. In the second column of

Table 2 is shown the minimum value of the adimensional factor which decreases the concrete compressive capacity found on the current analysis (η), according to MCFT. The third column shows whether or not reinforcement yielding occurred. The GTM functions (see Fig. 2) applied in each step are presented in the fourth column under the following labeling pattern: a) Increase load; b) Create reinforcement; c) Increase diameter; d) Outcome. The last column shows the location of the GTM design decisions employed in each step or range of steps. The labeling pattern used in that column is: I) a stirrup between the load and the left support; II) a stirrup between the load and the right support; III) various stirrups between left and right support; IV) various stirrups between the load and the left support; V) various stirrups between the load and the right support; VI) various stirrups between the load and the left support went from 2 legs to 4 legs. The reinforcement layouts of all four specimens are shown in Fig. 5. All the changes made by the GTM in the four specimens can be found in Video 1.

4. Experimental program

The experimental program was carried out using a large-scale test setup in the Structural Engineering Laboratory (SEL) at the University of Windsor, Ontario, Canada. Reinforcement bars 10 M, 20 M, 25 M, and 30 M made out of 400 W steel were used in all reinforced concrete elements [27]. The material tests were conducted according to [28] on the batch of reinforcement bars used in this research. The results exhibited the yield stress of 495.1 MPa, ultimate stress of 730.5 MPa, and modulus of elasticity of 269.2 GPa. According to the procedures established in [29], the experimental concrete compressive strength ($f_c^{'}exp$) determined through the cylinder test was 43.2 MPa.

4.1. Specimen preparation

The specimens were cast into a set of plywood formwork as shown in Fig. 6 a) and Fig. 6 b). The reinforcement cages were built as shown in the detailing presented in Fig. 5. Eleven 5-mm strain gauges for steel were properly attached to the reinforcement cages before casting the concrete. The location of the strain gauges is shown in Fig. 7 a). After curing for 28 days, the specimens were removed from the formwork as shown in Fig. 6 c). In order to use the digital image correlation (DIC) technique, a stochastic pattern (speckle) painting was applied on the front surface of each specimen.

4.2. Test setup

Linear Variable Differential Transformers (LVDT) were used to capture vertical displacements at three points underneath each specimen as shown in Fig. 7 a). The pin and roller boundary conditions were applied to supports A and B, respectively. A loading actuator with a capacity of 3000 kN was attached to a high-strength reaction frame (blue frame). As shown in Fig. 7 b) three digital cameras were mounted and connected to the data acquisition system (DAQ) to capture images of the front face of each specimen. The images were collected every 4 s during the tests. The photographs were later processed in a DIC software named *GOM correlate* [30]. Besides the eleven 5-mm strain gauges attached to the reinforcement cage, three more surface strain gauges were used in each specimen. These three strain gauges were attached to the back surface of the specimens to monitor the concrete surface strains as shown in Fig. 8. The values obtained from them were used to calibrate and validate the DIC results. An additional LVDT was attached to the load actuator to control its stroke during the tests. Fig. 9 shows a photograph of a specimen mounted on the test setup.

4.3. Test results

The shear force scheme can be found in Fig. 10. The loading scheme is presented in Fig. 10 a). The shear forces diagram resulting from the self-weight of the deep beam is shown in Fig. 10 b). The shear force diagram for the applied load (P_i) is presented in Fig. 10 c). The relationship between the critical shear force (V_i) and the applied load (P_i) is

Table 2
History of design decisions undertaken by GTM.

Load steps	η	Reinf. Yielded	Function	Design Decisions	Load steps	η	Reinf. Yielded	Function	Design Decisions
		SII.a					SII.b		
0–66	>0.75	no	a	–	0–52	>0.80	no	a	–
67	0.71	yes	b	I	53	0.79	no	b	I
67–69	>0.75	no	a	–	53–59	>0.80	no	a	–
70	0.74	yes	b	I	60	0.79	no	b	II
70–71	>0.75	no	a	–	60–64	>0.80	no	a	–
72	0.76	no	d	–	65	0.79	no	b	III
					65–71	>0.80	no	a	–
					72	0.81	no	d	–
		SII.c					SII.d		
0–44	>0.85	no	a	–	0–41	>0.90	no	a	–
45	0.8	no	b	I	42	0.89	no	b	I
45–49	>0.85	no	a	–	42–49	>0.90	no	a	–
50	0.84	no	b	II	50	0.89	no	b	IV
50–52	>0.85	no	a	–	50–52	>0.90	no	a	–
53	0.84	no	b	I	53	0.89	no	b	IV
53–54	>0.85	no	a	–	53–54	>0.90	no	a	–
55	0.84	no	b	II	55	0.89	no	b	V
55–59	>0.85	no	a	–	55–59	>0.90	no	a	–
60	0.84	no	b	II	60	0.89	no	b	III
60–64	>0.85	no	a	–	60–64	>0.90	no	a	–
65	0.84	no	b	III	65	0.89	no	b	III
65–71	>0.85	no	a	–	65–69	>0.90	no	a	–
72	0.81	no	d	–	70	0.89	no	c	VI
					70–71	>0.90	no	a	–
					72	0.91	no	d	–

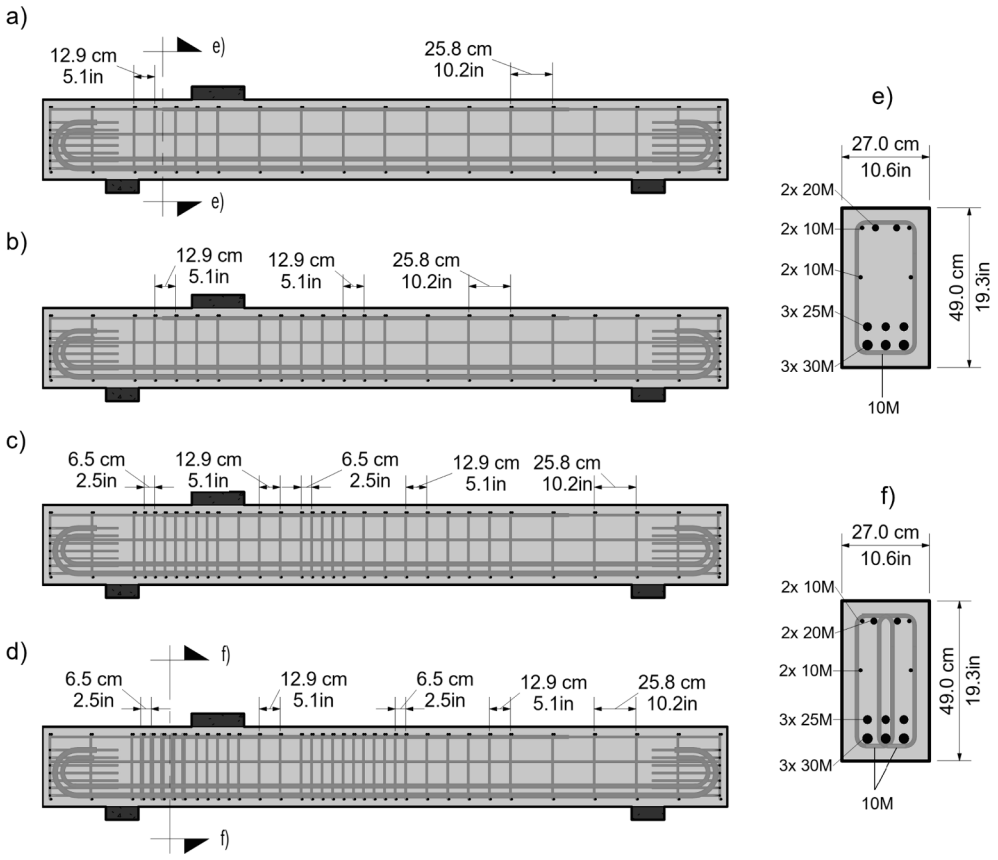

Fig. 5. Reinforcement detailing: a) SII.a side view; b) SII.b side view; c) SII.c side view; d) SII.d side view; e) SII.a, SII.b and SII.c cross-section; and f) SII.d cross-section.

Fig. 6. Specimens preparation: a) formwork and reinforcement cage before the concrete casting; b) specimens after the concrete casting; and c) specimens after the concrete curing.

expressed in kN in Equation (4) (see Fig. 10).

$$V_i = 0.818 \times P_i + 4.4 \quad (4)$$

The weight of steel reinforcement used in each specimen ($W_{reinf.}$) can be found in Table 3. The strut angles at the experimental ultimate applied load ($\varnothing_{strut}$) expressed in degrees are also shown in Table 3. These are the angles between the horizontal and the principal compressive strain direction in the critical shear region. These values were obtained using the DIC data. The maximum crack width at the ultimate applied load (CW_{test}) is shown in millimeters in Table 3. The crack widths were also obtained using the DIC data similar to what was used by other researchers [31,32]. The applied load while reinforcement reaches the yielding (P_y), as well as the experimental ultimate applied load (P_{test}) in each tested specimen, can be found in Table 3. The applied load that causes the development of the first crack of 0.1 mm width (P_{crack}) is also shown in Table 3. The critical shear force corresponding to P_{test} is represented as V_{test}. The critical shear force corresponding to P_{crack} is represented by V_{crack}. Equation (4) was used to calculate V_{test} and V_{crack} depending on P_{test} and P_{crack}, respectively. Both V_{test} and V_{crack} are also presented in Table 3. The predictions for the ultimate applied load and the critical shear force according to the EPSF approach can be found in Table 3 by P_{EPSF} and V_{EPSF}, respectively. Using the estimative of service load as a function of experimental failure load (P_{test}), from Birrcher et al. [21] (0.33 factor), service loads (P_s) for each specimen can be found in Table 3. The crack widths measured for each specimen under the service load are also presented in Table 3.

Table 4 presents four nondimensional performance indexes for each specimen. The ratio between the experimental ultimate applied load (P_{test}) and the applied yielding load (P_y) is called in this paper the hardening index (I_h). This index is expressed as (P_{test}/P_y) and indicates how far the failure happened in relation to the yielding during the test.

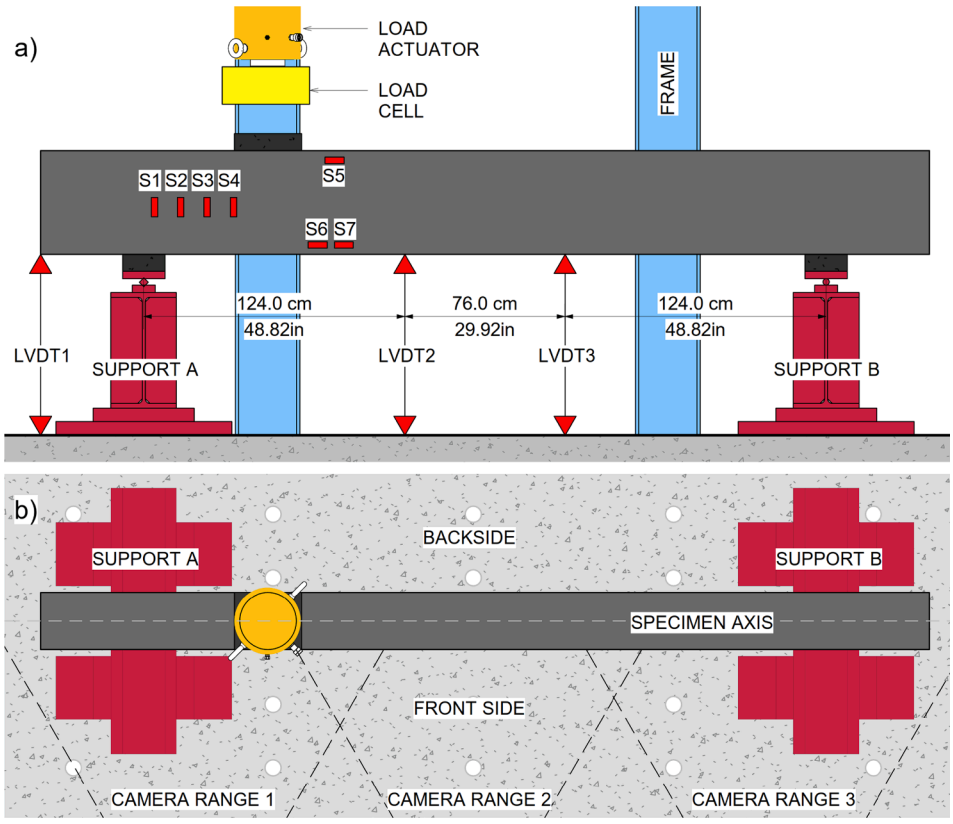

Fig. 7. Test setup. a) front side view; b) top view.

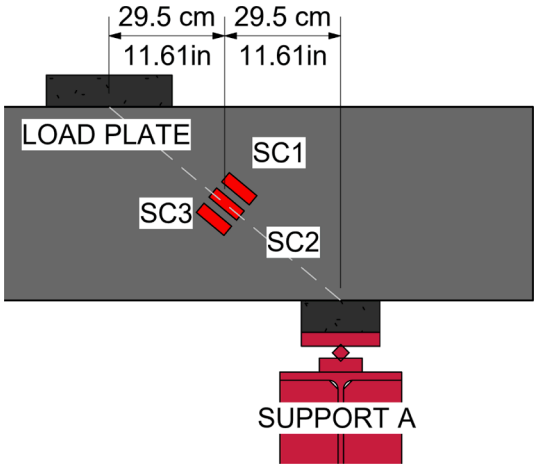

Fig. 8. Test setup backside side view.

The second index is expressed as (V_{test}/V_{EPSF}) and is called ultimate index (I_u). This index compares the experimental critical shear force with the predicted ultimate shear force (V_{EPSF}). The prediction was done according to the EPSF through the FEA solver (*jconc*) both developed by Ruiz & Muttoni [23]. The cracking index (I_c) measures how early the crack appears in relation to the experimental ultimate applied load. This index is expressed as (P_{crack}/P_{test}). The normalization of the critical shear force (V_{test}) equation used by Birrcher et al. [21] was employed to express the shear index (I_s) in this paper. The referred equation was adapted from Birrcher et al. [21] in Equation (5). The width of the deep beams in Equation (5) is represented by b_w.

$$I_s = \frac{V_{test}}{f_c' \times b_w \times d} \tag{5}$$

The cracking patterns formed during the tests correlate to the principal tensile strain plot from the DIC. Fig. 11, Fig. 12, and Fig. 13 show the principal tensile strain plot at the load level of 510 kN, 720 kN, and ultimate load (P_{test}) for each tested specimen, respectively. Video 2 shows the evolution of the crack pattern along the entire length of the specimens throughout the experimental tests. The DIC plots were obtained using *GOM correlate* software [30]. Fig. 14 shows all the four tested specimens after the unloading. The initial yielding occurred at different locations for each deep beam. For specimens SII.a and SII.b the reinforcement yielding started in the S1 position (see Fig. 7 a). For specimens SII.c and SII.d, the yielding first occurred close to the S2 position (see Fig. 7 a). The strain *versus* applied load plot for the main stirrup of each specimen is shown in Fig. 15. Fig. 16 shows the history of the maximum crack opening of each specimen throughout the tests. Fig. 17 shows the applied load (P_i) *versus* vertical displacement at the LVDT2 position (see Fig. 7 a) curves for each tested deep beam.

5. Discussion

The results have shown that the higher η_{adm} is, the higher is the use of steel ($W_{reinf.}$). Hence, the choice of η_{adm} on the GTM influences the required amount of reinforcement ($W_{reinf.}$) to satisfy the design parameters. As can be found in Table 3, a greater amount of transversal reinforcement ($W_{reinf.}$) leads to an increase in the strut angle at P_{test} ($\varnothing_{strut}$). All four tested specimens presented failure by crushing the concrete strut between the load plate and the support A (see Fig. 14). The highlights of the performance of each specimen are presented below.

The specimen SII.a has shown the lowest value of P_{crack} (156.0 kN) and also the lowest cracking index value, I_c equal to 0.13. Within the tested specimens, the highest maximum crack opening at P_{test} (CW_{test}) was also found in specimen SII.a and this crack width was found to be 2.40 mm. However, SII.a had the lowest reinforcement amount (191.1 kg) and reached out the highest ductility index (1.46). This means that

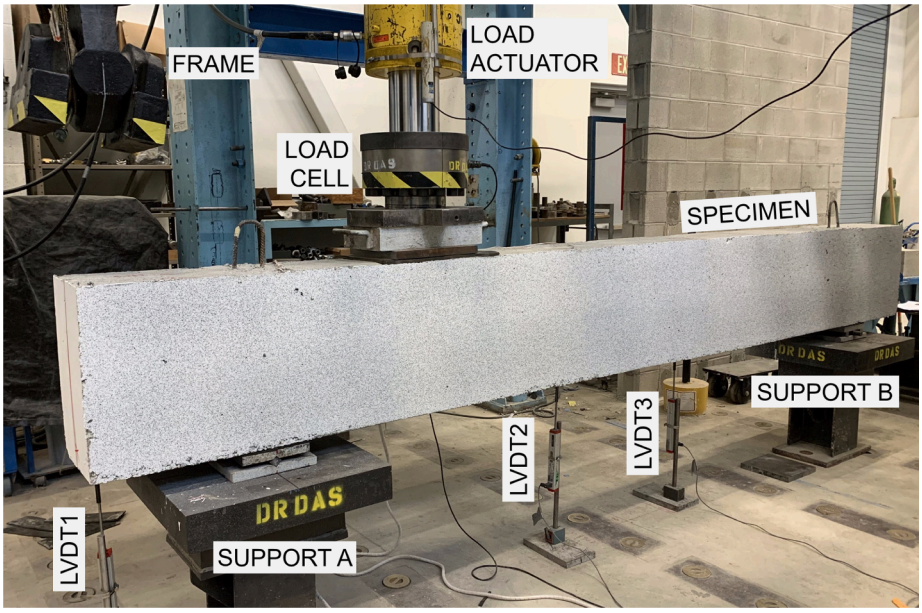

Fig. 9. Photograph of the test setup.

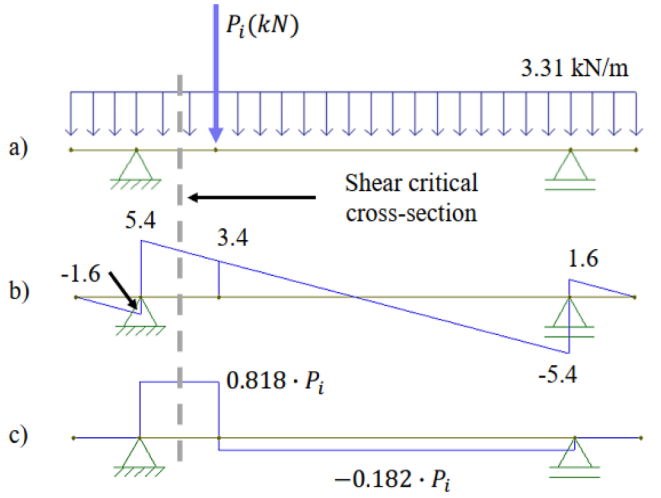

Fig. 10. Shear force analysis scheme: a) deep beam loading scheme; b) shear force diagram for deep beam's self-weight; and c) shear force diagram for the applied load (P_i).

the failure for specimen SII.a occurred at a load 46% higher than the yielding load (P_y).

Specimen SII.b exhibited the lowest yielding (P_y) and failure load (P_{test}), at 809.5 kN and 1079.0 kN, respectively. With these results, specimen SII.b presented the lowest shear index value (0.20) among all four tested deep beams. On the other hand, specimen SII.b reached the highest cracking load (P_{crack}) among all the specimens (240.2 kN). This means that specimen SII.b exhibited the highest cracking index value (0.22) among all the tested specimens.

Specimens SII.c and SII.d have presented the maximum crack width at P_{test} (CW_{test}) lower than 1 mm. The CW_{test} value obtained for specimens SII.c and SII.d was 0.89 and 0.68 mm, respectively. Besides that, specimen SII.d showed the highest P_{test} and P_y, which led to the highest values for the shear index (0.24). Both P_{test} and P_y were found to be equal to 1331.9 kN. Hence, specimen SII.d presented the lowest value of hardening index (I_h), which was found to be 1. The quasi-brittle behavior (P_{test} equal to P_y) exhibited by specimen SII.d can also be observed in the load–displacement curve shown in Fig. 17. Finally, specimen SII.d showed the largest steel consumption, with a reinforcement cage of 212.2 kg.

6. Conclusions

The main goal of this study is the proposal of the Generative Tie Method (GTM) on the design of reinforced concrete deep beams. A large-scale experimental investigation was carried out on four specimens designed by the GTM. The main conclusions of this paper can be summarized as follows:

Table 4
Performance indexes.

Sp.	$I_h = \frac{P_{test}}{P_y}$	$I_u = \frac{V_{test}}{V_{EPSF}}$	$I_c = \frac{P_{crack}}{P_{test}}$	$I_s = \frac{V_{test}}{f_c b_w d}$
SII.a	1.46	1.07	0.13	0.22
SII.b	1.33	0.91	0.22	0.20
SII.c	1.06	0.97	0.18	0.21
SII.d	1.00	1.00	0.17	0.24

Table 3
Test results.

Sp.	$W_{reinf.}$ (kg)	$\varnothing_{strut}$ (°)	CW_{test} (mm)	P_y (kN)	P_{test} (kN)	V_{test} (kN)	P_{crack} (kN)	V_{crack} (kN)	P_{EPSF} (kN)	V_{EPSF} (kN)	P_s (kN)	CW_s (mm)
SII.a	191.1	38.7	2.40	818.1	1191.3	978.9	156.0	132.0	1108.6	911.2	393.1	0.3
SII.b	194.1	40.8	1.88	809.5	1079.0	887.0	240.2	200.8	1185.3	974.0	356.1	0.2
SII.c	204.2	41.4	0.89	1100.2	1165.6	957.9	207.7	174.3	1199.1	985.3	384.6	0.2
SII.d	212.2	44.2	0.68	1331.9	1331.9	1093.9	229.5	192.1	1332.5	1094.4	439.5	0.2

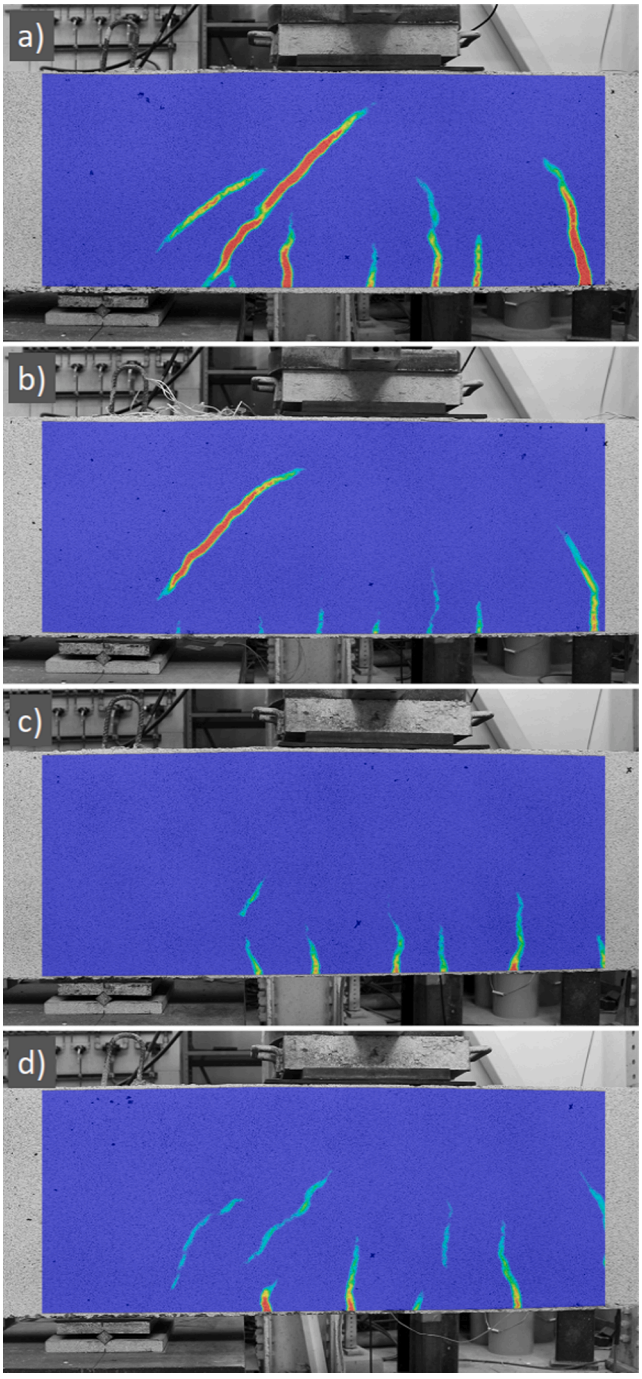

Fig. 11. Principal tensile strain obtained from DIC at the load level of 510 kN. a) SII.a; b) SII.b; c) SII.c; d) SII.d.

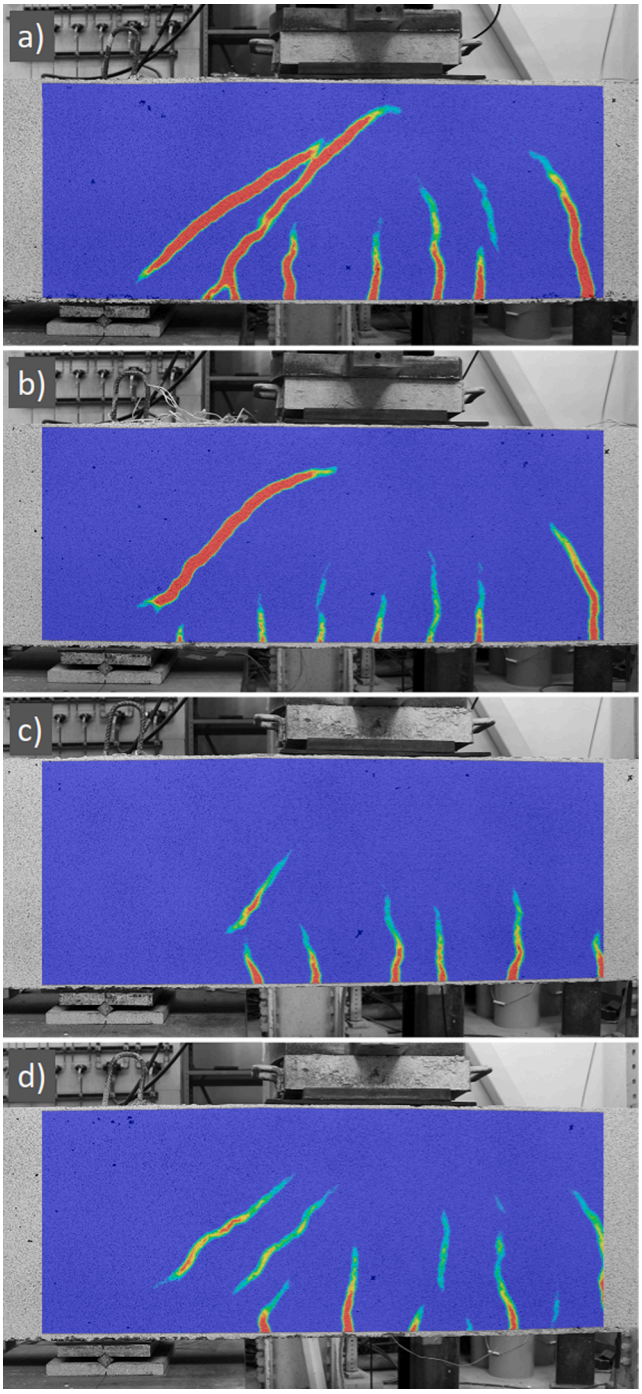

Fig. 12. Principal tensile strain obtained from DIC at the load level of 720 kN. a) SII.a; b) SII.b; c) SII.c; d) SII.d.

1. The major advantage of the proposed method (GTM) over existing methods to optimize the reinforcement layout design [14–17] is the ability to create new reinforcement positions through the choice of η_{adm}. The framework proposed by Amir & Sigmund [14] for instance, has shown great results, but it relies on the ground reinforcement arrangement. However, GTM uses the principal tensile strain orientation of the most critical concrete element to create a new reinforcement position.
2. The strength capacity predictions of the deep beams conducted through the EPSF approach proposed by Ruiz & Muttoni [23], showed well agreements with the experimental results. The relationship between the experimental critical shear force with the predicted critical shear force (I_u) ranged from 0.91 (SII.b) to 1.07 (SII.a).
3. From the practical examples of GTM application, it can be noticed that greater values of η_{adm} cause a greater reinforcement consumption for the same design load. The experimental results have shown decreases in the hardening index (I_h) when greater values of η_{adm} is assumed. As shown in Table 4, the hardening index (I_h) ranged from 1.46 (η_{adm}= 0.75) to 1.00 (η_{adm} = 0.90).
4. The strut angle (principal compressive strain direction) ranged from 38.7° at SII.a to 44.2° at SII.d (see Table 3). All the tested specimens presented failure by crushing the concrete strut between the load plate and the support A (see Fig. 14). The failure mode observed

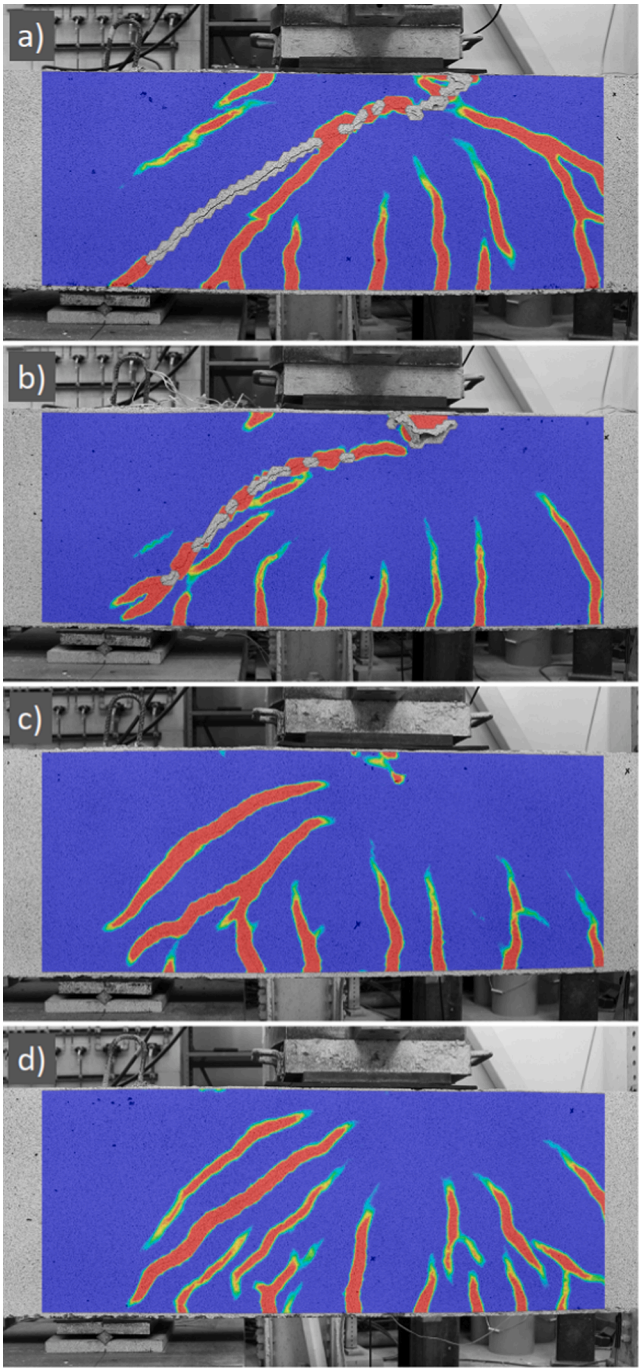

Fig. 13. Principal tensile strain obtained from DIC at ultimate load (P_{test}). a) SII.a; b) SII.b; c) SII.c; d) SII.d.

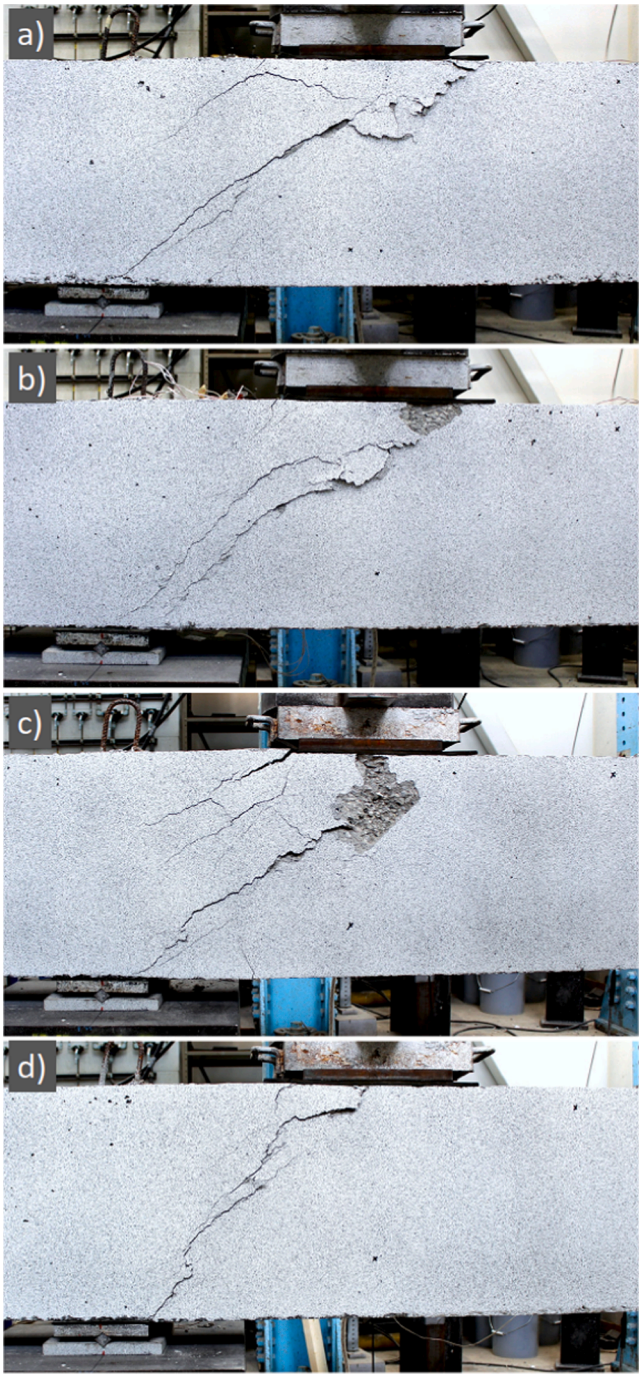

Fig. 14. Specimens after the test (unloaded). a) SII.a; b) SII.b; c) SII.c; d) SII.d.

matches well with the results presented by Birrcher et al. [21] for tested specimens with the same shear span-depth ratio ($a/d = 1.2$).

5. Although all the tested specimens showed similar failure modes, the number of cracks and their widths differed from one another. The experimental results have shown that the relationship between the amount of reinforcement and the maximum crack width at P_{test} (CW_{test}) is inversely proportional.
6. In the conclusions presented by Birrcher et al. [21], a minimum web reinforcement ratio of 0.3% was suggested for deep beams, rather than the ACI recommendation [1] of 0.25%. One of the arguments of this recommendation is based on the restriction of crack widths. According to Birrcher et al. [21] at the service load is desirable (not a recommendation) crack widths less than 0.4 mm (0.016 in). The experimental results of the present study revealed maximum crack widths of 0.3 mm under the service load for specimen SII.a. For the other specimens, the same value was 0.2 mm. Therefore the craking level of the studied deep beams can be controlled by the GTM, even using the minimum web reinforcement recommendation from ACI 318–19 [1] (0.25%).
7. The proposed method (GTM) allows the structural designer to control the level of tensile strain in the concrete by manipulating (changing/setting) the value of η_{adm}. The appropriate choice of η_{adm} for the Generative Tie Method framework can be an effective way of controlling the allowed crack widths. Different performances (outcomes) for each adopted η_{adm} were noticed in this investigation (see Video 2). The GTM is capable of addressing unusual design

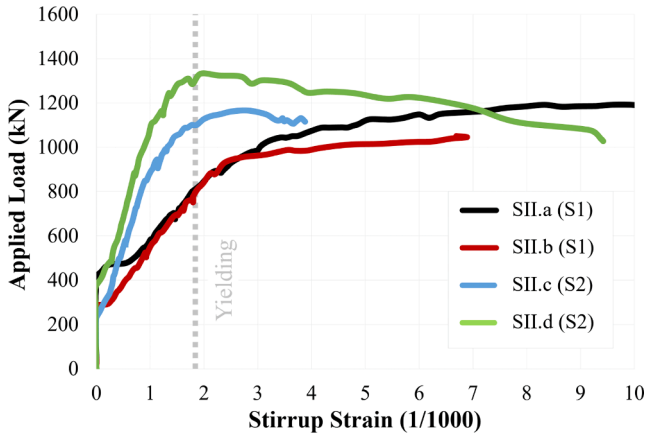

Fig. 15. Applied load (P_i) *vs.* stirrup strain curve for each tested specimen.

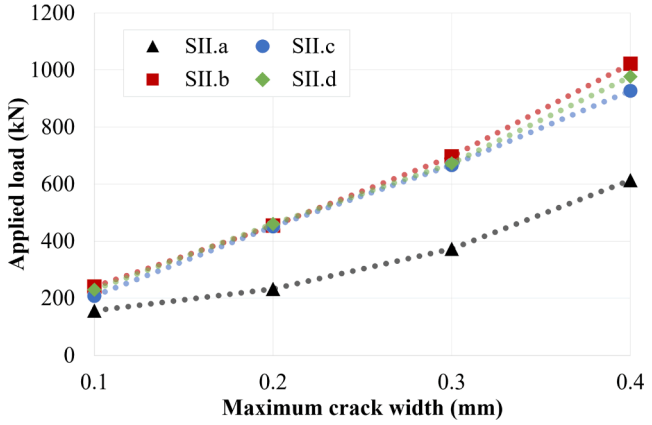

Fig. 16. Applied load (P_i) *vs.* maximum crack width (CW_i) curve.

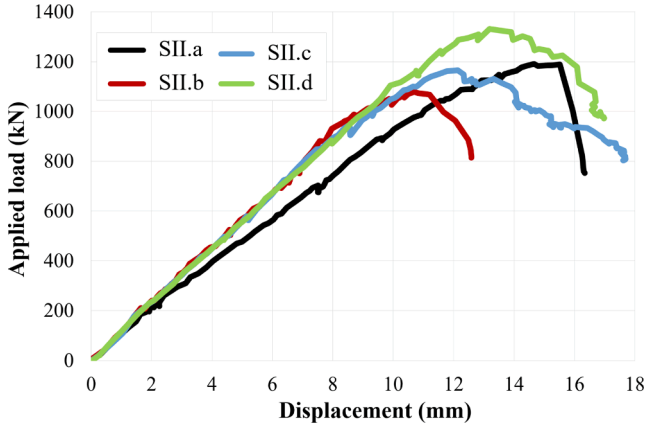

Fig. 17. Applied load (P_i) *vs.* vertical displacement curve at LVDT2 position for all tested specimens.

requirements, such as structures subjected to severe environmental conditions, in which the requirements for cracking control are stricter.

In order to better explore the Generative Tie Method potential, it is recommended further investigation of different levels of η_{adm} for this type of deep beam. Other shear span-depth ratios (a/d) should be investigated as well. The STM relies on the experience of the structural designer, which may not always lead to the most optimized outcome. The GTM bases decisions on FEA and provides tools for the designer to address serviceability issues (such as cracking) more accurately. This characteristic of the GTM allows the designer to make better use of the potential of reinforced concrete members.

Furthermore, the entire GTM process is computer-driven, which allows its implementation together with advanced design techniques such as generative design. Therefore, a technique to dissipate a possible tensile strain concentration on certain concrete elements, intrinsic to numerical solutions, should be incorporated into the proposed method to avoid discrepancy in the calculation of η. Finally, the proposed technique has shown promising results, and shapes never seen before should be designed and investigated by the GTM in future investigations.

CRediT authorship contribution statement

Marcos V.G. Silveira: Writing – original draft, Writing – review & editing, Conceptualization, Methodology, Formal analysis, Investigation. **Bruno Paini:** Writing – review & editing, Methodology, Formal analysis, Investigation. **Luís A.G. Bitencourt Jr:** Writing – review & editing, Supervision, Formal analysis, Software, Visualization. **Sreekanta Das:** Writing – review & editing, Resources, Funding acquisition, Project administration, Supervision.

Declaration of Competing Interest

The authors declare that they have no known competing financial interests or personal relationships that could have appeared to influence the work reported in this paper.

Acknowledgments

The authors wish to acknowledge the Emerging Leaders in the Americas Program (ELAP) for the scholarship provided to Mr. Marcos V. G. Silveira. This study was financed in part by the Coordenação de Aperfeiçoamento de Pessoal de Nível Superior – Brasil (CAPES) – Finance Code 001. As well, the cost of all the experimental work was supported by NSERC through Dr. Sreekanta Das. Dr. Luís A.G. Bitencourt Jr. would also like to extend his acknowledgments to the financial support of the National Council for Scientific and Technological Development – CNPq (Proc. N°: 310401/2019-4). The authors further recognize the help of the Structural Engineering Laboratory technical staff members, Mr. Matthew St. Louis and Mr. Jerome Finnerty. Finally, the authors would like to thank Autodesk Technology Centers for access to an innovation community that helped increase this research impact.

Appendix A. Supplementary data

Supplementary data to this article can be found online at https://doi.org/10.1016/j.engstruct.2022.113913.

References

[1] American Concrete Institute, 318-19 Building Code Requirements for Structural Concrete and Commentary, American Concrete Institute, 2019. https://doi.org/10.14359/51716937.
[2] Canadian Standards Association, Design of Concrete Structures CSA A23.3-14, 2014.
[3] Associação Brasileira de Normas Técnicas, ABNT NBR 6118: Projeto de estruturas de concreto - Procedimento, In portuguese, 2014. https://www.abntcatalogo.com.br/norma.aspx?ID=317027.
[4] European Standard, BS EN 1992-1-1: Eurocode 2 Design of concrete structures - Part 1-1: General rules and rules for buildings, 2004. https://eurocodes.jrc.ec.europa.eu/showpage.php?id=132.
[5] Schlaich J, Schafer K, Jennewein M. Toward a Consistent Design of Structural Concrete. PCI J 1987;32(3):74–150.
[6] Ali MA, White RN. Automatic generation of truss model for optimal design of reinforced concrete structures. ACI Struct. J. 2001. https://doi.org/10.14359/10286.

[7] H.E. Fairclough, T.J. Pritchard, L. He, M. Gilbert, LayOpt: A truss layout optimization web application, (2020). https://www.layopt.com (accessed July 24, 2020).
[8] Liang QQ, Xie YM, Steven GP. Topology Optimization of Strut-and-Tie Models in Reinforced Concrete Structures Using an Evolutionary Procedure. ACI Struct. J. 2000;97. https://doi.org/10.14359/863.
[9] Liang QQ, Xie YM, Steven GP. Generating Optimal Strut-and-Tie Models in Prestressed Concrete Beams by Performance-Based Optimization. ACI Struct. J. 2001;98. https://doi.org/10.14359/10191.
[10] Guan H. Strut-and-tie model of deep beams with web openings - An optimization approach. Struct. Eng. Mech. 2005;19(4):361–79.
[11] Guan H, Doh J-H. Development of Strut-And-Tie Models in Deep Beams with Web Openings. Adv. Struct. Eng. 2007;10(6):697–711. https://doi.org/10.1260/136943307783571427.
[12] Herranz JP, Santa Maria H, Gutierrez S, Riddell R. Optimal Strut-and-Tie Models Using Full Homogenization Optimization Method. ACI Struct. J. 2012;109. https://doi.org/10.14359/51684038.
[13] Bruggi M. A numerical method to generate optimal load paths in plain and reinforced concrete structures. Comput. Struct. 2016;170:26–36. https://doi.org/10.1016/j.compstruc.2016.03.012.
[14] Amir O, Sigmund O. Reinforcement layout design for concrete structures based on continuum damage and truss topology optimization. Struct. Multidiscip. Optim. 2013;47(2):157–74. https://doi.org/10.1007/s00158-012-0817-1.
[15] Amir O, Shakour E. Simultaneous shape and topology optimization of prestressed concrete beams. Struct. Multidiscip. Optim. 2018;57(5):1831–43. https://doi.org/10.1007/s00158-017-1855-5.
[16] Zelickman Y, Amir O. Layout optimization of post-tensioned cables in concrete slabs. Struct. Multidiscip. Optim. 2021;63(4):1951–74. https://doi.org/10.1007/s00158-020-02790-2.
[17] Fib Fédération internationale du béton, Bulletin No.100: Design and assessment with strut-and-tie models and stress fields: from simple calculations to detailed numerical analysis., Fédération internationale du béton, 2021. https://doi.org/10.35789/fib.BULL.0100.
[18] de Barros VP, Beck AT, Bittencout TN. Shear failure in reinforced concrete members without transverse reinforcement: analysis of model error of NBR6118: 2014. IBRACON Struct. Mater. J. 2021;14. https://doi.org/10.1590/s1983-41952021000100012.
[19] D. Birrcher, R. Tuchscherer, M. Huizinga, O. Bayrak, S. Wood, J. Jirsa, Strength and Serviceability Design of Reinforced Concrete Deep Beams, 2009.
[20] Tuchscherer R, Birrcher D, Huizinga M, Bayrak O. Distribution of Stirrups across Web of Deep Beams. ACI Struct. J. 2011;108. https://doi.org/10.14359/51664208.
[21] Birrcher DB, Tuchscherer RG, Huizinga M, Bayrak O. Minimum Web Reinforcement in Deep Beams. ACI Struct. J. 2013;110. https://doi.org/10.14359/51684409.
[22] Vecchio FJ, Collins MP. The Modified Compression-Field Theory for Reinforced Concrete Elements Subjected to Shear. ACI J. 1986;83. https://doi.org/10.14359/10416.
[23] Ruiz MF, Muttoni A. On development of suitable stress fields for structural concrete. ACI Struct. J. 2007;104:495–502. https://doi.org/10.14359/18780.
[24] Muttoni A, Ruiz MF, Niketic F. Design versus assessment of concrete structures using stress fields and strut-and-tie models. ACI Struct. J. 2015;112:605–15. https://doi.org/10.14359/51687710.
[25] A. Muttoni, O. Burdet, N. Kostic, M.F. Ruiz, i-concrete project, Syst. Stress Fields Dev. Concr. Struct. (n.d.). https://i-concrete.epfl.ch/ (accessed July 28, 2020).
[26] A. Muttoni, J. Schwartz, B. Thürlimann, Design of Concrete Structures with Stress Fields, 1997. https://doi.org/10.1007/978-3-0348-9047-2.
[27] Canadian Standards Association, Carbon steel bars for concrete reinforcement CSA G30.18-09, 2019.
[28] ASTM International, A370-19e1: Standard Test Methods and Definitions for Mechanical Testing of Steel Products, Am. Soc. Test. Mater. (2019). https://doi.org/10.1520/A0370-19E01.
[29] ASTM International, C39/C39M-18: Standard Test Method for Compressive Strength of Cylindrical Concrete Specimens, Am. Soc. Test. Mater. (2018). https://doi.org/10.1520/C0039_C0039M-18.
[30] GOM, GOM Correlate | GOM, (n.d.). https://www.gom.com/3d-software/gom-correlate.html (accessed June 30, 2020).
[31] Zohreh Heydariha J, Das S, Banting B. Effect of grout strength and block size on the performance of masonry beam. Constr. Build. Mater. 2017;157:685–93. https://doi.org/10.1016/j.conbuildmat.2017.09.130.
[32] Corr D, Accardi M, Graham-Brady L, Shah S. Digital image correlation analysis of interfacial debonding properties and fracture behavior in concrete. Eng. Fract. Mech. 2007;74:109–21. https://doi.org/10.1016/j.engfracmech.2006.01.035.

4. Research Paper III

This chapter follows the format of a journal paper entitled "*Experimental and numerical investigation of large-scale reinforced concrete deep beams designed with the Generative Tie Method*". This paper has been submitted to a reputable Journal for publication and is currently being reviewed.

Journal

Experimental and numerical investigation of large-scale reinforced concrete deep beams designed with the Generative Tie Method

Marcos V.G. Silveira[1a], Luís A.G. Bitencourt Jr.[2a*], Sreekanta Das[3b]

a Dept. of Structural and Geotechnical Engineering, University of São Paulo, São Paulo, SP, Brazil 05508-010.
b Dept. of Civil and Environmental Engineering, University of Windsor, Windsor, ON, Canada N9B 3P4.

ARTICLE INFO

Keywords:
Generative Tie Method (GTM)
Deep beams
Strut-and-Tie Method (STM)
Finite Element Analysis (FEA)
bond-slip

ABSTRACT

This study presents a comprehensive evaluation of the behavior of two large-scale reinforced concrete deep beams designed using the Generative Tie Method (GTM). Different admissible values of the loss of compressive strength in the concrete (η_{adm}) were considered, and the results were compared to a deep beam designed with the help of the Strut-and-Tie Method (STM). The study highlights the importance of selecting an appropriate η_{adm} value for designing reinforced concrete deep beams capable of exhibiting ductile behavior using the GTM. The results show that specimen SIIIa, designed using the GTM with a η_{adm} of 0.5, demonstrated a highly optimized reinforcement layout with the most pronounced reinforcement yielding, indicating ductile behavior. Among the studied specimens, the one designed using GTM with an η_{adm} of 0.7 exhibited the lowest maximum crack width and the highest ultimate load, despite demonstrating brittle failure. Both GTM-designed specimens demonstrated higher performance ratios compared to the deep beam designed using STM. By integrating the bond-slip model proposed in the fib Model Code 2010 into the finite element analysis framework, the numerical simulations produced highly accurate predictions of the behavior of the deep beams. The authors suggest further investigations to enhance the proposed numerical strategy and apply the GTM for designing reinforced concrete deep beams with organic or optimized shapes.

1. Introduction

Structural concrete discontinuous members also referred to as D-regions, require meticulous attention when designing the reinforcement layout. D-regions include pile caps, beam-column joints, frame corners, corbels, deep beams, holes, and support regions. The strut-and-tie method (STM) is the primary design method utilized for such structural members, which gained considerable attention following the publication by Schlaich et al. in 1986 [1]. Important structural concrete design codes, including the Canadian standard [2], ACI building code [3], and fib model code [4], provide provisions and guidelines to design D-regions using the STM. Although the STM is extensively used [5–14], its application presents a significant challenge in the development of idealized trusses. Therefore, various researchers are exploring and devising frameworks utilizing topology optimization to address this matter. Stoiber and Kromoser [15] provide a comprehensive review of numerical and experimental investigations into topology optimization in structural concrete.

Although the STM method is widely used for designing structural concrete D-regions, the Stress Fields method (SFM) has also been identified as a valuable tool for designing such elements, according to Ruiz and Muttoni [16]. Notwithstanding their similarities in principles, the main differentiation between these methods lies in the studied variables. While the STM is based on the truss analogy and examines the discrete forces acting in a truss, the SFM is based on the stress acting in usually 2D components. As a result, the SFM is more suitable for finite element analysis (FEA) implementation [17]. Ruiz and Muttoni [16] proposed an FEA framework based on Elasti-Plastic Stress Fields, which has been demonstrated to be an excellent analysis and design tool for discontinuous structural members [17–19].

In addition to the development of STM models, optimization frameworks have emerged as a promising approach in the design of reinforced concrete structures. For example, Zhang et al. [20] have recently proposed an innovative strategy that employs Topology Optimization to assist in the design of reinforcement layouts for deep beams. Their study highlights the advantages of using this approach, which resulted in an optimized reinforcement layout that exhibited superior performance in controlling damage accumulation.

The innovative strategies for structural components design and optimization mentioned above align with the use of innovative techniques employed in the fabrication of structural members. The application of 3D concrete printing in construction has been extensively researched, as evidenced by various research papers [21–24]. Additionally, 3D printing of steel-based materials is gaining popularity within the industry, particularly in the structural aspect, as demonstrated in the literature [25–29]. Furthermore, 3D printing has been explored as a viable option for producing formwork in the construction industry, as discussed in [30–32]. These applications can enhance the efficiency of structural component construction by facilitating the use of optimized shapes and reinforcement layouts.

In this study, a performance-based design method called the Generative Tie Method (GTM) [17] is employed in the design of the classical deep beam originally proposed by Schlaich et al. [1]. To this end,

[1] Ph.D. Candidate.
[2] Assistant Professor.
[3] Professor.
* Corresponding author: luis.bitencourt@usp.br

Nomenclature

Abbreviations and Symbols	Description		
ACI	American concrete institute	$f'_{c\,exp}$	Experimental concrete compressive strength
DAQ	Data acquisition system	f_y	Specified reinforcement yield strength
DIC	Digital image correlation	P_{crack}	Applied load while the first measurable crack (0.1 mm of width) appears
D-regions	Discontinuous regions	P_u	Experimental ultimate applied load
EPSF	Elastic-plastic stress fields	P_u/W_{Reinf}	Ratio/relationship between the ultimate load and the total weight of the reinforcement cage
FEA	Finite element analysis	P_y	Applied load while reinforcement reaches the yielding
GTM	Generative tie method	S_1	Slip I (*fib*)
LVDT	Linear variable differential transformers	S_2	Slip II (*fib*)
MCFT	Modified compression-field theory	S_3	Slip III (*fib*)
MDR	Minimum distributed reinforcement	W_{Reinf}	Weight of reinforcement cage
SC	Structural concrete	δ_u/δ_y	Ductility ratio
SFM	Stress fields method	η_{adm}	Admissible/allowable level of tensile strain in concrete within GTM
STM	Strut-and-tie method	τ_f	Shear friction capacity (*fib*)
f'_c	Specified concrete compressive strength	τ_{max}	Maximum value of bond stress (*fib*)

the research employs numerical simulations and large-scale tests to evaluate the effectiveness of the design approach. A comparative analysis is performed between the numerical prediction results and the experimental outcomes. Moreover, the study presents a comparative study between the GTM-designed specimens and the STM-designed specimen, previously studied by Silveira et al. [19]. Furthermore, the study concludes by outlining the advantages of using the GTM in the design of this type of structural component. Additionally, a comprehensive list of potential avenues for future investigations that may further enhance the efficacy of the design methodology employed in this research is also disclosed.

2. Design of the specimens

The study conducted by Silveira et al. [19] presents experimental and numerical investigations on the design of a classical deep beam with a large opening using the Strut-and-Tie Method (STM). A performance-based optimization framework called strut-and-tie performance-based optimization was developed, and a comparative analysis showed that the proposed method for the design of deep beams is promising. Additionally, this study includes the outcomes of a large-scale experimental program conducted on the specimen designed with the ACI-318 [3] Strut-and-Tie Method design provisions.

Silveira et al. [17] introduced the Generative Tie Method (GTM), a nonlinear procedure that employs finite element analysis (FEA) to iteratively design the reinforcement layout of a structural concrete (SC) member. This method is based on a five-step process, beginning with the creation of a first trial numerical model using the minimum distributed reinforcement (MDR). The numerical strategy used in this framework is the one proposed by Ruiz & Muttoni [16]. Overall, the GTM enhances the efficiency of the design process, reducing the time and effort required for manual design and increasing the accuracy and reliability of the reinforcement layout.

In this study, two large-scale specimens based on the "*deep beam with a large hole*" proposed by Schlaich et al. [1] and previously investigated by Silveira et al. [19] are analyzed. The geometric configuration, boundary conditions, and load scheme of the specimens are presented in Figure 1a. The specified concrete compressive strength (f'_c) and maximum diameter of coarse aggregate used were 40 MPa and 12.7 mm (1/2 in), respectively. The reinforcement layout design of the two specimens was carried out using the Generative Tie Method (GTM) [17]. This nonlinear process uses Finite Element Analysis (FEA) iteratively to optimize the reinforcement layout of structural concrete members. The first trial model used in the GTM framework was designed based on the minimum distributed reinforcement (MDR) recommended by ACI 318-19 [3]. The MDR was implemented using 10M 400W steel reinforcement bars [2,33], with nominal yield strength (f_y) of 400 MPa and actual cross-sectional area of 100 mm². Figure 1b and Figure 1c show the MDR layout adopted as input for the GTM framework, with the two layers of 10M reinforcement bars [33] placed close to each face of the specimens.

As part of this investigation, the reinforcement design of the specimens SIIIa and SIIIb was carried out using the Generative Tie Method (GTM) algorithm presented in Figure 2, adapted from Silveira et al. [17]. The GTM follows a systematic five-step process to ensure that the structural component meets the design requirements. The first step incorporates the creation of an initial numerical model that incorporates the minimum distributed reinforcement (MDR). In the second step, a nonlinear numerical analysis of the model is conducted using the finite element analysis (FEA) approach, which is based on the methodology developed by Ruiz & Muttoni [16]. The design requirements recommended by the relevant structural codes and standards are verified in the third step. Based on the results of the previous step, the fourth step consists of making design decisions, which may include increasing the diameter or amount of existing reinforcement bars, as well as introducing additional reinforcement bars if required. The load is then gradually increased, leading back to the second step for further FEA analysis. The final step is initiated upon fulfillment of all design requirements, which entails reaching the predetermined design load and subsequently verifying if the current model complies with the prescribed design specifications. The chosen values of η_{adm} were 0.5 and 0.7 for SIIIa and SIIIb, respectively. The GTM framework has been enabled to increase the cross-sectional area of existing rebars from the initial trial model shown in Figure 1b. While the studied specimens can easily accommodate new rebars in the height and length directions, as shown in Figure 1a, the width direction has limited space to accommodate increases in existing rebar amount or diameters, as illustrated in Figure 1c. Therefore, in the design of the studied specimens, the GTM framework was programmed to prioritize the creation of new rebar positions over the increase in existing ones.

In contrast to prior investigations undertaken by the present authors, the functionality to generate diagonal reinforcements in addition to horizontal and vertical ones was implemented in the current study. However, to avoid impractical reinforcement configurations, this functionality was restricted to creating solely 45-degree-oriented diagonal reinforcements in addition to the vertical and horizontal bars.

Additionally, the minimum new reinforcement length was set to 500 mm (20 in) to prevent reinforcement anchorage issues. Diagonal-oriented new reinforcement bars were set to have horizontal and vertical components of at least 300 mm (12 in) in length. The design load of 720 kN for both studied specimens was divided into 72 increments of 10 kN. The history of the design decisions made by the GTM algorithm during the design process is summarized in Table 1. Video 1 shows all the reinforcement changes generated by the GTM algorithm in the design of the two specimens.

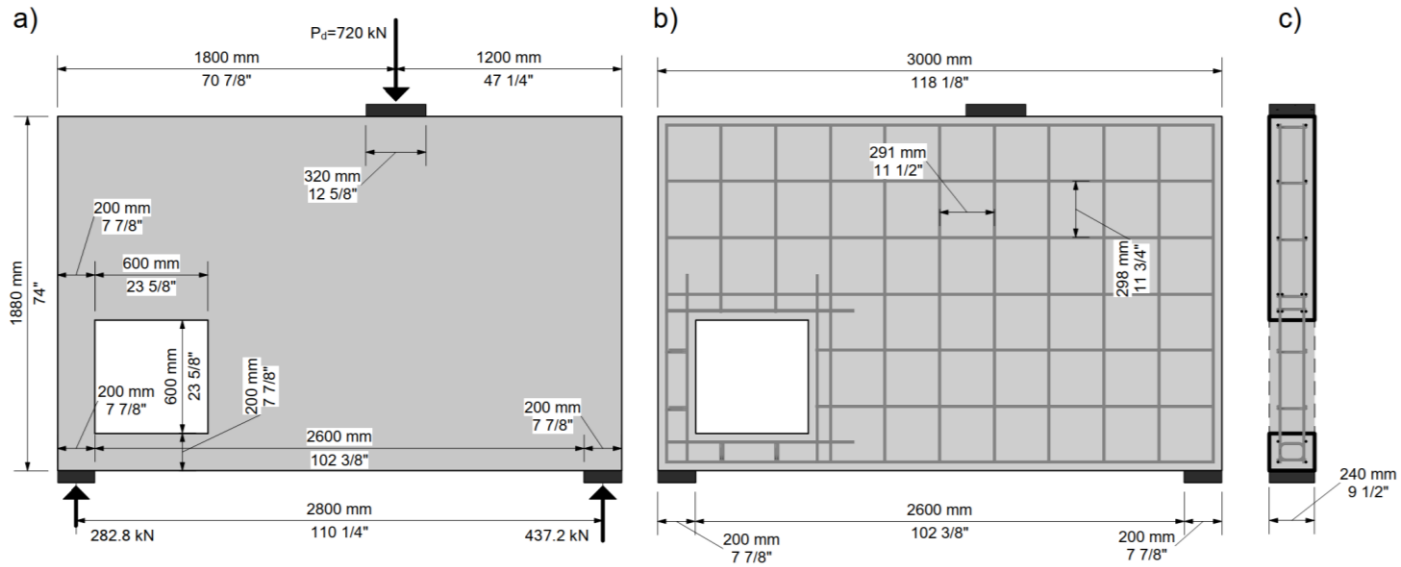

Figure 1 – Deep beam with a large hole a) elevation: overall dimensions, boundary conditions, and load scheme b) elevation: minimum distributed reinforcement layout c) cross-section: minimum distributed reinforcement layout.

Table 1 - History of design decisions made by GTM in the design SIIIa and SIIIb.

Step	η	Reinf. Yielding?	Function	Design decisions
			SIIIa	
0-37	>0.50	no	Increase load	-
38	0.49	no	Create reinforcement	Inclined reinforcement bars created in the upper right corner of the opening.
38	>0.50	no	Increase load	
39	0.49	no	Create reinforcement	Short bars extended to their maximum length in the upper right corner of the opening.
39-49	>0.50	no	Increase load	
50	0.49	yes	Create reinforcement	All short bars extended to their maximum length
50-52	>0.50	no	Increase load	
53	0.54	yes	Create reinforcement	Inclined reinforcement bars created in the upper right corner of the opening.
53-69	>0.50	no	Increase load	
70	0.54	yes	Create reinforcement	Longitudinal reinforcement bars created below the opening at the main tie.
70-71	>0.50	no	Increase load	
72	>0.50	no	Outcome	
			SIIIb	
0-19	>0.70	no	Increase load	
20	0.69	no	Create reinforcement	Inclined reinforcement bars created in the upper right corner of the opening.
20-29	>0.70	no	Increase load	
30	0.69	no	Create reinforcement	All short bars extended to their maximum length.
30-31	>0.70	no	Increase load	
32	0.69	no	Create reinforcement	Inclined reinforcement bars created in the upper right corner of the opening.
32-49	>0.70	no	Increase load	
50	0.69	no	Create reinforcement	Diagonal, horizontal, and vertical reinforcement bars created in the upper right corner of the opening.
50-59	>0.70	no	Increase load	
60	0.69	no	Create reinforcement	Diagonal, horizontal, and vertical reinforcements created in the upper right corner of the opening.
60-64	>0.70	no	Increase load	
65	0.69	no	Create reinforcement	Stirrup created below the opening.
65-69	>0.70	no	Increase load	
70	0.69	no	Create reinforcement	Diagonal, horizontal, and vertical reinforcements created in the upper right corner of the opening.
70-71	>0.70	no	Increase load	
72	>0.50	no	Outcome	

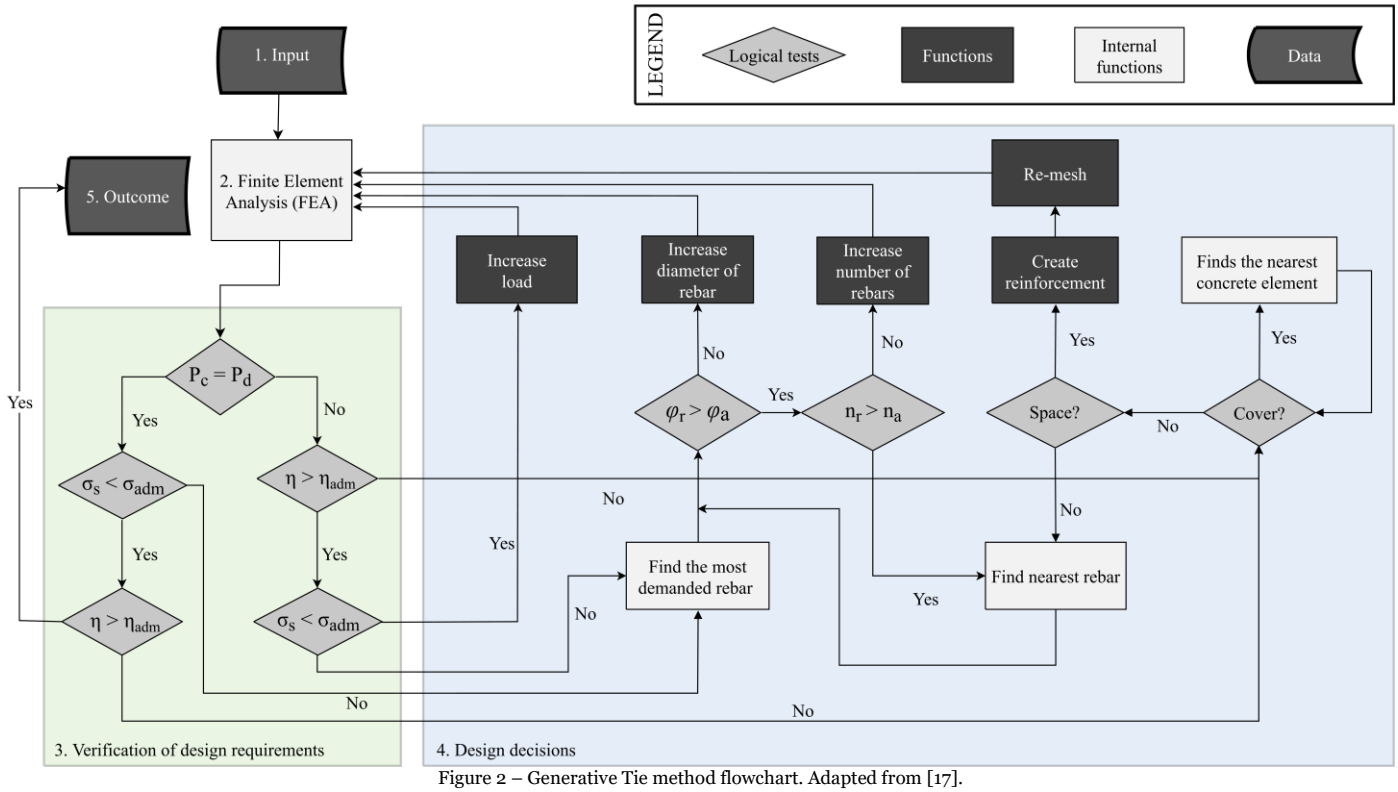

Figure 2 – Generative Tie method flowchart. Adapted from [17].

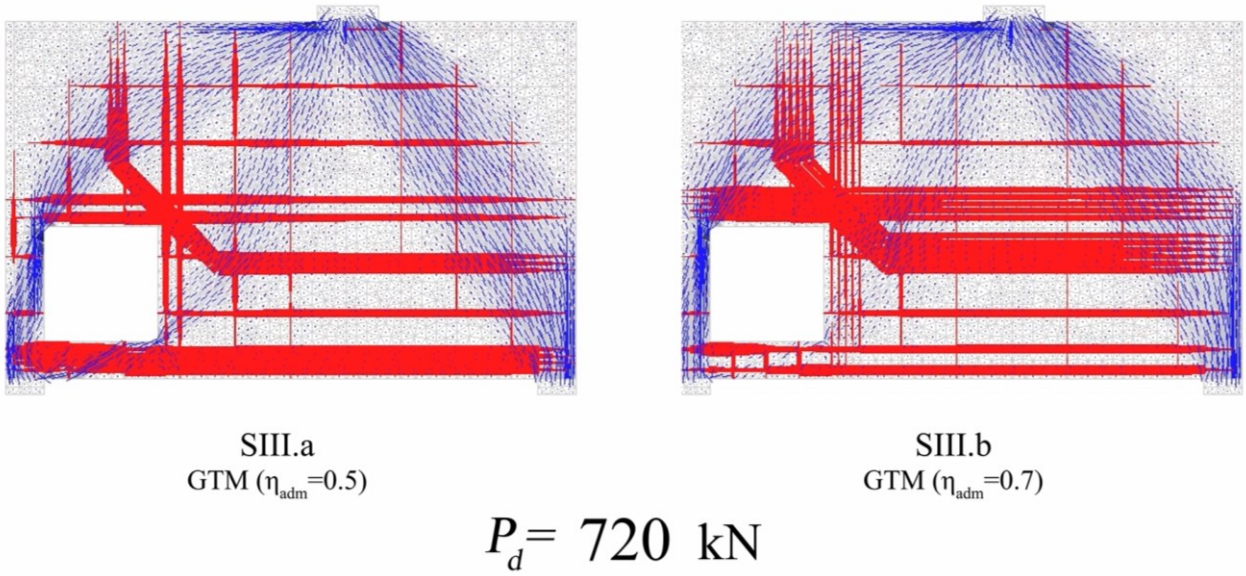

Video 1 – Animation of design decisions made by GTM in the design of SIIIa and SIIIb.

In accordance with the findings of Silveira et al. [17], selecting a higher value for η_{adm} results in a lower allowable level of tensile strain in concrete. Thus, the design process of specimen SIIIb was more complex than that of SIIIa, as detailed in Table 1. As indicated in the same table, no yielding of reinforcement occurred during the design of SIIIb (column 3), indicating that the design was governed by the allowable level of tensile strain in concrete (η_{adm}). Since the value of η_{adm} assigned to SIIIb (0.7) was greater than that assigned to SIIIa (0.50), the reinforcement cage designed for SIIIb is heavier than the one designed for SIIIa. The reinforcement layouts for both specimens are depicted in Figure 3, where the reinforcement bars displayed represent two layers of 10M bar [33]. As illustrated in Figure 3, more reinforcement bars were needed in specimen SIIIb around the right-top corner of the opening. The total weights of the designed reinforcement cages were 117.1 kg and 144.5 kg for SIIIa and SIIIb, respectively. Therefore, the reinforcement weight of SIIIb is 23.4% greater than that of SIIIa.

3. Numerical Simulation

A 2D finite element analysis (FEA) approach was utilized to predict the performance of the reinforced concrete deep beams investigated in this research. This numerical technique provided an effective means of analyzing the behavior of the beams under different loading conditions, allowing for a detailed assessment of their structural response. Throughout the implementation of this approach, various aspects of the behavior of the deep beams were successfully predicted: the deflection, stress fields, and failure mechanisms. Following previous research [19], the discretization of the concrete was achieved using constant strain triangle elements (see Figure 4a). The concrete was modeled using a constitutive damage model integrated using an implicit-explicit scheme, as proposed by Bitencourt et al. [34]. The FEA strategy applied in this research incorporates the approach proposed by Cervera et al. [35], utilizing two independent scalar damage variables for tension and compression (refer to Figure 4d). The reinforcement bars were modeled

using truss finite elements with an elastic-plastic constitutive model, as shown in Figures 4b and 4e.

As proposed by Bitencourt et al. [36], the coupling finite elements describe the bond-slip phenomenon that occurs between the reinforcement bars and concrete in reinforced concrete members. Figure 4c depicts the schematic of the coupling finite element used to model the debonding mechanism. Moreover, the constitutive model adopted in this research was inspired by the one proposed in the *fib* Model Code 2010 [4], as shown in Figure 4f. To carry out the numerical simulations, the parameters were chosen as follows: $\tau_{max} = 16.4\,MPa$, $\tau_f = 6.6\,MPa$, S_1=1 mm, S_2=2 mm, S_3=25 mm, and $\alpha = 0.4$. The incorporation of a bond-slip model can be highlighted as the main incorporation of the numerical strategy proposed by the same authors in Silveira et al. [19]. Hence, improvements in the prediction of crack patterns and strain in the reinforcement bars are expected.

Finally, the numerical simulations utilized the Modified Compression-field Theory (MCFT) equation [37], which describes the loss of concrete compressive strength due to transversal tensile strain in conjunction with the FE technique presented in previous research papers [19,34,36]. The properties of materials used in the numerical simulations were obtained from the experimental program, as detailed in section 4.

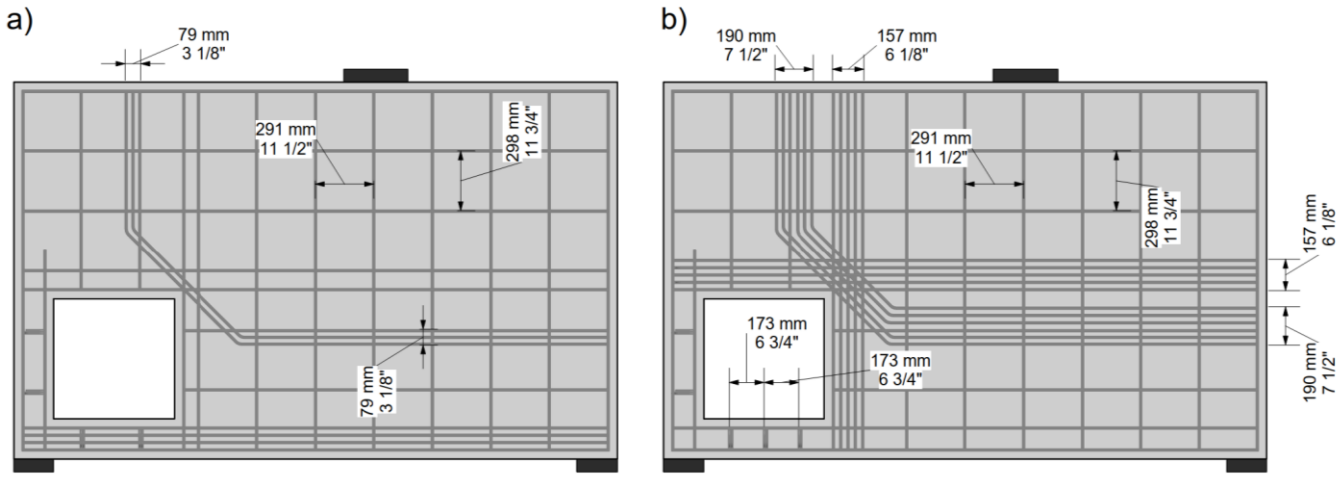

Figure 3 – Reinforcement layout detailing of a) SIIIa b) SIIIb.

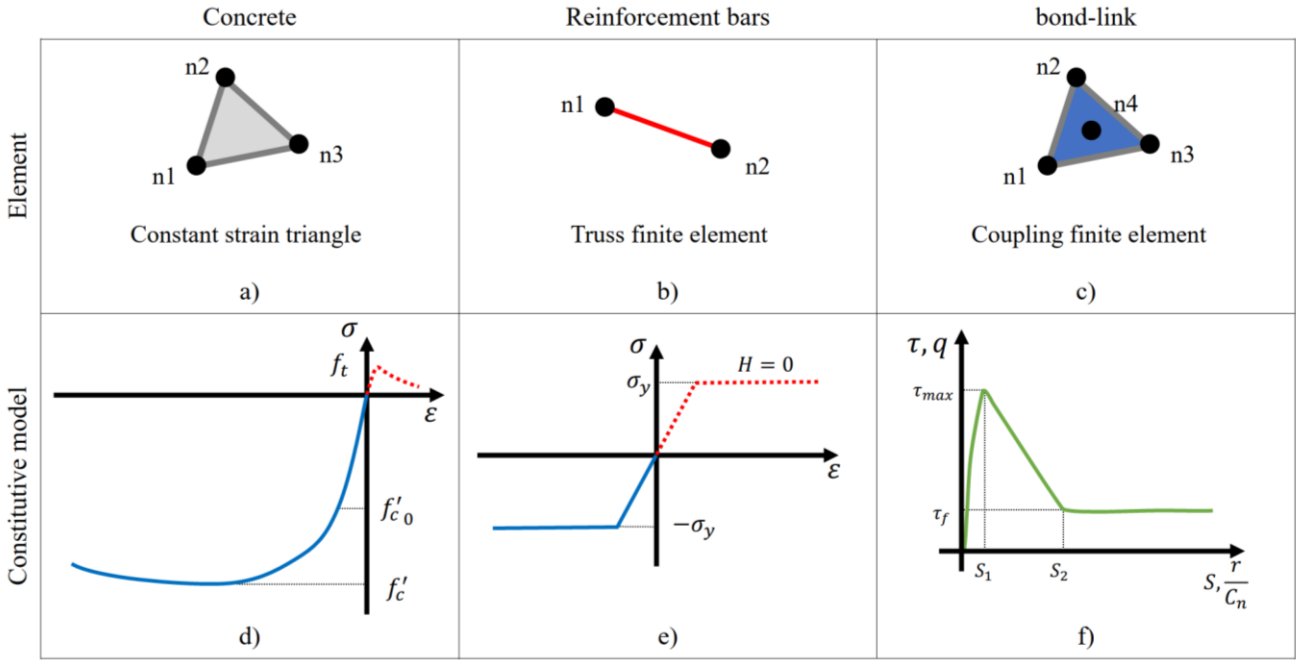

Figure 4 – Numerical strategy a) concrete finite element; b) reinforcement bars finite; c) Coupling finite element; d) concrete constitutive model; e) reinforcement bars constitutive model; f) coupling constitutive model. (adapted from Silveira et al. [19]).

4. Experimental Program

The experimental program was conducted in the Structural Engineering Laboratory at the University of Windsor in Canada, including fabrication, preparation, and testing of the specimens. Reinforcement bars 10M made out of 400W steel were used in all reinforced concrete elements [33]. The batch of reinforcement bars used in this research was tested according to [38]. The results exhibited yielding stress of 495.1 MPa, ultimate stress of 730.5 MPa, and modulus of elasticity of 269.2 GPa. According to the procedures established in [39], the experimental concrete compressive strength ($f'_{c\,exp}$) determined through the cylinder test was 43.2 MPa.

4.1 Specimen fabrication and preparation

Specimens SIIIa and SIIIb were both built on full-scale to be experimentally tested under the loading scheme shown in Figure 1a. Figures 5a and 5b show the specimens right before and after the concrete casting, respectively. Both Figures 5a and 5b present SIIIa at the bottom, and SIIIb at the top part of the photographs. Ten strain gauges were properly attached to the reinforcement cage in five different positions in each specimen, as shown in Figure 6. To enhance the digital image correlation (DIC) analysis, speckle paints were applied to the front face of each specimen and also to the front face of the steel supports, as shown in Figure 7.

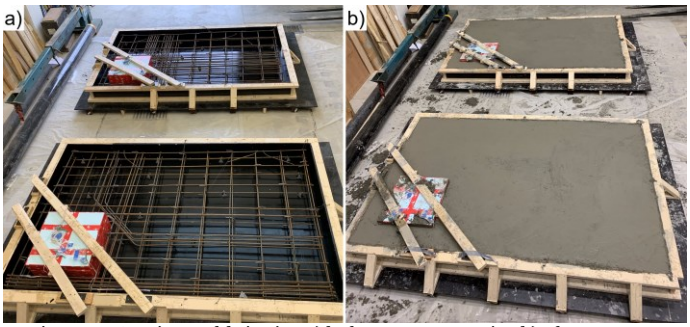

Figure 5 – Specimens fabrication a) before concrete casting b) after concrete casting.

4.2 Test setup

The loading scheme shown in Figure 1a was achieved using a high-load capacity reaction structure composed of a 1.3 m thick strong concrete floor, two 1.3 m thick strong walls in L-shape, and a steel assembly of two I-beams, as shown in Figure 6. The support assemblies are composed of steel stands and thick steel plates, they are also shown in Figure 6a. A load actuator of ±2000 kN capacity was attached to the I-beams assembly. The instrumentation used during the tests was categorized into physical instrumentation and contactless instrumentation. The physical instrumentation includes a load cell at the load actuator, four Linear Variable Differential Transformers (LVDT), and ten steel strain gauges. As shown in Figure 6a, two LVDTs (displacement gauges) were placed underneath the specimen in order to read the displacement of the bottom surface of each deep beam. The third LVDT was placed on the rear side of the specimen in order to capture a possible out-of-plane displacement during the test (see Figure 6b). The fourth LVDT was attached to the load actuator measuring its stroke along the load application.

The contactless instrumentation used in this research was based on the DIC technique. Four digital cameras mounted in the front of each specimen, taking pictures every 6 seconds, were used to collect the DIC data. The left camera and right camera in Figures 6 and 7 were mounted in portrait orientation. Each camera covered half of the specimens. Two additional cameras, shown as Support A Camera and Support B Camera in Figures 6 and 7, were assembled close to each support. Those cameras were meant to read closely the displacements in the support regions. The acquired photographs were subsequently subjected to post-processing using *GOM correlate* [40]. Those readings are later used to investigate the boundary conditions of the specimens during the tests. All the instrumentation (physical and contactless) data was collected by a proprietary data acquisition system (DAQ). Supplementary to all the instruments mentioned, a portable camera with a large field of view (GoPro) was set in front of the test setup covering the whole scene. Two professional studio lights with color and intensity control were used to enhance the DIC results (see Figure 7).

5. Results and Discussions

This section presents and discusses the results obtained from both experimental and numerical investigations conducted in this study. The experimental results include load-displacement curves, crack pattern and propagation, crack width, reinforcement bar strain, and failure mode. Additionally, the numerical investigation results are compared with those obtained through the experimental program. Furthermore, the section also includes comparisons between the results of this study and those of other research studies.

Table 2 provides experimental test results, with SIa results obtained from Silveira et al. 2022 [19] for comparison purposes. The table lists the reinforcement steel weight in kilograms (kg) employed by each member. Table 2 also shows the crack load (P_{crack}) of each reinforced concrete specimen, which corresponds to the applied load that resulted in the first visible crack with a width of 0.1 mm. Those loads were obtained with the help of the DIC data. The yielding load (P_y) and its position are also exhibited in the table (refer to Figure 6a). The ultimate load (P_u) represents the applied load that caused the failure of the specimens. Finally, two performance ratios are also depicted in Table 2. To measure the effectiveness of the reinforcement bars used in the specimens, this study employed the P_u/W_{Reinf} ratio proposed by Herranz et al. 2012 [41]. This ratio establishes the relationship between the ultimate load (P_u) and the total weight of reinforcement utilized in the construction of the specimen (W_{Reinf}). Moreover, in order to assess the ductility of the specimen failure, this research utilized the δ_u/δ_y ratio, which represents the relationship between the deflection observed under the ultimate load and the deflection measured under the yielding load.

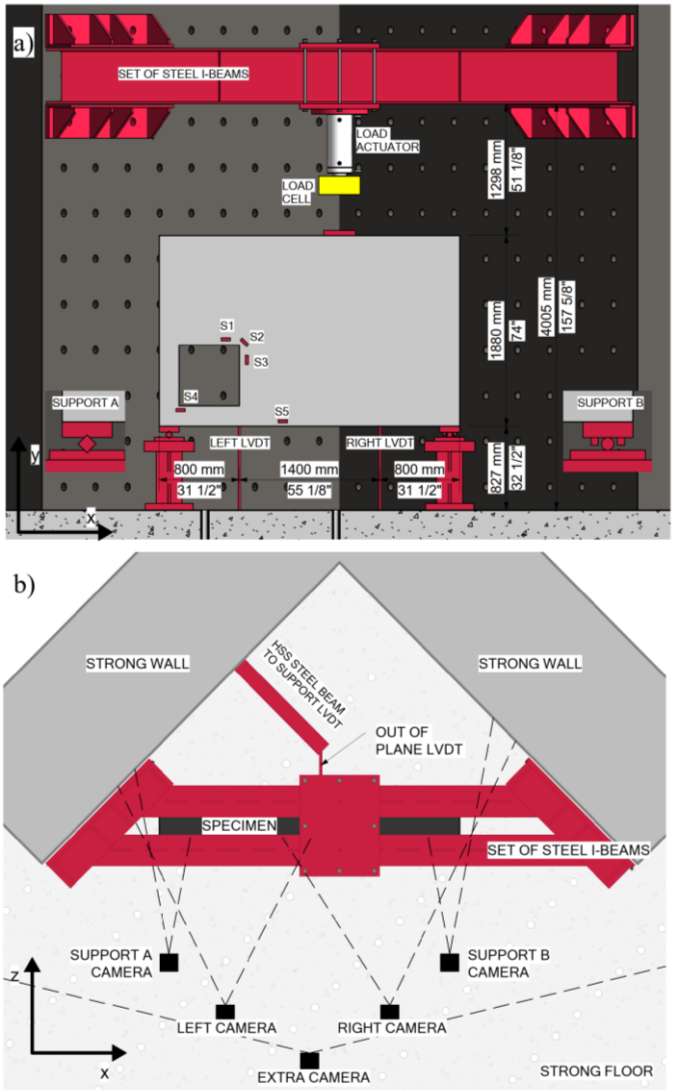

Figure 6 – Test setup scheme a) front elevation; b) plan view.

The experimental results in Table 2 demonstrate that specimen SIIIa exhibited the best performance with a P_u/W_{Reinf} ratio of 14.3 and a δ_u/δ_y ratio of 11.0, outperforming the other two specimens. In contrast, SIIIb demonstrated better performance than the specimen designed using the STM, SIa. Both SIa and SIIIb failed in the right support region due to concrete crushing, while SIIIa experienced a shear failure below the opening (see Figure 11). Moreover, the first yielding of reinforcement occurred at the same position (S4) for both SIa and SIIIb, however, they also exhibited brittle failures overall. In contrast, SIIIa demonstrated the first yielding at the S2 position and exhibited a ductile failure. These findings indicate that SIIIa had the most favorable performance in terms of ductility and material consumption.

The results presented by Zhang et al. [20] highlight the outstanding performance of a deep beam with ductile failure, which was the case of SIIIa. In addition, Zhang et al. [20] investigated the use of topology optimization to aid in the design of deep beams. The research found that optimizing the reinforcement layout resulted in a 13.8% reduction in steel reinforcement consumption compared to an unoptimized specimen while maintaining the bearing load and the quasi-brittle failure.

Figure 8 shows the principal major strain distribution of specimens SIIIa and SIIIb under the load of 720 kN, as obtained through the DIC

method. The principal major strain plot can serve as a reliable indicator of the crack pattern and propagation ([17,19,42–45]). The principal major strain plot generated through DIC can provide valuable information on the distribution and magnitude of strains in reinforced concrete members, which in turn can be used to detect and monitor crack formation. The figure reveals that both specimens underwent the same degree of cracking when subjected to the applied load of 720 kN. This observation is supported by the evolution of crack width, as shown in Figure 10. Crack 1 should be highlighted by being the most prominent in terms of length and width.

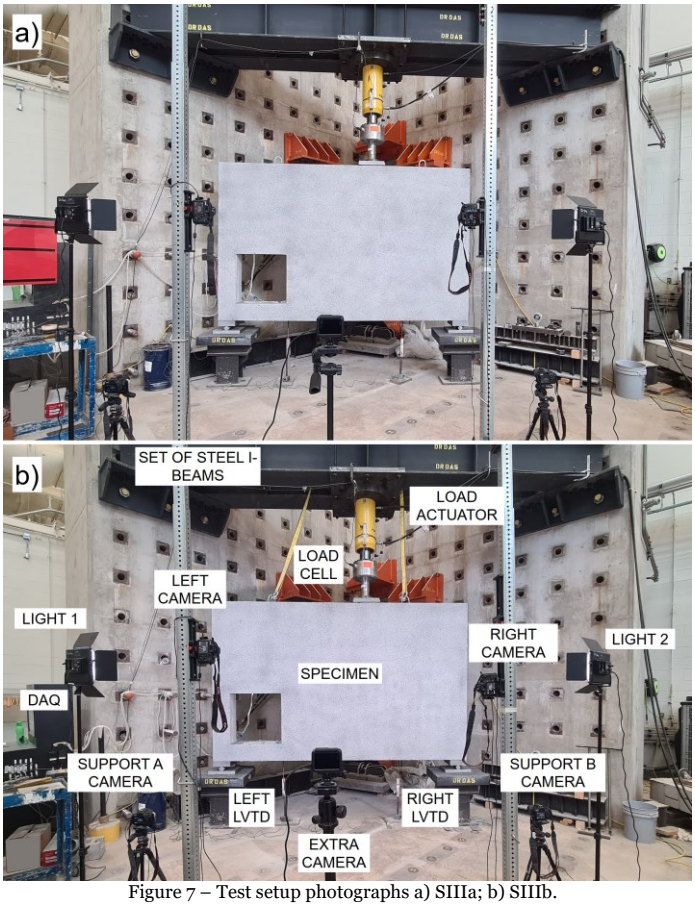

Figure 7 – Test setup photographs a) SIIIa; b) SIIIb.

The principal major strain distribution obtained through the DIC technique for specimens SIIIa and SIIIb at their ultimate load is presented in Figure 9. The figure reveals some key differences in the crack patterns of the two specimens. Specifically, SIIIa exhibited wider cracks than SIIIb, consistent with the crack width evolution exhibited in Figure 10. Nevertheless, specimen SIIIb showed a greater number of cracks overall. The most significant difference in the crack patterns of specimens SIIIa and SIIIb was in their distribution. Specimen SIIIb exhibited more cracks on both the right and left sides of the specimen, while specimen SIIIa had two prominent cracks that were not present in SIIIb. The first was a diagonal crack that extended from the lower right corner of the opening to the right side of the left support corner. Specimen SIIIa failed in shear at this location, as evidenced in Figure 11. The second one was a horizontal crack close to the upper left corner of the opening that was also visible through the width of the specimen.

Table 2 – Experimental test results. SIa results were extracted from Silveira et al. 2022 [19].

Sp.	Reinf. Weight	Crack load P_{crack}	Yeilding load P_y & Position		Ultimate load P_u	$\frac{P_u}{W_{reinf}}$	$\frac{\delta_u}{\delta_y}$
	(kg)	(kN)	(kN)		(kN)	(kN/kg)	
SIa	134	426	1312	S4	1832	13.6	1.7
SIIIa	117	523	839	S2	1678	14.3	11
SIIIb	145	506	1088	S4	1984	13.7	3.7

The evolution of crack widths in specimens SIIIa and SIIIb is presented in Figure 10. The DIC technique used to measure crack widths is consistent with the approach adopted by previous research studies, such as [17,46,47]. The technique has a minimum resolution of 0.1 mm, and any crack width below this threshold is considered to have a width of 0 mm. As observed in Figure 10, Crack 1 in specimen SIIIa was the first crack to become visible and exhibited the widest opening among the six analyzed cracks. Crack 1 reached a width of 3.6 mm when specimen SIIIa was under the ultimate load. Similarly, Crack 1 was the first to appear in specimen SIIIb, although Crack 3 registered the largest opening among the three analyzed cracks within specimen SIIIb. Crack 3 achieved a width of 1.6 mm when specimen SIIIb was under its ultimate load.

The applied load versus displacement curves obtained from experimental tests and numerical simulations for both specimens SIIIa and SIIIb are presented in Figure 12. The displacements were measured from the projection of the right edge of the opening to the bottom surface of the specimen, where the left LVDT was placed (refer to Figure 6). The results indicate that SIIIa exhibited a yielding plateau, whereas specimen SIIIb did not. The numerical simulations accurately captured this contrast. Moreover, the experimental and numerical results exhibited good agreement, as both specimens' stiffness and ultimate load were well predicted.

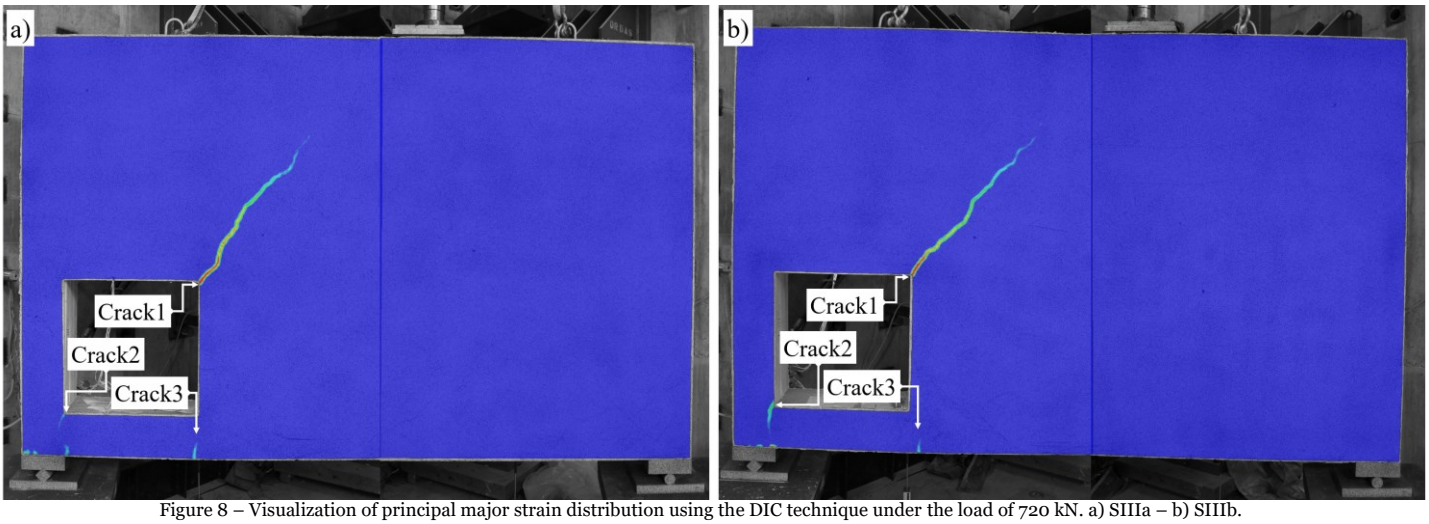

Figure 8 – Visualization of principal major strain distribution using the DIC technique under the load of 720 kN. a) SIIIa – b) SIIIb.

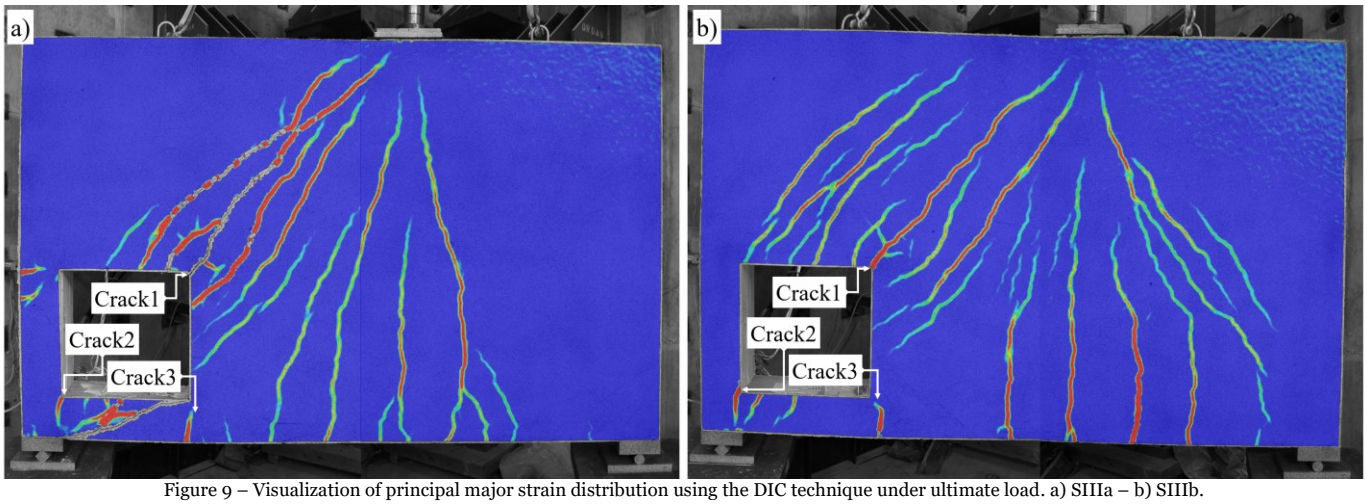

Figure 9 – Visualization of principal major strain distribution using the DIC technique under ultimate load. a) SIIIa – b) SIIIb.

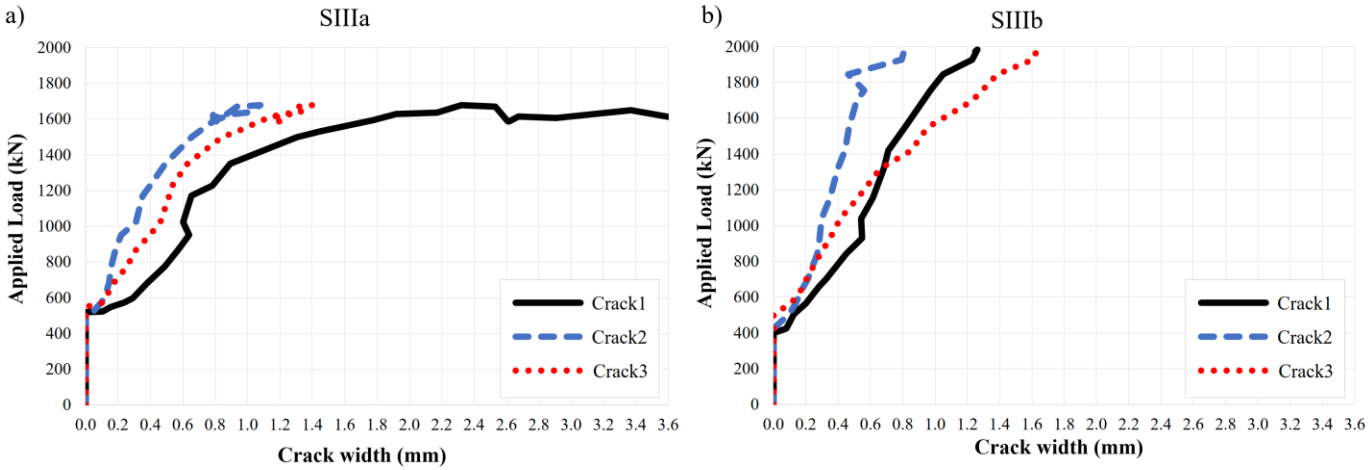

Figure 10 – Evolution of crack width captured via digital image correlation. a) SIIIa - b) SIIIb.

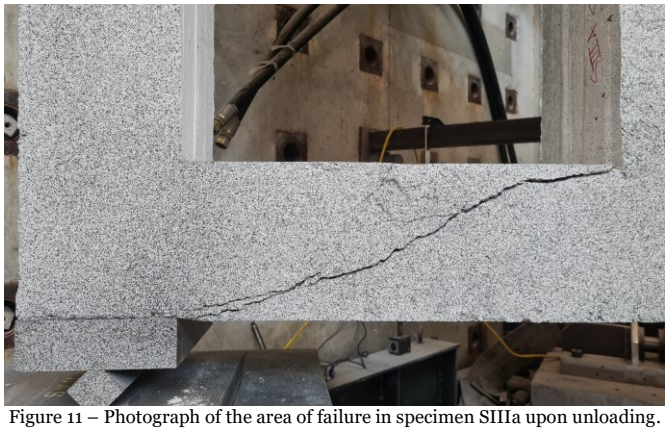

Figure 11 – Photograph of the area of failure in specimen SIIIa upon unloading.

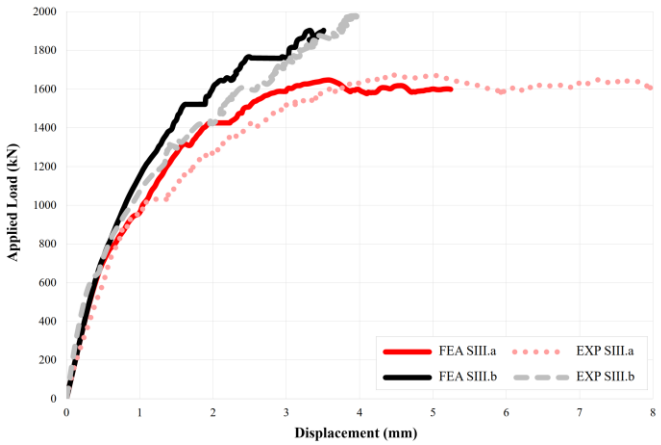

Figure 12 – Applied load *vs* displacement curves obtained from experimental tests and numerical simulations.

Table 3 exhibits the ultimate load results for the four categories: experimental results of specimens SIIIa and SIIIb and numerical simulation results of specimens SIIIa and SIIIb. The table also includes the percentage error when compared to the experimental results, indicating how well the numerical simulations were able to predict the ultimate load. The results show that the ultimate experimental load of specimen SIIIa is 1678 kN, while the ultimate experimental load of specimen SIIIb is 1984 kN. The ultimate loads predicted by the numerical simulation for specimens SIIIa and SIIIb are 1647 kN and 1903 kN, respectively. The percentage errors for the numerical simulations compared to the experimental results are 1.9% for specimen SIIIa and 4.0% for specimen SIIIb. These results suggest that the numerical simulations accurately predicted the ultimate load for both specimens with a small margin of error. However, the displacement exhibited by SIIIa under the ultimate load was not well captured by the simulations, as can be observed in Figure 12.

Figure 13 illustrates the tensile damage plots generated by applying FEA on the two investigated specimens, SIIIa and SIIIb. As shown by the scale on the right-hand side of Figure 13, the finite elements highlighted on the plot have tensile damage ranging from 0.99 to 1. Such values indicate that the corresponding tensile stresses have surpassed the concrete tensile strength, thereby the damaged elements coincided with the crack location. Therefore, the numerical strategy effectively captured the corresponding crack pattern for both specimens (refer to Figure 9). Specifically, the simulation accurately predicted that SIIIb would demonstrate a larger number of cracks with smaller widths as compared to SIIIa, as the experimental results have shown. Furthermore, the simulation also captured a more intensive cracking level below the opening for SIIIa compared to SIIIb, which was again supported by the experimental results.

Figure 14 presents the results of the stress fields for the studied deep beams obtained through FEA. The compressive stress fields are depicted in blue vectors, providing a clear visualization of stress distribution across the members. Furthermore, the stress on the reinforcement bars is displayed using varying thicknesses and colors, and its value range is presented in the legend located in the right lower corner of the figure. It is important to note that the legend exclusively pertains to the stress on the reinforcement bars.

Table 3 – Finite element analysis results compared to experimental results.

Results	Ultimate load P_u (kN)	Deviation (%)
EXP SIIIa	1678	-
EXP SIIIb	1984	-
FEA SIIIa	1647	1.9%
FEA SIIIb	1903	4.0%

The stress field simulation presented in Figure 14 offers critical insight into the impact of different η_{adm} values within the GTM framework on the structural mechanism performed by each deep beam. The results suggest that the selection of these values can significantly affect the distribution of stress across the components. Notably, the compressive stress flow on the left side of the specimen was observed to be considerably altered by the reinforcement layout. Hence, the failure modes observed in specimens SIIIa and SIIIb are very different, with shear failure occurring in specimen SIIIa at the compressed diagonal strut below the opening. While the reinforcement layout of specimen SIIIb led to a higher level of compressive stress on the left side of the opening, preventing the same type of failure observed in specimen SIIIa. However, the failure of specimen SIIIb eventually occurred due to concrete crushing at the right support region.

The results highlight the importance of carefully considering reinforcement layouts and η_{adm} values in the design of deep beams using the GTM. By following this approach, structural designers can exercise greater control over the performance of individual components in comparison to traditional design techniques such as the STM. This greater control allows for more nuanced and targeted design decisions, resulting in improved structural integrity and material consumption optimization.

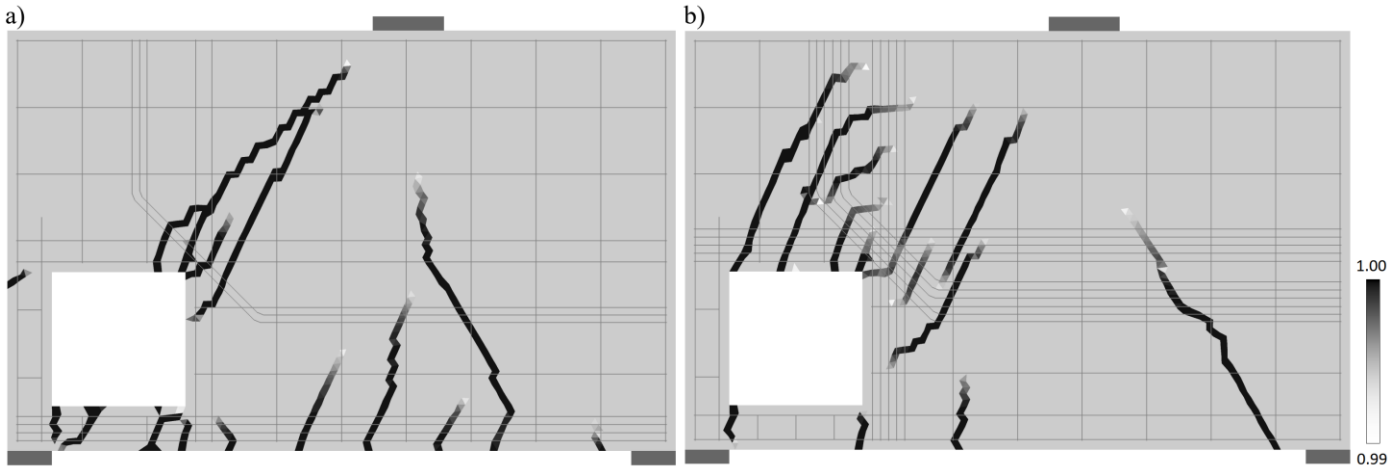

Figure 13 – Tensile damage plot using finite element analysis. a) SIIIa – b) SIIIb.

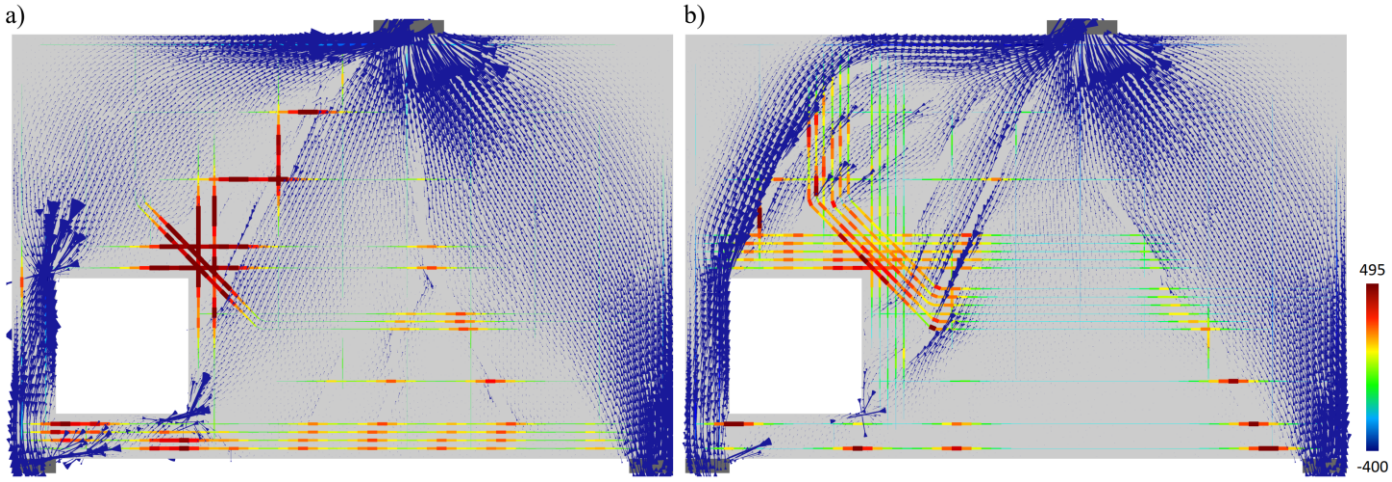

Figure 14 – Stress fields simulation through finite element analysis. a) SIIIa – b) SIIIb.

Figure 15 presents the applied load versus rebar strain curves obtained from experimental tests and numerical simulations. The figure displays results for ten different rebar positions of two specimens, SIIIa and SIIIb, as labeled in the caption. The rebar positions for strain gauges are illustrated in Figure 6a. The numerical simulations were found to have predicted the strain at strategic rebar positions of both specimens with great accuracy. In particular, the prediction of S1, S3, S4, and S5 rebar strains for specimen SIIIa and the prediction of rebar strains S2, S3, S4, and S5 for specimen SIIIb were noteworthy. However, it should be noted that some strain gauges may have failed after reaching a certain level of strain, as could be the case for strain gauges S2 and S4 for specimen SIIIa. Overall, the results suggest that the FEA approach utilized in this research was effective in predicting the rebar strain in the tested reinforced concrete deep beams. The ability to predict the rebar strain using FEA is a critical component of the design of reinforced concrete members with complex shapes, such as deep beams, ensuring that they are safe, efficient, and cost-effective.

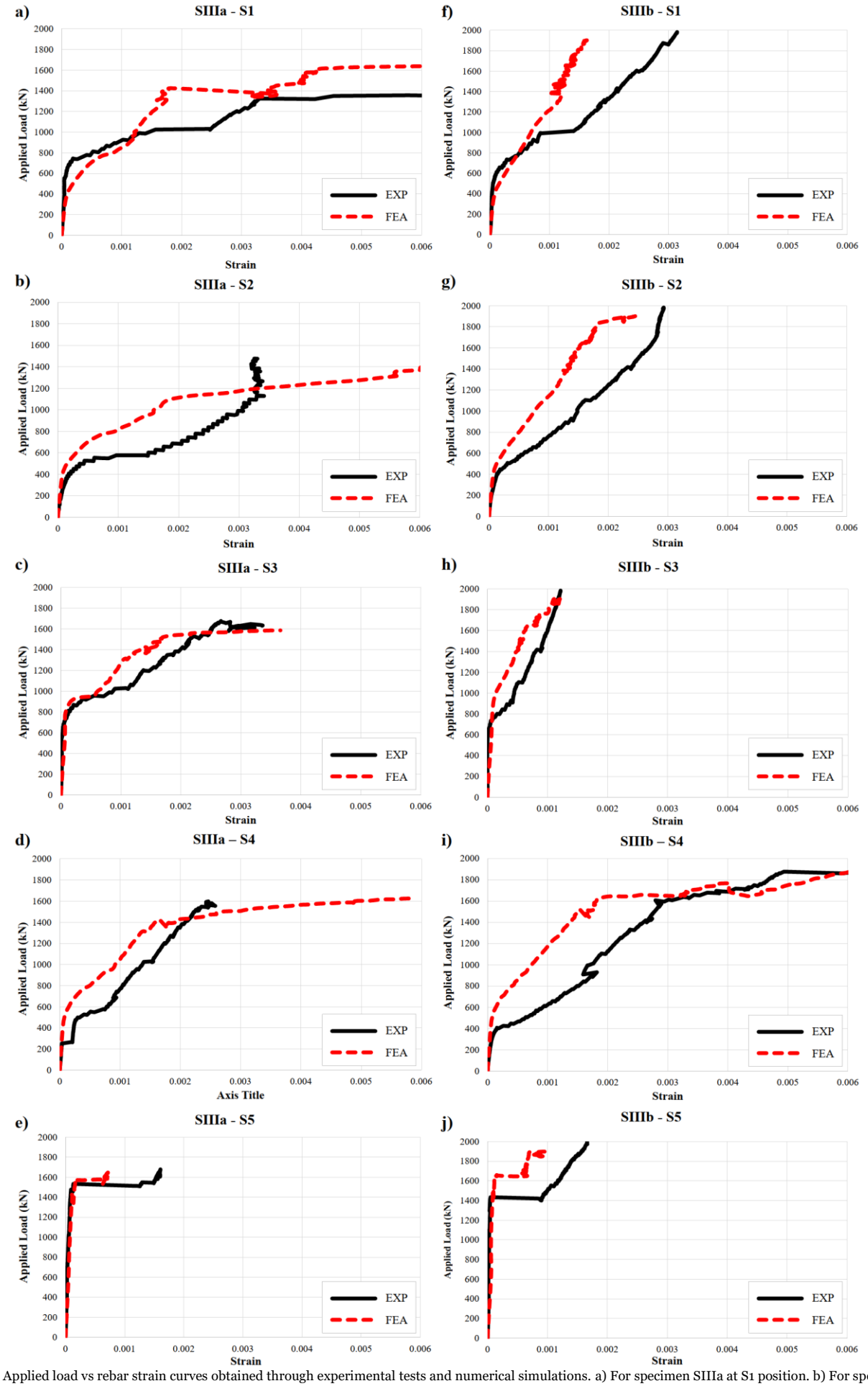

Figure 15 – Applied load vs rebar strain curves obtained through experimental tests and numerical simulations. a) For specimen SIIIa at S1 position. b) For specimen SIIIa at S2 position. c) For specimen SIIIa at S3 position. d) For specimen SIIIa at S4 position. e) For specimen SIIIa at S5 position. f) For specimen SIIIb at S1 position. g) For specimen SIIIb at S2 position. h) For specimen SIIIb at S3 position. i) For specimen SIIIb at S4 position. j) For specimen SIIIb at S5 position.

6. Conclusions

This research conducted a comprehensive evaluation to assess the behavior of two large-scale reinforced concrete deep beams designed using the Generative Tie Method (GTM). The study considered different admissible values of the loss of compressive strength in the concrete (η_{adm}) and compared the results to the same deep beam designed by the Strut-and-Tie Method (STM). The key findings of this study can be concisely summarized as follows:

1. Specimen SIIIa, which was designed using the GTM with a η_{adm} of 0.5, demonstrated a highly optimized reinforcement layout, utilizing the smallest amount of reinforcement (117 kg) while achieving the highest P_u/W_{Reinf} ratio (14.3) among the three analyzed large-scale specimens. The specimen also exhibited pronounced reinforcement yielding (Figure 15) and hence, a ductile behavior (Figure 12). This can be evidenced by the highest δ_u/δ_y ratio (11. 0) among the specimens, also performed by specimen SIIIa. These findings emphasize the importance of selecting a suitable η_{adm} value in designing reinforced concrete deep beams capable of exhibiting ductile failures using the GTM.
2. At the applied load of 839 kN, specimen SIIIa exhibited visible cracks 0.1 mm wide, which was the earliest among the three analyzed specimens. Furthermore, at the ultimate load (P_u), SIIIa demonstrated the most extensive cracking, with a maximum crack width of 3.6 mm. These results underscore the crucial importance of carefully selecting η_{adm} values in the design of reinforced concrete members using the GTM, to ensure satisfactory structural performance and adequate durability.
3. Specimen SIIIb demonstrated exceptional performance in several critical aspects. Firstly, SIIIb exhibited the lowest maximum crack width at the ultimate load (1.6 mm) among all the studied specimens. This suggests that designers may have greater control over the acceptable cracking level in structural components by choosing the appropriate η_{adm} (see Figure 10). Furthermore, SIIIb achieved the highest ultimate load and the second-highest P_u/W_{Reinf} ratio (after SIIIa), demonstrating efficient resource usage to achieve remarkable performance.
4. The highest reinforcement consumption was observed in specimen SIIIb (145 kg), which is noteworthy. Additionally, specimen SIIIb exhibited a brittle failure without showing any yielding plateau on the structural equilibrium curve (refer to Figure 12), despite some reinforcements showing yielding (refer to Figures 15 f-j). These observations suggest that, in this particular case, the low level of cracking was associated with a failure that occurred without any warning (brittle failure).
5. The numerical approach employed to predict the behavior of the deep beams demonstrated excellent agreement with the experimental results in several key aspects. The ultimate loads of the investigated specimens were successfully predicted with a small error of 1.9% for specimen SIIIa and 4.0% for specimen SIIIb (refer to Table 3). Furthermore, the numerical simulations also successfully predicted the Applied load *vs* Displacement curves with considerable accuracy, as illustrated in Figure 12.
6. Moreover, the numerical simulations accurately predicted the Applied load *vs* Rebar strain curves, refer to Figure 15. The numerical simulation also proved to be effective in predicting the location and propagation of the main cracks in the studied deep beams, as shown in Figure 9 and Figure 13. These findings demonstrate strong validation for the efficacy of the numerical strategy used in this study and support the adoption of similar techniques in the design and analysis of reinforced concrete members.
7. The stress fields presented in Figure 14 indicate that the selection of different η_{adm} values within the GTM framework can significantly influence the formation of stress fields on the structural members. The compressive stress flow on the left side of the specimen was observed to be considerably altered by the reinforcement layout. A shear failure occurred in specimen SIIIa at the compressed diagonal strut right below the opening (refer to Figure 11). On the other hand, the reinforcement layout of specimen SIIIb led to a higher level of compressive stress on the left side of the opening, preventing the same type of failure observed in SIIIa. Nonetheless, SIIIb eventually failed due to concrete crushing at the right support region.

In conclusion, the authors suggest several avenues for further investigation. First, experimental research should be conducted in deep beams with organic or optimized shapes designed with the help of the GTM. Moreover, the authors recommend enhancing the numerical strategy used in this research to improve its capability in predicting the load-displacement performance of reinforced concrete deep beams. Finally, the authors recommend the application of the GTM for designing reinforced concrete deep beams providing the flexibility to create reinforcement at any angle, not just restricted to 0º, 90º, or 45º.

7. Acknowledgments

The authors would like to express their gratitude to the Emerging Leaders in the Americas Program (ELAP) for providing Mr. Marcos V. G. Silveira with a scholarship for this research. In addition, the study received partial financial support from the Coordenação de Aperfeiçoamento de Pessoal de Nível Superior – Brasil (CAPES) – Finance Code 001. The experimental work was made possible with the generous support through Dr. Sreekanta Das' NSERC Discovery grant. Dr. Luís A.G. Bitencourt Jr. would like to acknowledge the fellowship of research productivity (PQ) granted by the National Council for Scientific and Technological Development – CNPq (Grant # 307175/2022-7). The authors also appreciate the assistance provided by the Structural Engineering Laboratory technical staff members, Mr. Matthew St. Louis and Mr. Jerome Finnerty. Finally, the authors wish to express their gratitude to Autodesk, Inc. for providing the license for Revit® software. Their support greatly contributed to the success of this research.

8. References

[1] J. Schlaich, K. Schaefer, M. Jennewein, Toward a Consistent Design of Structural Concrete, PCI Journal. (1987). https://doi.org/10.15554/pcij.05011987.74.150.

[2] Canadian Standards Association, Design of Concrete Structures CSA A23.3-19, 2019.

[3] American Concrete Institute, 318-19 Building Code Requirements for Structural Concrete and Commentary, American Concrete Institute, 2019. https://doi.org/10.14359/51716937.

[4] Federation internationale du beton fib, fib Model Code for Concrete Structures 2010, Ernst & Sohn, 2013.

[5] B.S. Maxwell, J.E. Breen, Experimental Evaluation of Strut-and-Tie Model Applied to Deep Beam with Opening, ACI Struct J. 97 (2000). https://doi.org/10.14359/843.

[6] B.S. Chen, M.J. Hagenberger, J.E. Breen, Evaluation of Strut-and-Tie Modeling Applied to Dapped Beam with Opening, ACI Struct J. 99 (2002). https://doi.org/10.14359/12113.

[7] M.T. Ley, K.A. Riding, Widianto, S. Bae, J.E. Breen, Experimental Verification of Strut and Tie Model Design Method, ACI Struct J. 104 (2007). https://doi.org/10.14359/18957.

[8] D. Kuchma, Y. Sukit, T. Nagle, J. Hart, H.Hwang. Lee, Experimental Validation of Strut-and-Tie Method for Complex Regions, ACI Struct J. 105 (2008). https://doi.org/10.14359/19941.

[9] K.S. Ismail, M. Guadagnini, K. Pilakoutas, Shear behavior of reinforced concrete deep beams, ACI Struct J. 114 (2017) 87–99. https://doi.org/10.14359/51689151.

[10] T.K. Mohammedali, A.M. Jalil, K.S. Abdul-Razzaq, A.H. Mohammed, STM experimental verification for reinforced concrete continuous deep beams, International Journal of Civil Engineering and Technology. 10 (2019) 2227–2239.

[11] J.L. Jewett, J. V. Carstensen, Experimental investigation of strut-and-tie layouts in deep RC beams designed with hybrid bi-linear topology optimization, Eng Struct. (2019). https://doi.org/10.1016/j.engstruct.2019.109322.

[12] L. Zhou, Z. Liu, Z. He, Elastic-to-Plastic Strut-and-Tie Model for Deep Beams, Journal of Bridge Engineering. (2018). https://doi.org/10.1061/(ASCE)BE.1943-5592.0001206.

[13] Islam Shabana, Brahim Benmokrane, Ahmed Sabry Farghaly, Shear Strength of GFRP-Reinforced Concrete Squat Walls: A Strut-and-Tie Model, ACI Struct J. 120 (2023). https://doi.org/10.14359/51738347.

[14] Z.-Q. He, Z. Liu, J. Wang, Z.J. Ma, Development of Strut-and-Tie Models Using Load Path in Structural Concrete, Journal of Structural Engineering. 146 (2020). https://doi.org/10.1061/(asce)st.1943-541x.0002631.

[15] N. Stoiber, B. Kromoser, Topology optimization in concrete construction: a systematic review on numerical and experimental investigations, Structural and Multidisciplinary Optimization. 64 (2021) 1725–1749. https://doi.org/10.1007/s00158-021-03019-6.

[16] M.F. Ruiz, A. Muttoni, On development of suitable stress fields for structural concrete, ACI Struct J. 104 (2007) 495–502. https://doi.org/10.14359/18780.

[17] M.V.G. Silveira, B. Paini, L.A.G. Bitencourt Jr, S. Das, Design and experimental investigation of deep beams based on the Generative Tie Method, Eng Struct. 255 (2022) 113913. https://doi.org/10.1016/j.engstruct.2022.113913.
[18] A. Muttoni, M.F. Ruiz, F. Niketic, Design versus assessment of concrete structures using stress fields and strut-and-tie models, ACI Struct J. 112 (2015) 605–615. https://doi.org/10.14359/51687710.
[19] M.V.G. Silveira, L.A.G. Bitencourt, S. Das, A performance-based optimization framework applied to a classical STM-designed deep beam, Structures. 41 (2022) 488–500. https://doi.org/10.1016/j.istruc.2022.05.035.
[20] H. Zhang, Y. Chen, H. Chen, Q. Xiao, W. Xu, Experimental investigation and simulation on load-transfer paths in optimally designed RC deep beams, Eng Struct. 278 (2023). https://doi.org/10.1016/j.engstruct.2022.115469.
[21] A. Pajonk, A. Prieto, U. Blum, U. Knaack, Multi-material additive manufacturing in architecture and construction: A review, Journal of Building Engineering. 45 (2022). https://doi.org/10.1016/j.jobe.2021.103603.
[22] A. Jandyal, I. Chaturvedi, I. Wazir, A. Raina, M.I. Ul Haq, 3D printing – A review of processes, materials and applications in industry 4.0, Sustainable Operations and Computers. 3 (2022) 33–42. https://doi.org/10.1016/j.susoc.2021.09.004.
[23] X. Han, J. Yan, M. Liu, L. Huo, J. Li, Experimental study on large-scale 3D printed concrete walls under axial compression, Autom Constr. 133 (2022). https://doi.org/10.1016/j.autcon.2021.103993.
[24] T. Daungwilailuk, P. Pheinsusom, W. Pansuk, Uniaxial load testing of large-scale 3D-printed concrete wall and finite-element model analysis, Constr Build Mater. 275 (2021). https://doi.org/10.1016/j.conbuildmat.2020.122039.
[25] L. Gardner, Metal additive manufacturing in structural engineering – review, advances, opportunities and outlook, Structures. 47 (2023) 2178–2193. https://doi.org/10.1016/j.istruc.2022.12.039.
[26] V. Laghi, M. Palermo, G. Gasparini, M. Veljkovic, T. Trombetti, Assessment of design mechanical parameters and partial safety factors for Wire-and-Arc Additive Manufactured stainless steel, Eng Struct. 225 (2020). https://doi.org/10.1016/j.engstruct.2020.111314.
[27] C. Buchanan, L. Gardner, Metal 3D printing in construction: A review of methods, research, applications, opportunities and challenges, Eng Struct. 180 (2019) 332–348. https://doi.org/10.1016/j.engstruct.2018.11.045.
[28] S. Huang, X. Deng, Y. Wang, Experimental investigations of optimized 3D Printing Planar X-joints manufactured by stainless steel and high-strength steel, Eng Struct. 285 (2023). https://doi.org/10.1016/j.engstruct.2023.116054.
[29] C. Huang, P. Kyvelou, L. Gardner, Stress-strain curves for wire arc additively manufactured steels, Eng Struct. 279 (2023). https://doi.org/10.1016/j.engstruct.2023.115628.
[30] J. Burger, T. Huber, E. Lloret-Fritschi, J. Mata-Falcón, F. Gramazio, M. Kohler, Design and fabrication of optimised ribbed concrete floor slabs using large scale 3D printed formwork, Autom Constr. 144 (2022). https://doi.org/10.1016/j.autcon.2022.104599.
[31] L. Wang, Y. Yang, L. Yao, G. Ma, Interfacial bonding properties of 3D printed permanent formwork with the post-casted concrete, Cem Concr Compos. 128 (2022). https://doi.org/10.1016/j.cemconcomp.2022.104457.
[32] B. Zhu, B. Nematollahi, J. Pan, Y. Zhang, Z. Zhou, Y. Zhang, 3D concrete printing of permanent formwork for concrete column construction, Cem Concr Compos. 121 (2021). https://doi.org/10.1016/j.cemconcomp.2021.104039.
[33] Canadian Standards Association, Carbon steel bars for concrete reinforcement CSA G30.18-09, 2019.
[34] L.A.G. Bitencourt, O.L. Manzoli, Y.T. Trindade, E.A. Rodrigues, D. Dias-da-Costa, Modeling reinforced concrete structures using coupling finite elements for discrete representation of reinforcements, Finite Elements in Analysis and Design. 149 (2018) 32–44. https://doi.org/10.1016/j.finel.2018.06.004.
[35] M. Cervera, J. Oliver, O. Manzoli, A RATE-DEPENDENT ISOTROPIC DAMAGE MODEL FOR THE SEISMIC ANALYSIS OF CONCRETE DAMS, Earthq Eng Struct Dyn. 25 (1996) 987–1010. https://doi.org/https://doi.org/10.1002/(SICI)1096-9845(199609)25:9<987::AID-EQE599>3.0.CO;2-X.
[36] L.A.G. Bitencourt, O.L. Manzoli, P.G.C. Prazeres, E.A. Rodrigues, T.N. Bittencourt, A coupling technique for non-matching finite element meshes, Comput Methods Appl Mech Eng. 290 (2015) 19–44. https://doi.org/10.1016/j.cma.2015.02.025.
[37] F.J. Vecchio, M.P. Collins, The Modified Compression-Field Theory for Reinforced Concrete Elements Subjected to Shear, ACI Journal. 83 (1986). https://doi.org/10.14359/10416.
[38] ASTM International, A370-19e1: Standard Test Methods and Definitions for Mechanical Testing of Steel Products, American Society for Testing and Materials. (2019). https://doi.org/10.1520/A0370-19E01.
[39] ASTM International, C39/C39M-18: Standard Test Method for Compressive Strength of Cylindrical Concrete Specimens, American Society for Testing and Materials. (2018). https://doi.org/10.1520/C0039_C0039M-18.
[40] GOM, GOM Correlate | GOM, (n.d.). https://www.gom.com/3d-software/gom-correlate.html (accessed June 29, 2020).
[41] J.P. Herranz, H. Santa Maria, S. Gutierrez, R. Riddell, Optimal Strut-and-Tie Models Using Full Homogenization Optimization Method, ACI Struct J. 109 (2012). https://doi.org/10.14359/51684038.
[42] C. Lakavath, S.S. Joshi, S.S. Prakash, Investigation of the effect of steel fibers on the shear crack-opening and crack-slip behavior of prestressed concrete beams using digital image correlation, Eng Struct. 193 (2019) 28–42. https://doi.org/10.1016/j.engstruct.2019.05.030.
[43] R. El Ghadioui, T. Proske, N.L. Tran, C.A. Graubner, Structural behaviour of CFRP reinforced concrete members under bending and shear loads, Materials and Structures/Materiaux et Constructions. 53 (2020). https://doi.org/10.1617/s11527-020-01496-7.
[44] E. Rossi, N. Randl, P. Harsányi, T. Mészöly, Overlapped joints in Textile Reinforced Concrete with UHPC matrix: An experimental investigation, Materials and Structures/Materiaux et Constructions. 54 (2021). https://doi.org/10.1617/s11527-021-01739-1.
[45] M. Kaszubska, R. Kotynia, J.A.O. Barros, H. Baghi, Shear behavior of concrete beams reinforced exclusively with longitudinal glass fiber reinforced polymer bars: Experimental research, Structural Concrete. 19 (2018) 152–161. https://doi.org/10.1002/suco.201700174.
[46] J. Zohreh Heydariha, S. Das, B. Banting, Effect of grout strength and block size on the performance of masonry beam, Constr Build Mater. 157 (2017) 685–693. https://doi.org/https://doi.org/10.1016/j.conbuildmat.2017.09.130.
[47] D. Corr, M. Accardi, L. Graham-Brady, S. Shah, Digital image correlation analysis of interfacial debonding properties and fracture behavior in concrete, Eng Fract Mech. 74 (2007) 109–121. https://doi.org/https://doi.org/10.1016/j.engfracmech.2006.01.035.

5. Research Paper IV

This chapter follows the format of a journal paper entitled "*Design of reinforced concrete deep beams using a Generative Design framework based on Topology Optimization and Generative Tie Method*". This paper has been submitted to a reputable Journal for publication and is currently being reviewed.

Journal

Design of reinforced concrete deep beams using a Generative Design framework based on Topology Optimization and Generative Tie Method

Marcos V. G. Silveira[1a], Luís A.G. Bitencourt Jr.[2a], Sreekanta Das[3b*]

[a] Dept. of Structural and Geotechnical Engineering, University of São Paulo, São Paulo, SP, Brazil 05508-010.
b Dept. of Civil and Environmental Engineering, University of Windsor, Windsor, ON, Canada N9B 3P4.

ARTICLE INFO

Keywords:
Generative Design (GD)
Topology Optimization (TO)
Generative Tie Method (GTM)
Strut-and-Tie Method (STM)
Large-scale tests
Finite Element Analysis (FEA)

ABSTRACT

This research paper explores the design of structural concrete (SC) deep beams using a generative design framework that combines Topology Optimization and the Generative Tie Method (GTM). Through a comprehensive investigation involving computational simulations using Finite Element Analysis (FEA) and rigorous large-scale experimental testing, insights into the optimization strategies of SC deep beams are provided. The FEA results exhibited strong agreement with the experimental findings, highlighting the efficacy of the utilized numerical strategy in accurately predicting the performance of optimized deep beams during the design process. The key findings of this study indicate that the GTM is an effective tool for designing deep beams, whether or not they incorporate Topology Optimization. Specimens designed in accordance with the GTM, with an allowable value of compressive strength reduction in concrete (η_adm) set to 0.5, exhibited improved ductility responses compared to specimens designed with η_adm equal to 0.7. The topology optimization process significantly influenced stress distribution, cracking behavior, and overall ductility. The GTM-designed specimens outperformed the specimen designed using the Strut-and-Tie method in terms of ductility and material optimization. The generative design framework, integrating Topology Optimization and the GTM, demonstrates promising outcomes for the design of complex-shaped SC members.

1. Introduction

The design of reinforcement layout for structural concrete discontinuous members, known as D-regions, requires careful consideration due to their unique characteristics. These D-regions include various structural elements such as pile caps, beam-column joints, frame corners, corbels, deep beams, holes, and support regions. The primary approach employed for their design is the strut-and-tie method (STM), which gained significant attention following the publication by Schlaich et al. in 1986 [1]. Leading structural concrete design codes, including the Canadian standard [2], American Concrete Institute (ACI) building code [3], and *fib* Model Code [4], incorporate provisions and guidelines for the design of D-regions using the STM. However, the application of the STM presents a notable challenge in the development of idealized trusses. As a result, researchers are actively investigating and developing frameworks that integrate Topology Optimization (TO) to address this inherent limitation and enhance the design of D-regions.

According to Zhang et al.[5], TO is a mathematical approach utilized in engineering to optimize the arrangement of materials within a defined design space. Topology optimization aims to determine the most efficient and resilient structural arrangement of material while satisfying certain performance criteria or objectives. In traditional design processes, engineers often start with a predefined shape or structure and make incremental changes to improve its performance. Topology optimization allows designers to establish design requirements and constraints, such as maximum stress, minimum weight, or desired mass reduction targets. The process involves iteratively removing material from various regions within the design space and evaluating the resulting design's performance through finite element analysis or other computational methods [6]. These evaluations help determine which regions contribute most effectively to the desired objectives and which regions can be removed or reduced, respecting the design requirements and constraints.

Although TO has proven to be a valuable tool for designers in proposing equivalent trusses within the STM framework [6–9], its applicability extends further to the realm of structural shape conception [10–14]. Beghini et al. [14] highlight the importance of collaborative efforts between architecture and engineering in the construction industry. An alternative approach that employs a customized structural TO framework to facilitate the generation of integrated design ideas is proposed in [14]. However, the application of TO to achieve optimal forms presents significant challenges in the construction process and reinforcement layout design [6,7,15–17] due to the organic-looking shapes obtained [16]. In the specific context of this research, the resulting design from topology optimization is further simplified to align with the manufacturing process employed, the regular plywood formwork method. Despite simplifying the shapes obtained through topology optimization, designing the reinforcement layout using conventional methods such as the STM still presents challenges [15,16]. Therefore, to address those challenges, this research applies the Generative Tie Method (GTM) [18,19] to the design of the reinforcement layout of the optimized members.

The GTM is a nonlinear procedure that employs finite element analysis (FEA) to iteratively generate the reinforcement layout of structu-

[1] Ph.D. Candidate.
[2] Assistant Professor.
[3] Professor.
* Corresponding author: sdas@uwindsor.ca

Nomenclature

Abbreviations and Symbols	Description		
ACI	American Concrete Institute	τ_{max}	Maximum value of bond stress (*fib*)
DAQ	Data acquisition system	$f'_{c\,exp}$	Experimental concrete compressive strength
DIC	Digital image correlation	f_y	Specified reinforcement yield strength
D-regions	Discontinuous regions	P_u/V_{conc}	Ratio/relationship between the ultimate load and the volume of concrete employed
EPSF	Elastic-plastic stress fields	P_{crack}	Applied load while the first measurable crack (0.1 mm of width) appears
FEA	Finite element analysis	P_u	Experimental ultimate/failure applied load
GD	Generative design	P_u/W_{Reinf}	Ratio/relationship between the ultimate load and the total weight of the reinforcement cage
GTM	Generative tie method	P_y	Applied load while reinforcement reaches the yielding
LVDT	Linear variable differential transformers	S_1	Slip I (*fib*)
MCFT	Modified compression-field theory	S_2	Slip II (*fib*)
MDR	Minimum distributed reinforcement	S_3	Slip III (*fib*)
RC	Reinforced concrete	V_{conc}	volume of concrete
SC	Structural concrete	W_{Reinf}	Weight of steel reinforcement used in each specimen
STM	Strut-and-tie method	δ_u/δ_y	Ductility ratio
TO	Topology optimization	η_{adm}	Admissible/allowable level of tensile strain in concrete within GTM
f'_c	Specified concrete compressive strength	τ_f	Shear friction capacity (*fib*)

ral concrete (SC) members [18,19]. This method follows a systematic five-step process, which initiates with the application of FEA to an initial trial numerical model employing the minimum distributed reinforcement (MDR) usually mandatory by structural codes and standards. Subsequently, the model undergoes iterative refinement based on interactive FEA analysis. The FEA strategy incorporated within the GTM is the one proposed by Ruiz & Muttoni [20], which integrates the Elastic-Plastic Stress Fields (EPSF) [21,22]. The EPSF formulation adopts the Modified Compression-field Theory (MCFT) [23] to capture the loss in compressive strength exhibited by concrete under significant tensile strain. The GTM algorithm has the capability to increase the diameter or quantity of existing rebars within the MDR model and also strategically introduce new rebars (ties) in identified positions. Overall, applying GTM has resulted in significant advancements in the efficiency of reinforcement concrete (RC) member design, significantly elevating the precision and reliability of the reinforcement layout [18,19].

The integration of the Generative Tie Method and Topology Optimization for the structural design of the investigated deep beams is achieved in this research through the application of the Generative Design (GD) methodology. According to Alsakka et al. [24], GD methods utilize computational capabilities to create alternative designs that meet a defined set of objectives and criteria, encompassing factors such as performance, materials, manufacturing techniques, and costs. Conforming to Sivam [25], pioneer investigations in GD were performed by Frazer in the early 1970s [26]. According to Shea et al. [27], GD systems aim to create new design processes that produce unprecedented and buildable elements using the current computing and manufacturing resources. Also according to Shea et al. [27], the GD method can be seen as a collaborative partner in the design process, capable of generating design ideas in response to robust and rigorous computational models of design constraints and performance criteria.

According to Sun and Ma [28], GD encompasses the exploration of multiple design variants and the evaluation of their performance. Unlike traditional optimization processes focusing on a single optimal design, GD aims to generate a range of design solutions by manipulating multiple variants. Prominent studies in various domains have been highlighted, showcasing their significant contributions to the field of GD in different industries. Sydora & Stroulia [29] conducted investigations into the use of GD techniques within the context of interior design applications. Gan [30] has focused on generative design in modular construction design. Gonzalez-Delgado et al. [31] have made notable advancements in the structural design of wind turbines also using GD. Zhang et al. [32] have explored generative design in the early stages of residential building designs. Furthermore, Caetano et al. [33] have critically examined the terminologies surrounding computational design, particularly generative design, through an extensive literature review incorporating multiple definitions proposed by various authors.

This research paper aims to explore and advance the design of RC deep beams by leveraging a generative design framework that combines Topology Optimization and the Generative Tie Method. The effectiveness of the proposed GD approach for RC deep beams is thoroughly examined through a comprehensive investigation, including computational simulations using FEA and large-scale experimental testing. Performance comparisons are conducted between four optimized large-scale specimens, as well as three additional large-scale specimens with different design parameters previously studied by the same authors [7,19]. The results demonstrate the promising potential of integrating Topology Optimization and the Generative Tie Method within the generative design framework, offering significant advancements in the design of complex-shaped structural concrete members.

2. Design of the Specimens

This research paper presents a generative design framework that integrates two distinct methods: Topology Optimization and Generative Tie Method [18,19]. Topology optimization iteratively removes material from the design space to optimize performance based on FEA. The outcomes of TO often result in complex and organic designs, which can present challenges when applying traditional design methods such as the STM. Consequently, within this research, the reinforcement layout design of the optimized members is carried out using the GTM, a nonlinear procedure that utilizes FEA to determine the arrangement of reinforcement bars in SC members iteratively. The proposed GD framework serves as a mediator between TO, which focuses on material removal, and the GTM, which focuses on generating reinforcement bars where needed. This GD framework aims to achieve a balance between the two approaches, as demonstrated in Figures 1 and 6.

The parameters of both approaches are systematically examined to explore their potential for generating optimized design solutions for structural concrete members. As shown in Figure 1, the design decisions are thoroughly made in three hierarchical levels, each building upon the outcomes of the previous level. The first level involves applying TO to find

the optimized shape of the component. In the second level, the optimized shape obtained from the previous step is modified to accommodate construction method limitations, such as the use of regular formwork techniques with plywood formwork or similar. Additionally, the MDR, often required by the main structural concrete building codes, is modeled at this stage. Finally, the GTM is applied in the last stage to design the reinforcement layout [18,19]. A set of metrics is generated to support designers in objectively evaluating and comparing different design solutions.

In this study, the classical deep beam with a large opening proposed by Schlaich et al. [1] is designed under the proposed generative design framework. Specifically, the TO approach is applied to the studied structural component, targeting 70% and 55% of mass reductions. The resulting optimized designs are illustrated in Figure 2. Further details about the software utilized in this study can be obtained from [34]. As manufacturing automation processes were not considered in this study, the optimized shapes obtained by applying TO (Figure 2) have been regularized to comply with the limitations of the construction process employed, plywood formwork. The simplified geometries for the specimens with mass targets of 70% and 55% obtained through the application of TO are shown in Figures 3a) and 3b), respectively. The MDR layout for each specimen was designed in accordance with the requirements of ACI 318-19 [3]. Figure 4 displays the MDR layouts for both geometries, where each reinforcement bar position represents two layers of 10M [35].

The reinforcement layout was designed using the GTM [18,19]. According to Silveira et al. [18], the definition of the allowable value of compressive strength reduction in the concrete within the GTM (η_{adm}) holds significant importance in the SC member performance. In accordance with prior research [19], the specimens under investigation were devised with η_{adm} values of 0.5 and 0.7 for each initial model illustrated in Figure 4. As a consequence, four specimens were produced, as outlined in Table 1. The specified compressive strength of (f_c') 40 MPa and a maximum coarse aggregate diameter of 12.7 mm (1/2") were adopted in the design of four structural concrete specimens. The reinforcement cage was composed of 10M and 15M steel rebars of the 400W type, which have yield strength (f_y) of 400 MPa [2,35]. The first two specimens, SIV.a and SIV.b, had 70% of the original concrete volume (Figure 4a). SIV.a was designed with an η_{adm} value of 0.5, while SIV.b was designed with η_{adm} = 0.7. The remaining two specimens, SIV.c and SIV.d, had a reduction concrete volume of 45% and were designed based on the MDR layout presented in Figure 4. SIV.c was designed with an η_{adm} value of 0.5, while SIV.d was designed with η_{adm} = 0.7. Table 1 provides an overview of the design parameters employed for each specimen in the research program.

Table 2 presents the design history of each specimen. Notably, the design of specimens SIV.b and SIV.d with η_{adm} equal to 0.7 was driven by the chosen η_{adm}, and no reinforcement yielding was reached during the design process. In contrast, SIV.a and SIV.c with η_{adm} equal to 0.5 exhibited a different pathway. Figure 5 shows the reinforcement layouts for all four specimens studied in this research. Figure 6 provides a more detailed presentation of the proposed generative design framework, which employs Topology Optimization for geometry conception and the Generative Tie Method for the reinforcement layout design, as summarized in Figure 1.

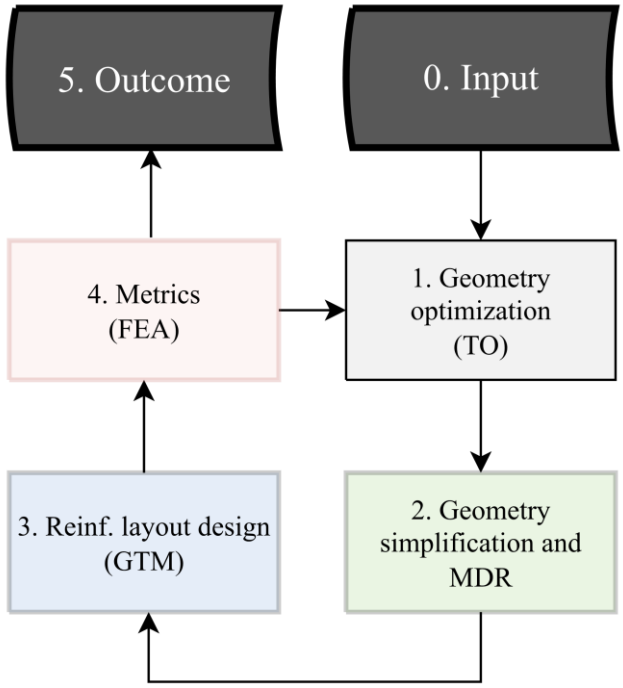

Figure 1 – Proposed Generative Design Framework.

Table 1 – Summary of the test matrix.

Sp.	TO target mass	GTM η_{adm}
SIVa	70%	0.5
SIVb	70%	0.7
SIVc	55%	0.5
SIVd	55%	0.7

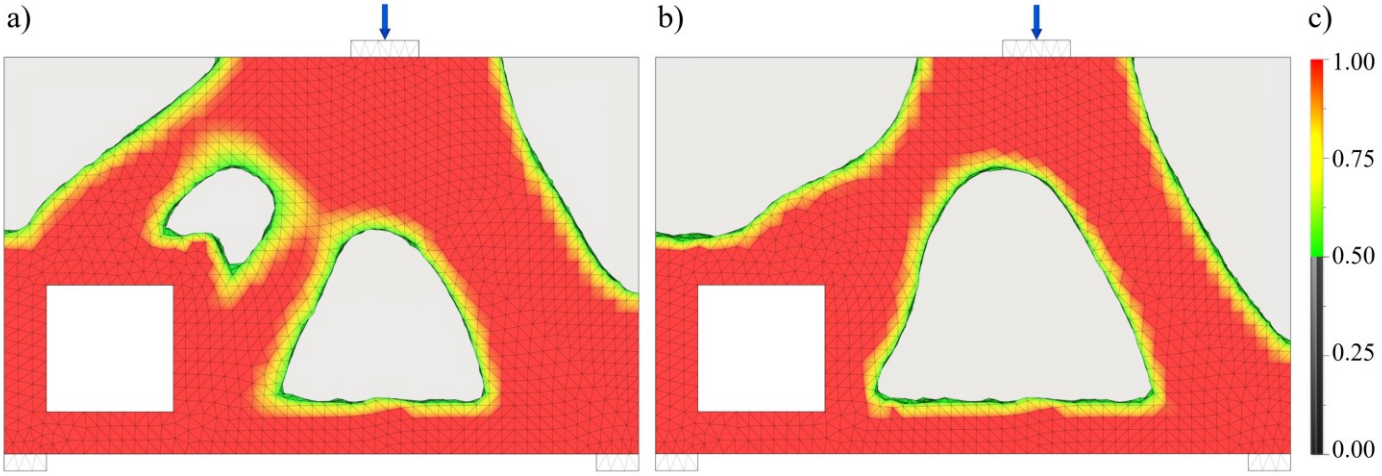

Figure 2 – Topology optimization results using Autodesk Fusion 360: a) target mass of 70%; and b) target mass of 55%.

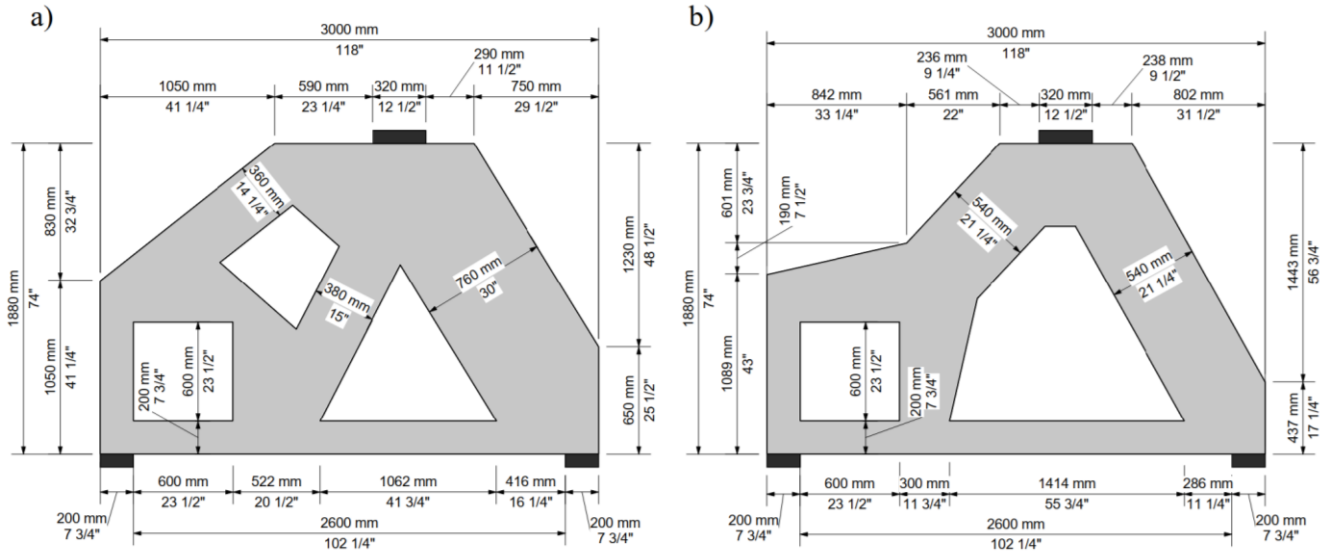

Figure 3 –Specimen simplified geometry based on topology optimization: a) 70% of the original concrete volume; and b) 55% of the original concrete volume.

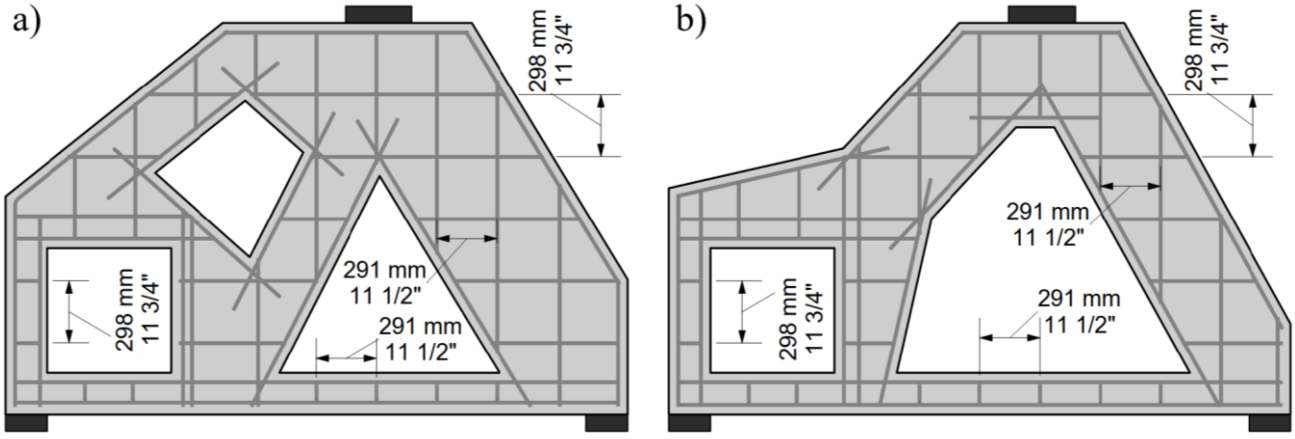

Figure 4 – Specimens minimum distributed reinforcement: a) 70% of the original concrete volume; and b) 55% of the original concrete volume.

3. Numerical Simulation

The performance of the investigated reinforced concrete deep beams was predicted using a 2D finite element analysis. Various aspects of the deep beams' behavior, including deflection, stress fields, crack patterns, and failure mechanisms, were used to enhance the experimental investigation. The discretization of the concrete was achieved through constant strain triangle elements [7]. The concrete behavior was modeled using a constitutive damage model integrated with an implicit-explicit scheme proposed by Bitencourt et al. [36]. The FEA strategy implemented to represent the material failure process incorporated the damage approach presented by Cervera et al. [37], which utilized two independent scalar damage variables to describe the distinct tension and compression behaviors. The reinforcement bars were modeled using truss finite elements with an elastoplastic constitutive model, as used in a previous publication by the authors [19].

To account for the bond-slip phenomenon between the reinforcement bars and concrete, the coupling finite elements - as proposed by Bitencourt et al. [38] - were employed. The constitutive model for the bond-slip adopted in this research was inspired by the one proposed in the *fib* Model Code 2010 [4]. The schematic of the coupling finite element used for modeling the debonding mechanism is illustrated by Silveira et al. [7,19], with the following parameters: $\tau_{max} = 16.4\ MPa$, $\tau_f = 6.6\ MPa$, S_1=*1 mm*, S_2=*2 mm*, S_3=*25 mm*, and $\alpha = 0.4$. The numerical simulations were conducted using fundamental parameters obtained through the experimental program (Section 4) for material characterization, including concrete compressive strength, modulus of elasticity of reinforcement bars, yielding stress, and ultimate stress. In contrast to prior research conducted by the same authors [7,19], the FEA strategy employed in this study does not incorporate the MCFT.

4. Experimental Program

The experimental program, which encompassed the fabrication, preparation, and testing of the specimens, was carried out in the Structural Engineering Laboratory at the University of Windsor, Canada. All reinforced concrete elements were constructed using 10M and 15M reinforcement bars made from 400 W steel [2,35]. The reinforcement bars underwent testing in accordance with [39], revealing yielding stress, ultimate stress, and modulus of elasticity values of 495.1 MPa, 730.5 MPa, and 269.2 GPa, respectively. The experimental compressive strength of the concrete ($f'_{c\ exp}$) was determined via the cylinder test and found to be 43.2 MPa, in accordance with the procedures stipulated in [40].

4.1 Specimen fabrication and preparation

Specimens SIVa, SIVb, SIVc, and SIVd were constructed at full-scale to undergo experimental testing using the setup shown in Figure 8. Figures 7a) and 7c) display the specimens prior to concrete casting, while Figures 7b) and 7d) depict them upon completion of the casting process. Specimen SIV.a is shown at the top of Figures 7a) and 7b), while SIV.b appears at the bottom of the same figures. Specimen SIV.c is displayed at the top of Figures 7c) and 7d), while SIV.d appears at the bottom of the same figures. Ten 5-mm strain gauges were affixed suitably to the reinforcement cage in five distinct locations in each specimen, as depicted

Table 2 – A record of decisions made by the Generative Tie Method on the design of SIVa, SIVb, SIVc and SIVd.

Step	η_{min}	Reinf. Yielding?	Function	Design decisions
SIV.a				
0-37	>0.50	no	Increase load	-
38	0.49	yes	Create reinforcement	Short reinforcement bars with tension in their end were extended; Inclined reinforcement bars created between two openings and; Rebar created below the square opening.
38-54	>0.50	no	Increase load	
55	0.57	yes	Create reinforcement	Inclined rebar created between two openings.
55-64	>0.50	no	Increase load	
65	0.59	yes	Create reinforcement	Inclined rebar created between two openings.
65-71	>0.50	no	Increase load	
72	0.6	yes	Increase the number of rebars	Rebar created below the square opening.
72	>0.50	no	Outcome	
SIV.b				
0-18	>0.70	no	Increase load	
19	0.69	no	Create reinforcement	Short reinforcement bars with tension in their end were extended and; Inclined reinforcement bars created between two openings
19-34	>0.70	no	Increase load	
35	0.69	no	Create reinforcement	Diagonal, horizontal, and vertical reinforcement bars created between two openings.
35-43	>0.70	no	Increase load	
44	0.69	no	Create reinforcement	Diagonal, horizontal, and vertical reinforcement bars created between two openings.
44-49	>0.70	no	Increase load	
50	0.69	no	Create reinforcement	Horizontal, and vertical reinforcement bars created between two openings.
50-54	>0.70	no	Increase load	
55	0.69	no	Increase diameter	Rebar below the square opening had the diameter increased.
55	>0.70	no	Increase load	
56	0.69	no	Create reinforcement	Rebar created below the square opening.
56-64	>0.70	no	Increase load	
65	0.69	no	Increase diameter	Inclined rebar between two openings had the diameter increased.
65-71	>0.70	no	Increase load	
72	>0.70	no	Outcome	
SIV.c				
0-29	>0.50	no	Increase load	
30	>0.50	yes	Create reinforcement	Rebar created below the opening.
30-41	>0.50	no	Increase load	
42	>0.50	yes	Increase diameter	Rebar below the opening had the diameter increased.
42-44	>0.50	no	Increase load	
45	>0.50	yes	Increase diameter	Rebar below the opening had the diameter increased.
45-50	>0.50	no	Increase load	
51	>0.50	yes	Increase diameter	Rebar below the opening had the

				diameter increased.
51-54	>0.50	no	Increase load	
55	>0.50	yes	Increase the number of rebar	The number of vertical bars at the far-left position has been increased.
55-59	>0.50	no	Increase load	
60	>0.50	yes	Create reinforcement	Horizontal, and vertical reinforcement bars created on top of the square opening.
60-64	>0.50	no	Increase load	
65	>0.50	yes	Create reinforcement	Horizontal, and vertical reinforcement bars created on top of the square opening.
65-71	>0.50	no	Increase load	
72	0.47	yes	Create reinforcement	Horizontal reinforcement bar created on top of the square opening.
72	>0.50	no	Outcome	
SIV.d				
0-19	>0.50	no	Increase load	
20	0.69	no	Create reinforcement	Inclined reinforcement bars created in the upper right corner of the square opening.
20-24	>0.50	no	Increase load	
25	0.69	no	Create reinforcement	Inclined reinforcement bars created in the upper right corner of the square opening, and stirrup created below the square opening.
25-27	>0.50	no	Increase load	
28	0.69	no	Create reinforcement	Stirrup created below the square opening.
28-34	>0.50	no	Increase load	
35	>0.70	yes	Create reinforcement	Rebar created below the square opening.
35-39	>0.50	no	Increase load	
40	0.69	no	Create reinforcement	Inclined reinforcement bars created in the upper right corner of the square opening.
40-49	>0.50	no	Increase load	
50	0.69	yes	Increase diameter	Rebar in the upper right corner of the square opening had the diameter increased.
50-54	>0.50	no	Increase load	
55	0.69	no	Create reinforcement	Rebar created below the square opening.
55-64	>0.50	no	Increase load	
65	0.69	no	Increase diameter	Three reinforcement bars below the opening had their diameter increased.
65-71	>0.50	no	Increase load	
72	0.69	yes	Create reinforcement	Rebar created below the square opening.
72	>0.50	no	Outcome	

in Figure 8. Additionally, speckle paints were administered to the front face of each specimen and the steel supports, as demonstrated in Figure 9, to augment the digital image correlation (DIC) analysis.

4.2 Test setup

The loading scheme used for the experimental tests was achieved by employing a high-load capacity reaction structure. The latter consisted of a 1.2m thick concrete floor, two 1.2m thick walls, and a steel assembly made of two I-beams, as illustrated in Figure 8. The support assemblies, which comprise steel stands and thick steel plates, are also visible in Figure 8a). The load actuator, possessing a 2000 kN capacity, is connected to the I-beams assembly. Two types of instrumentation were used during the experimental tests: physical and contactless. Physical instrumentation involved a load cell at the load actuator, four Linear Variable Differential Transformers (LVDT), and ten steel strain gauges. Two LVDTs were placed underneath the specimen in order to measure the displacement of the bottom surface of each deep beam, as demonstrated in Figure 8a. The third LVDT was placed on the rear side of the specimen to capture any potential out-of-plane displacement during the test (refer to Figure 8b). The fourth LVDT was attached to the load actuator to measure its stroke during the load application.

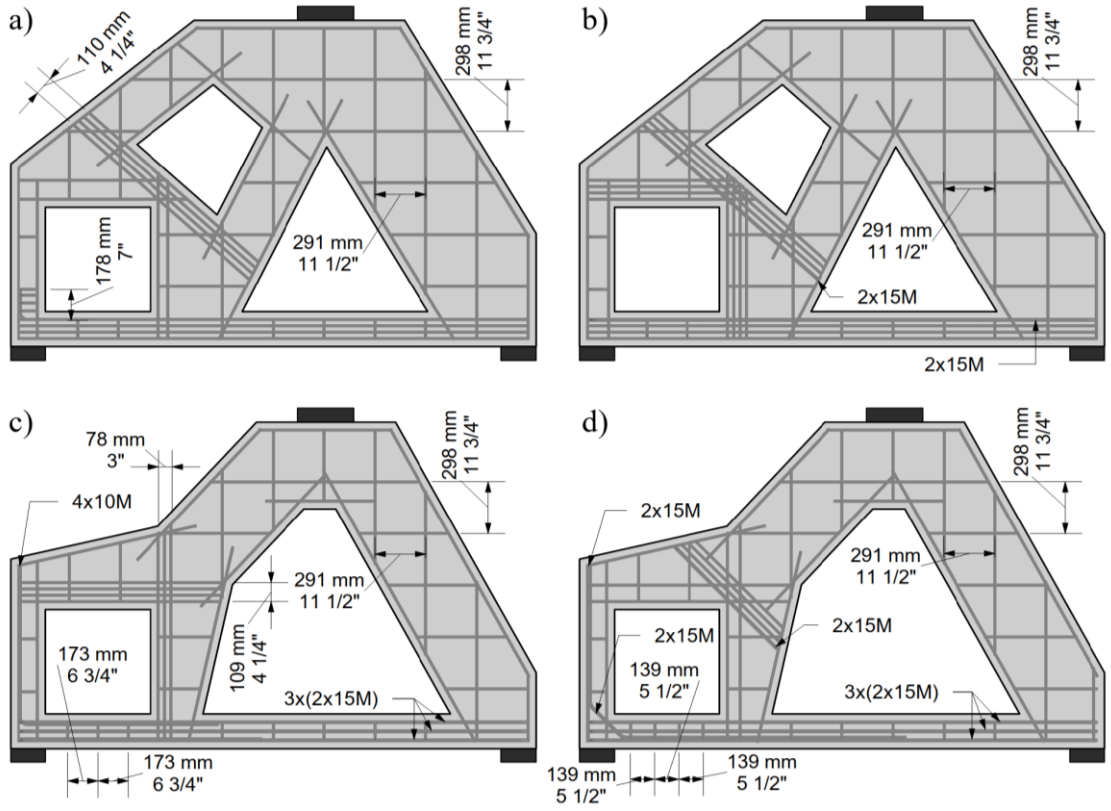

Figure 5 – Reinforcement layout designed using the GTM: a) SIV.a; b) SIV.b; c) SIV.c; and d) SIV.d.

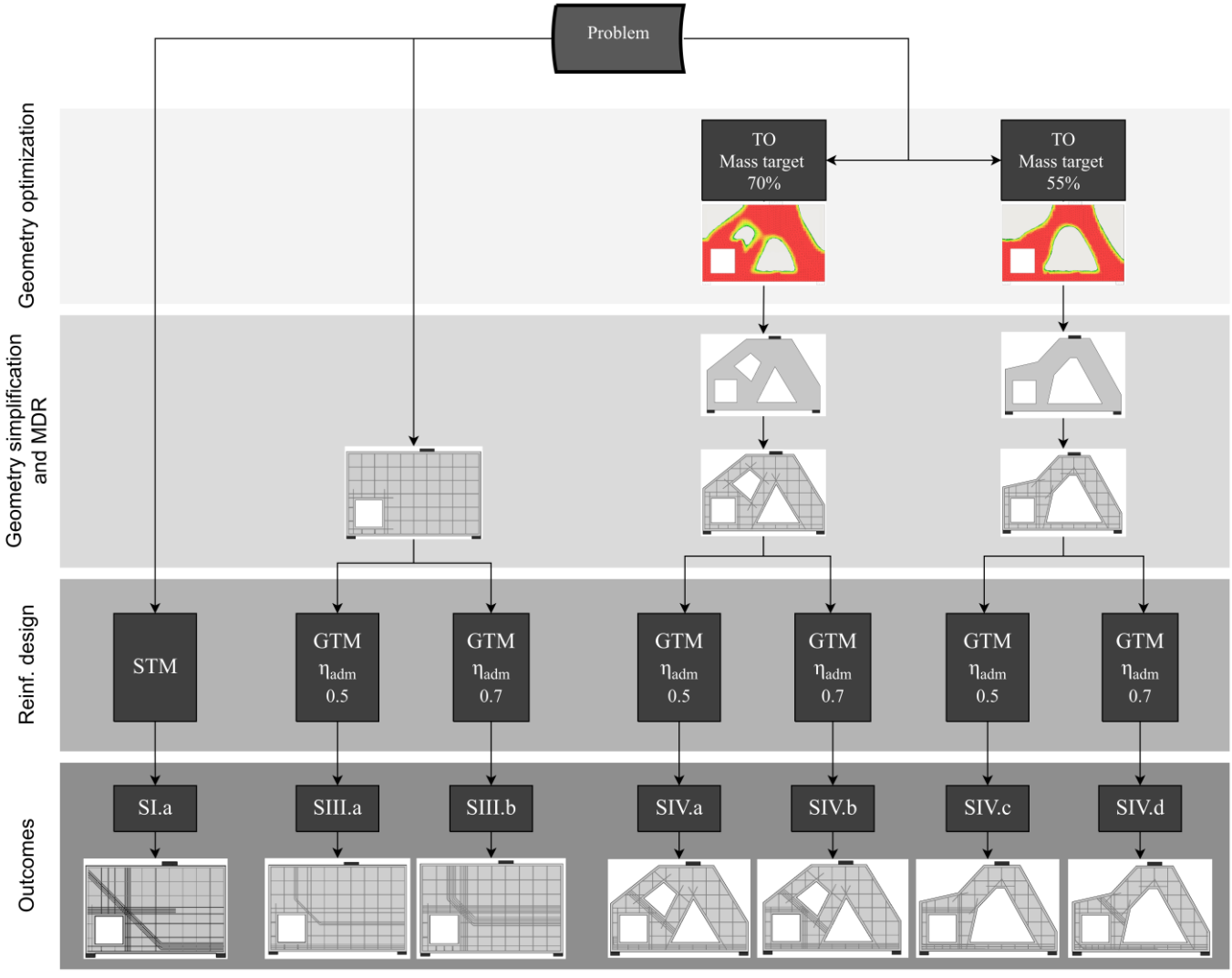

Figure 6 –The proposed generative design framework flowchart.

The contactless instrumentation was based on the digital image correlation technique. To obtain DIC data, four cameras were employed, located in the front of each specimen and capturing images every 6 seconds. The left and right cameras shown in Figures 8 and 9 were mounted in portrait orientation, with each camera covering half of the specimens. Additionally, two DIC cameras, designated as Support A Camera and Support B Camera in Figures 8 and 9, were positioned near each support to closely monitor the displacements in the support regions. The acquired photographs were later processed using *GOM correlate* [41]. These readings were subsequently used to investigate the boundary conditions of the specimens during the tests. The physical and contactless instrumentation data was collected by a proprietary data acquisition system (DAQ). Furthermore, a portable camera with a wide field of view (GoPro) was situated in front of the test setup to capture the entire scene. To enhance the DIC results, two professional studio lights with color and intensity control were employed, as depicted in Figure 9.

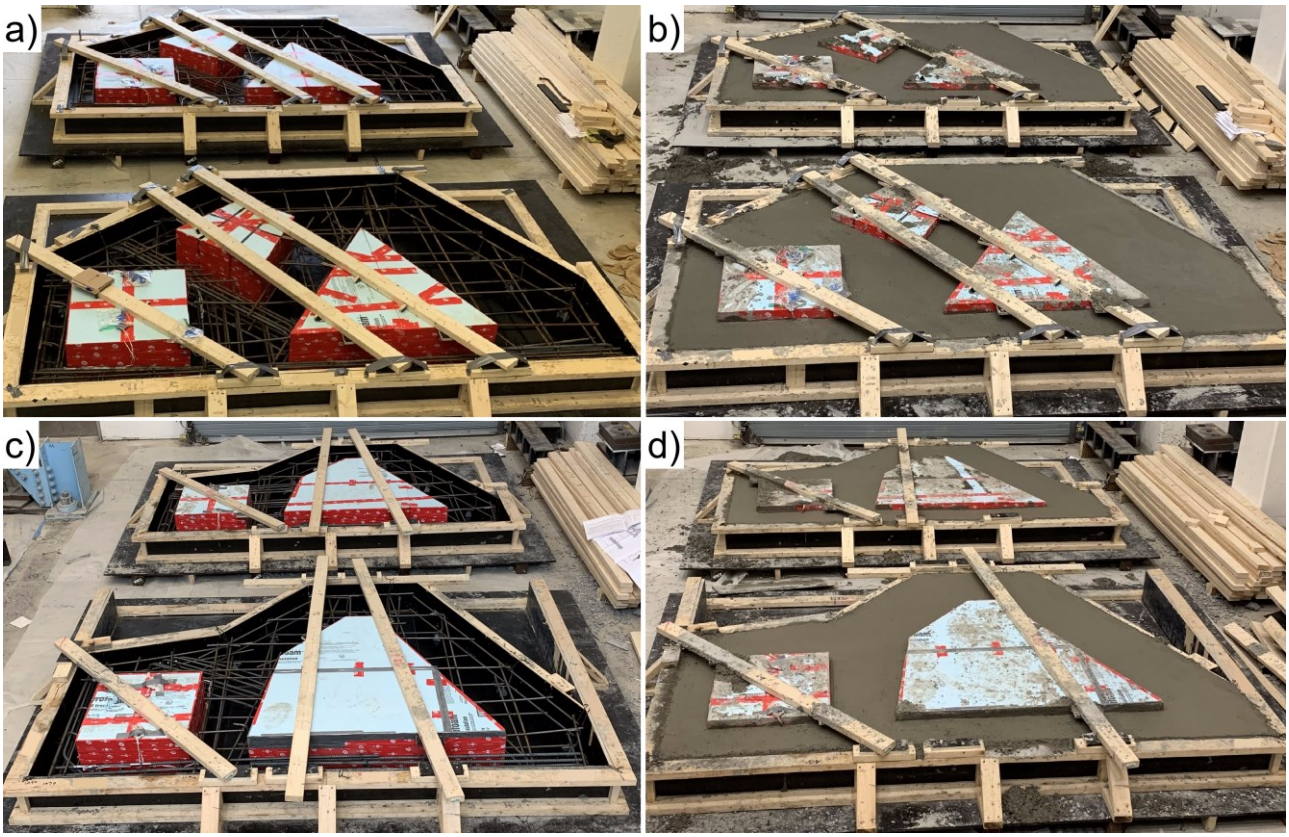

Figure 7 – Preparation of the specimens: a) SIV.a (top) and SIV.b (bottom) before concrete casting; b) SIV.a (top) and SIV.b (bottom) after concrete casting; c) SIV.c (top) and SIV.d (bottom) before concrete casting; and d) SIV.c (top) and SIV.d (bottom) after concrete casting.

5. Results and Discussions

Figure 10 displays the relationship between the applied load and deflection for the four examined specimens. The noticeable differences in initial stiffness among the specimens are directly attributed to the variations in the amount of concrete and reinforcement utilized. The specimens with a greater quantity of concrete and reinforcement demonstrate higher initial stiffness. Specifically, in terms of decreasing stiffness, the order of the specimens is as follows: SIVb, SIVa, SIVd, and SIVc. Notably, the load-deflection curves of SIVa and SIVc, designed with a GTM parameter η_{adm} equal to 0.5, exhibited more pronounced horizontal plateaus, indicating improved ductility. Additionally, specimens designed with a GTM parameter η_{adm} equal to 0.7 also exhibited notable horizontal plateaus in their load-deflection curves, suggesting satisfactory ductility. When comparing specimens with the same volume of concrete or mass target, specifically 70% (SIVa and SIVb) and 55% (SIVc and SIVd), the data presented in Table 2 demonstrates that the specimens designed with a GTM parameter η_{adm} equal to 0.7 exhibited significantly higher ultimate loads.

Table 3 presents the experimental results of reinforced concrete deep beams with varying design parameters, as indicated in Table 1. The performance of the specimens was evaluated based on several key measurements. The ultimate load (P_u) column represents the maximum load sustained by each specimen before failure. The symbol P_y indicates the applied load at the point of initial reinforcement bar yielding. The location where the rebar yielding was observed is also shown in Table 3. The applied load at the occurrence of the first visible crack, with a width of 0.1 mm, is presented in Table 3 as P_{crack}. Lastly, the widest crack observed when the specimens were subjected to the ultimate load is exhibited in millimeters.

SIVb demonstrates the highest Ultimate Load of 1616 kN, followed closely by SIVa with a load of 1344 kN. SIVd and SIVc exhibit lower Ultimate Loads of 874 kN and 714 kN, respectively. The strain gauges affixed to the reinforcement cage at position S2 (refer to Figure 8) captured the initial yielding of SIVa, SIVb, and SIVd, indicating the commencement of yielding at that location. However, the precise position of yielding for SIVc remains undetermined. Furthermore, the applied load when the first cracks were visible (0.1 mm wide) for SIVa, SIVb, SIVc, and SIVd were 230 kN, 318 kN, 214 kN, and 183 kN, respectively. The maximum crack widths when the specimens were under the ultimate load were 3.0 mm, 1.9 mm, 3.7 mm, and 5.0 mm for SIVa, SIVb, SIVc, and SIVd, respectively.

The visualization of the principal major strain distribution using the DIC technique under the ultimate load is depicted in Figure 11. The figure provides individual visualizations for each specimen: SIVa, SIVb, SIVc, and SIVd. The visualization of the tensile strain patterns is closely correlated with the observed crack patterns in the specimens. Notably, the crack width measurements at positions Crack1 and Crack3 were consistent across all four specimens. However, variations were observed in the crack widths measured at position Crack2, particularly between SIVa and the other three specimens. Quasi-vertical cracks, originating from the left support region and extending upwards towards the square opening, were observed in SIVb, SIVc, and SIVd. Consequently, measurements for this region were obtained by summing the crack widths in the vicinity. The graphics depicting the evolution of crack widths captured via digital image correlation are shown in Figure 12. The approach employed in measuring crack widths using the DIC technique

aligns with the methodology adopted in previous research studies, including references [18,42,43]. For SIVa, the widest cracks occurred at the Crack2 position. In contrast, for SIVb, the Crack3 position exhibited the largest opening under the ultimate load. Notably, the two specimens designed with the topology optimization mass target of 55%, SIVc, and SIVd, demonstrated maximum crack widths at the Crack2 position.

Table 3 – Summary of experimental results.

Sp.	P_u	P_y	Position of 1st rebar yielding	P_{crack}	Maximum Crack width
	(kN)	(kN)		(kN)	(mm)
SIVa	1344	636	S2	230	3.0
SIVb	1616	903	S2	318	1.9
SIVc	714	582	Unknown	214	3.7
SIVd	874	685	S2	183	5.0

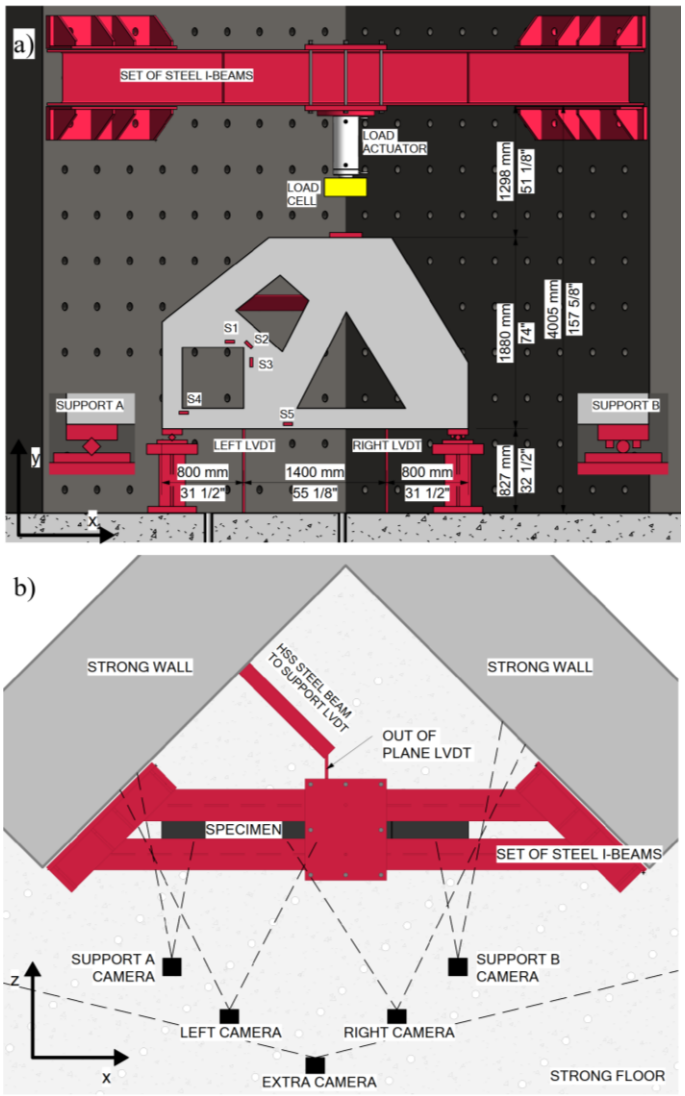

Figure 8 – Test setup scheme: a) elevation, and b) plan view.

Figure 13 provides photographs of the specimens following the completion of the tests. SIVa exhibited shear failure along the diagonal line formed by the right side of the left support region and the bottom right corner of the square opening. Similarly, SIVb and SIVc experienced shear failure along the vertical component formed on the left side of the opening, with the fracture plane extending from the line between the left side of the left support upwards towards the square opening. SIVd displayed a notable crack at the same position as observed in SIVb and SIVc. However, the failure in SIVd occurred along the diagonal line, starting from the upper left corner of the square opening and extending upwards, as shown in Figure 13d).

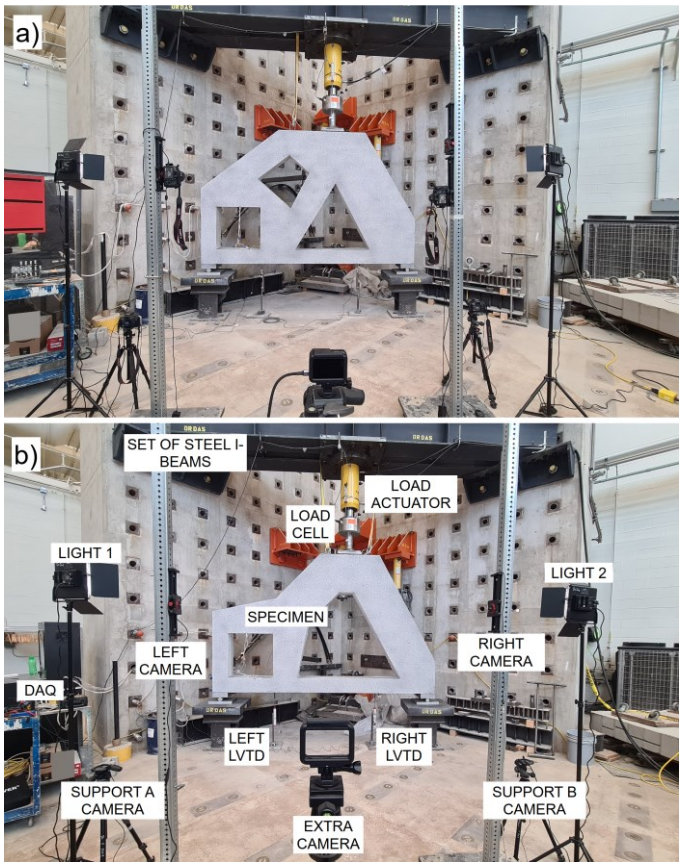

Figure 9 – Test setup photographs: a) SIV.a; and b) SIV.c.

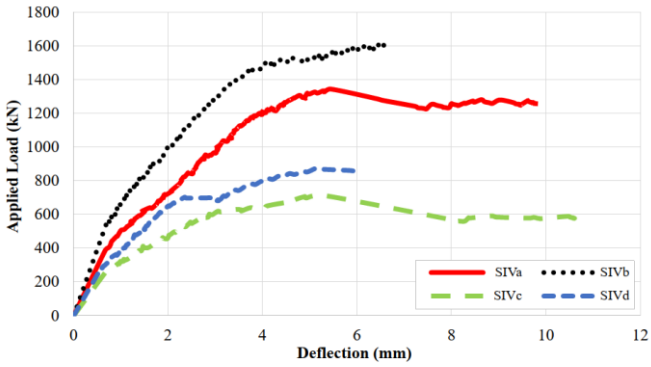

Figure 10 - Applied load *vs.* deflection curves obtained from the experimental program for the specimens SIVa, SIVb, SIVc, and SIVd.

Figure 14 illustrates a comparative analysis of the applied load *vs.* deflection curves, showcasing the experimental program and numerical simulations for the four studied specimens: a) SIVa; b) SIVb; c) SIVc; and d) SIVd. The deflection measurements were precisely captured at the left LVDT position, as depicted in Figure 8. Noteworthy findings include the numerical predictions accurately capturing the variations in stiffness throughout the loading process, effectively reflecting the phenomena of cracking and yielding. Furthermore, the numerical simulations exhibited high precision in predicting both the maximum displacements and ultimate loads. Table 4 provides comparisons between the numerical predictions and experimental results for the ultimate load. It should be highlighted that the numerical response for the specimen designed with a 70% mass target and η_{adm} of 0.7, SIVb, exhibited a softer curve compared to the experimental data. This observation is further supported by the results presented in Table 4, where the most substantial deviation between the predictions and results was observed for the SIVb specimen (-7.0%).

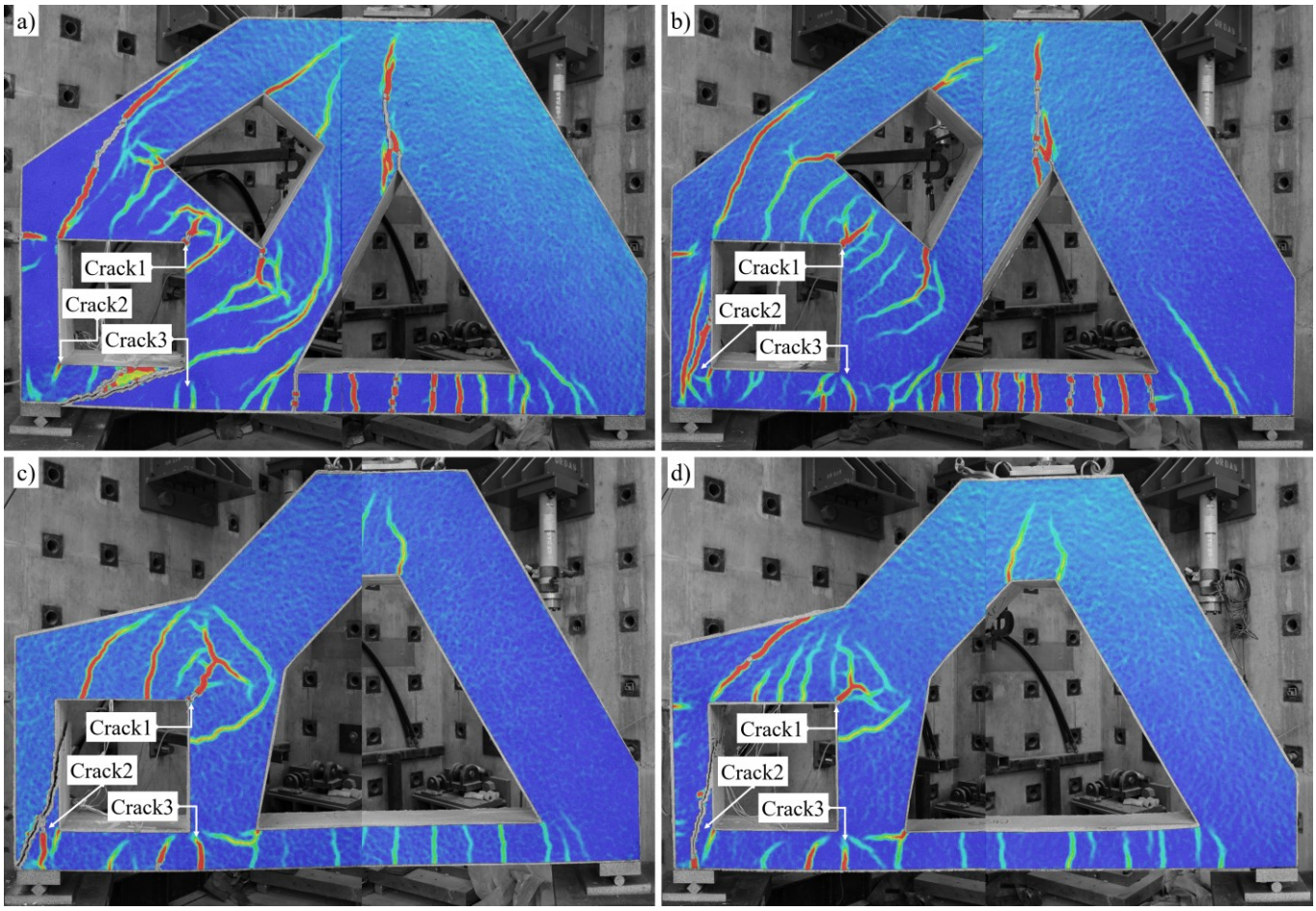

Figure 11 – Visualization of principal major strain distribution using the DIC technique under ultimate load: a) SIVa; b) SIVb; c) SIVc; and d) SIVd.

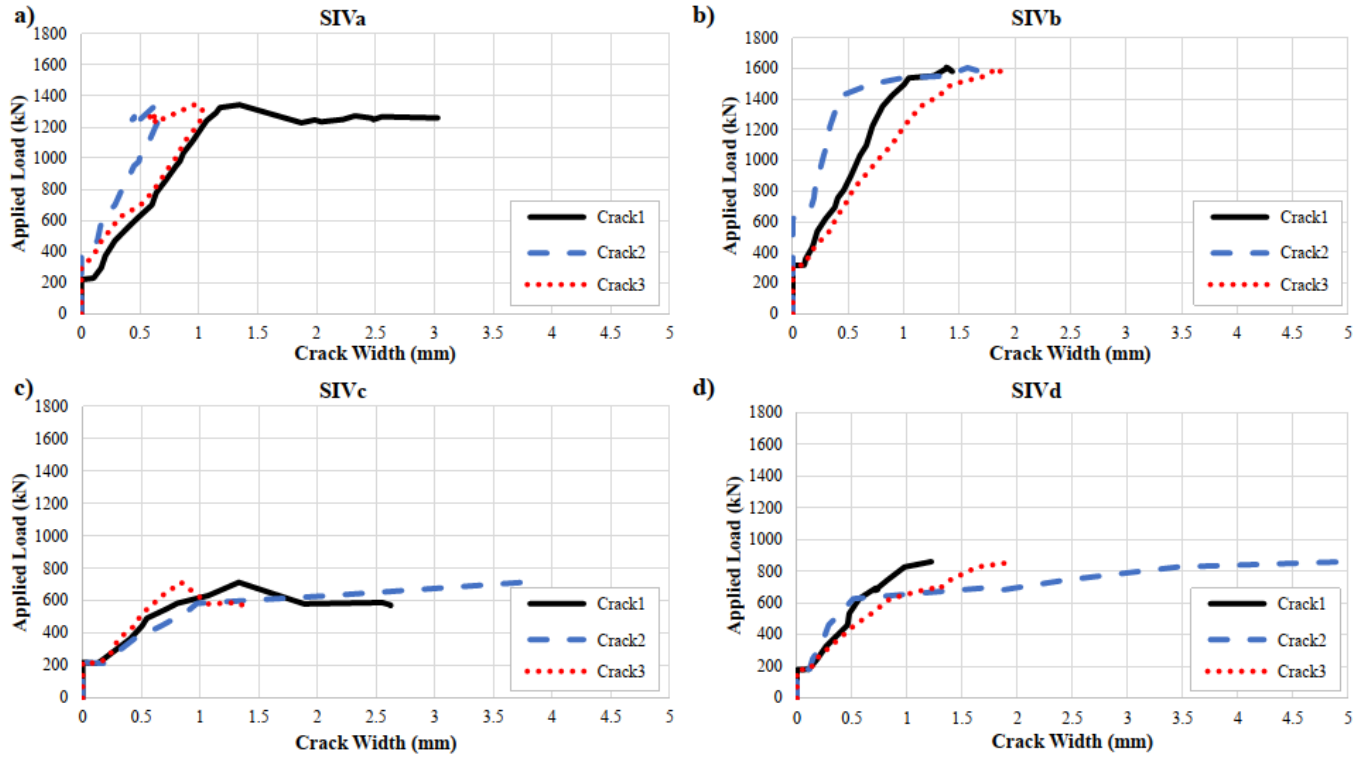

Figure 12 - Evolution of crack width captured via DIC: a) S IVa; b) SIVb; c) SIVc; and d) SIVd.

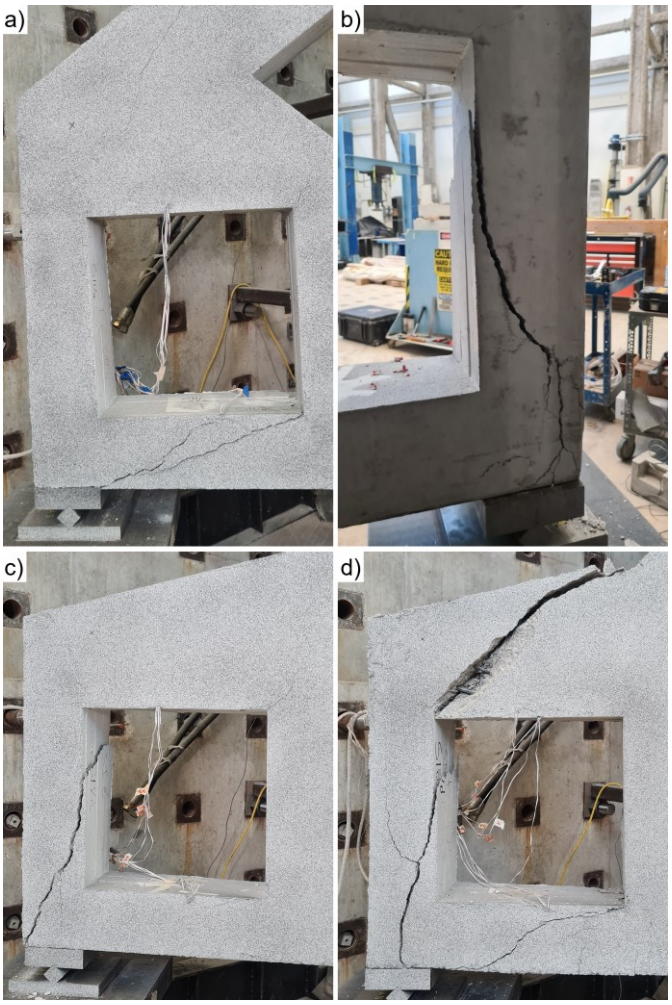

Figure 13 – Photograph of the specimens after the completion of the tests: a) SIVa; b) SIVb; c) SIVc; and d) SIVd.

Table 4 - Comparison of numerical predictions and experimental results for the ultimate load.

Sp.	P_u EXP (kN)	P_u FEA (kN)	Deviation (%)
SIVa	1344	1374	2.2%
SIVb	1616	1504	-7.0%
SIVc	714	713	-0.2%
SIVd	874	863	-1.2%

Figure 15 presents the tensile damage plot, obtained through numerical predictions, for the four specimens under study. This plot provides valuable information that can be correlated with the observed crack patterns. Notably, the predicted crack pattern demonstrates good agreement with the experimental results depicted in Figure 11. The simulations accurately captured the main and widest cracks observed in the experiments. However, the narrower cracks observed on the right side of SIVc and SIVd, as detected by DIC (Figure 11), were not evident in the corresponding predicted tensile damage plot (Figure 15).

Furthermore, Figure 16 showcases the stress field plots also obtained through FEA. The compression fields within the concrete are represented by blue vectors, while the stress distribution on the reinforcement bars is visualized using a scale provided in the figure. Notably, these plots revealed pronounced stress concentrations in the reinforcement cage located above the square opening in specimens SIVc and SIVd. The lower levels of tensile stress observed in the horizontal reinforcement bars, which connect the supports of the specimens, align with the reduced levels of cracking revealed in Figures 11 and 15.

The applied load *vs.* rebar strain curves for all four studied specimens in five different positions are depicted in Figures 17 and 18, obtained through experimental tests and numerical simulations. Figure 17 illustrates the results of five strain gauge positions for both SIVa and SIVb specimens. In contrast, Figure 18 incorporates just four strain gauge positions for both SIVc and SIVd, as SIVc lacks diagonal reinforcement above the square opening (S2 position), and the strain gauges attached to the reinforcement bars at the S1 position in SIVd yielded defective results. The agreements between numerical simulations are evident in both figures, with notable strain predictions for positions S1, S2, and S4 in SIVa and SIVb. Remarkable strain predictions for positions S3, S4, and S5 in SIVc and SIVd were also revealed in Figure 18. Considering the complexity of the structural behavior of the optimized deep beams under study, the employed numerical simulations strategy proves suitable for predicting important design parameters such as load *vs.* deflection, cracking patterns, and strain developed in the reinforcement bars.

Table 5 provides a comprehensive comparison of experimental results from Series I, II, and IV, with Series I and III results extracted from [7,19], respectively. The volume of concrete (V_{conc}) employed in each specimen, reflecting the use or absence of Topology Optimization, is presented in Table 5. Specimens SIa, SIIIa, and SIIIb, extracted from Silveira et al. [7,19], were designed without the application of TO, resulting in a concrete volume of 1.27m³. Conversely, the specimens investigated in this research were designed with the aid of topology optimization, resulting in smaller concrete volumes compared to SIa, SIIIa, and SIIIb. Furthermore, the table showcases the utilization of η_{adm} within the GTM approach, with the notable exception of SIa, which was designed using the Strut-and-Tie Method. Additionally, the table includes the total weight of the reinforcement cage (W_{reinf}) employed in each specimen and the experimental results for the Ultimate Load (P_u).

Three performance ratios are also provided in the table. The first ratio measures the efficiency of the designed reinforcement cage by comparing the Ultimate Load (P_u) obtained in the experimental test with the total weight (W_{reinf}) of the reinforcement cage. The second ratio evaluates the efficiency of the employed volume of concrete (V_{conc}) by relating the Ultimate Load (P_u) to the volume of concrete utilized in each specimen. Lastly, the third ratio assesses the yielding capacity of the specimens by comparing the maximum deflection observed during the experimental test with the deflection at which reinforcement yielding was initially noticeable (δ_u/δ_y). Both deflections were measured from the experimental test at the left LVDT position (refer to Figure 8). Additionally, Table 5 includes the maximum crack width exhibited by each specimen.

Among all the specimens from Series I, III, and IV, SIa [7] exhibited the highest Ultimate Load (P_u) of 1832 kN. The same specimens also performed the lowest ductility ratio (δ_u/δ_y) of 1.7 and also the lowest maximum crack width of 1.4mm. Notably, specimen SIIIa, designed without topology optimization and with a η_{adm} value of 0.5, demonstrated the best reinforcement efficiency, achieving 14.3 kN per kilogram of the reinforcement bar. Additionally, SIIIa [19] showcased the highest yielding capacity, with a ductility ratio (δ_u/δ_y) of 11.0. On the other hand, the specimen SIVb, designed with a topology optimization mass target of 70% and η_{adm} of 0.7, displayed the highest concrete efficiency, reaching 1865 kN per cubic meter of concrete. Specimen SIVc displayed the lowest performance in terms of both reinforcement and concrete efficiencies, with values of 7.3 kN per kilogram of reinforcement bars and 1030 kN per cubic meter of concrete. Lastly, the widest crack was observed in the specimen designed with a topology optimization mass target of 55% and η_{adm} of 0.7, measuring 5.0 mm in width. All the values presented in Table 5 are visualized through a Parallel Coordinate Plot, depicted in Figure 19. This type of plot offers several benefits, including the ability to effectively compare and analyze multiple variables simultaneously, enabling the identification of patterns, trends, and relationships among the different parameters.

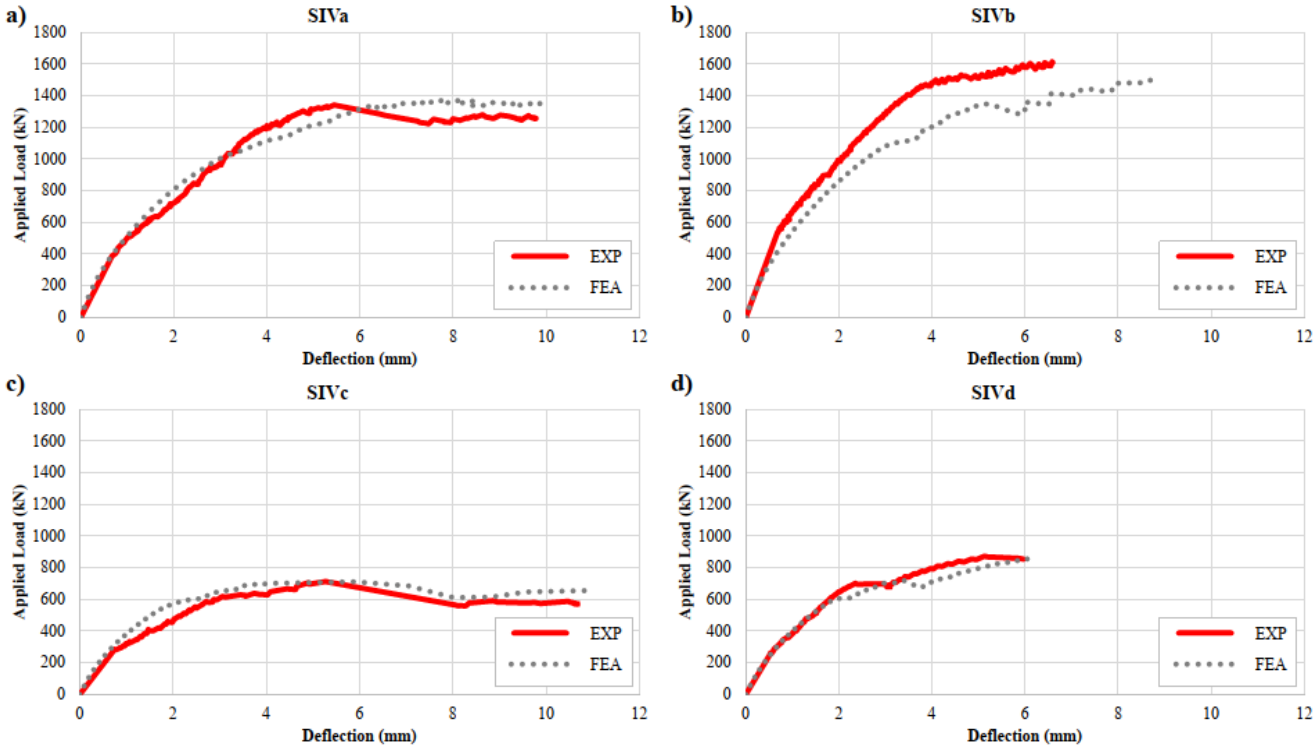

Figure 14 - Applied load *vs.* deflection curves for both experimental and numerical results: a) SIVa; b) SIVb; c) SIVc; and d) SIVd.

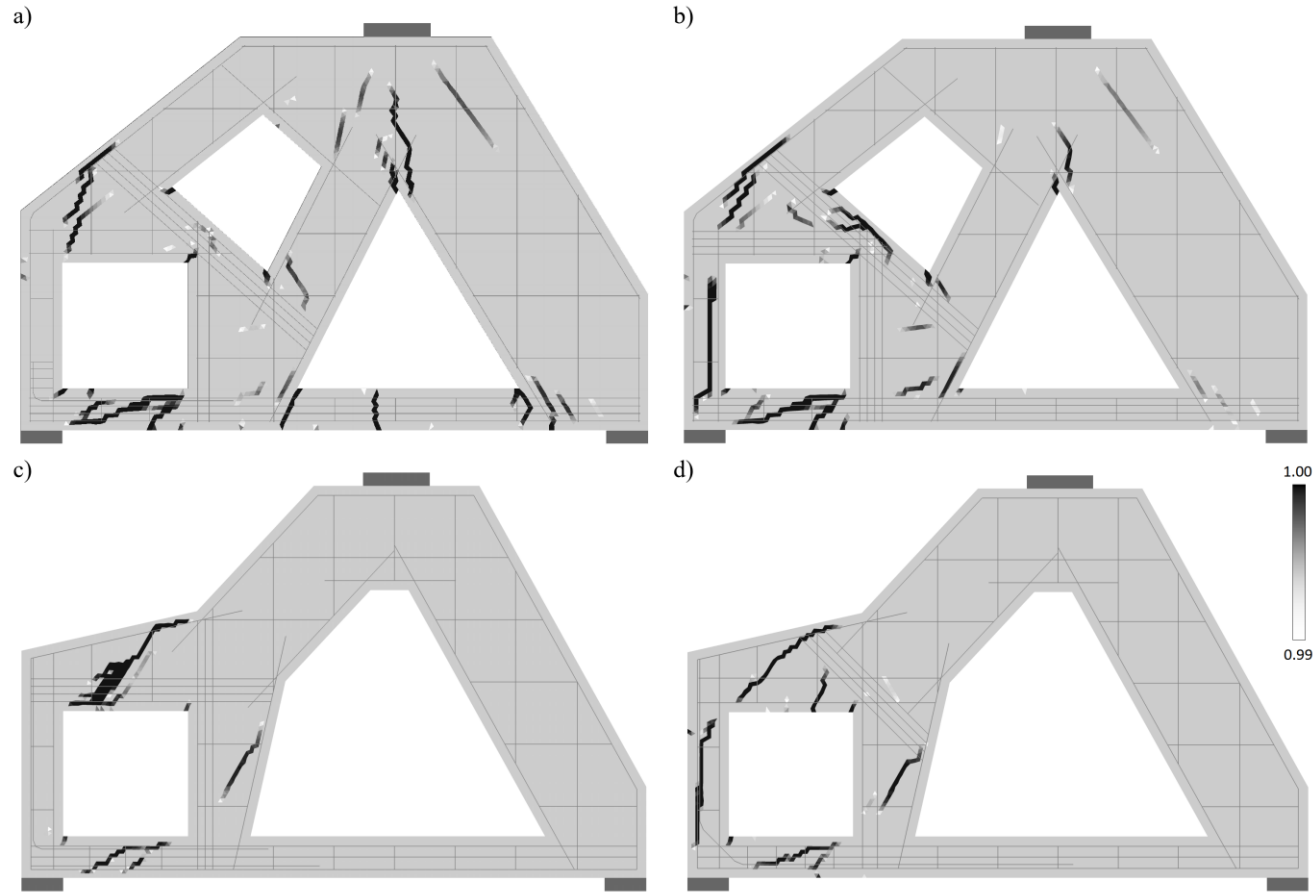

Figure 15 – Tensile damage plot using FEA: a) SIVa; b) SIVb; c) SIVc; and d) SIVd.

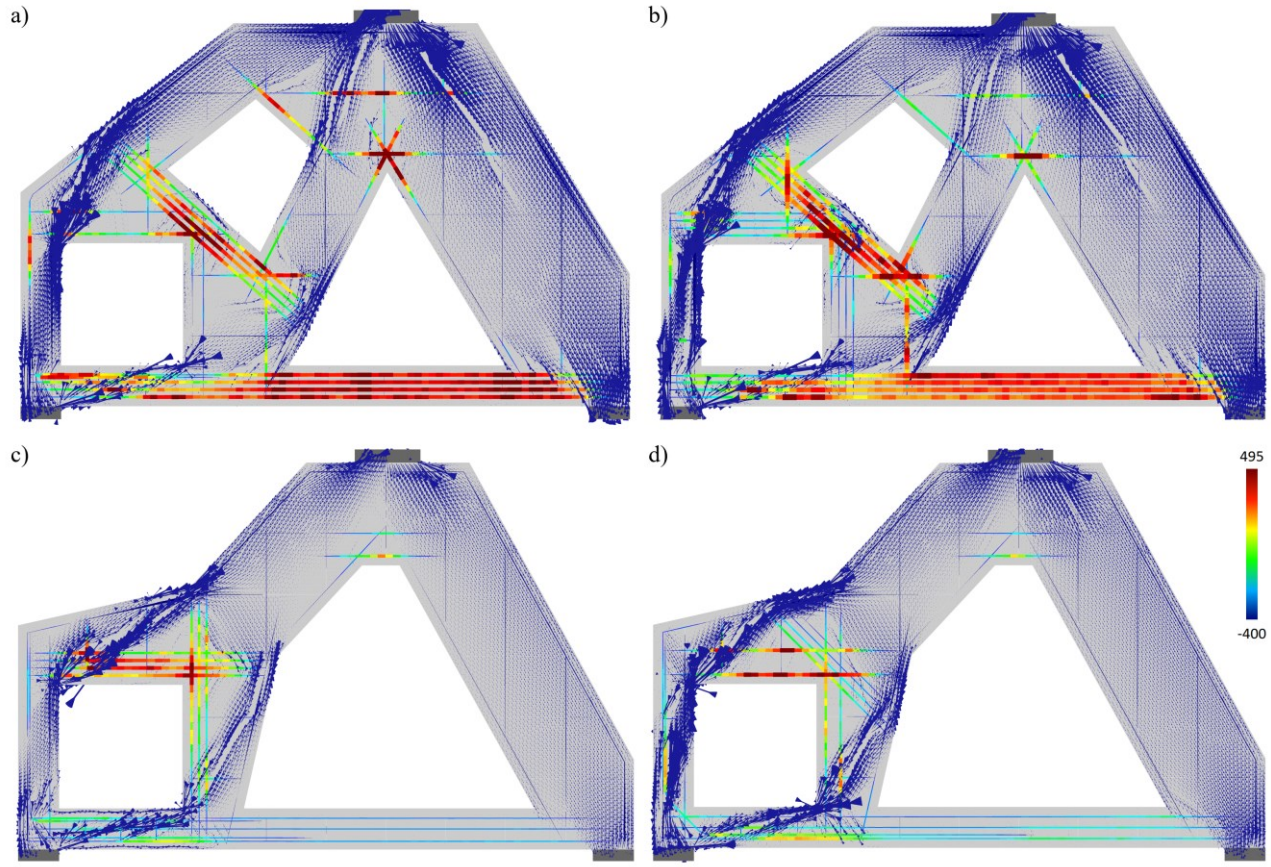

Figure 16 - Stress fields plot using FEA: a) SIVa; b) SIVb; c) SIVc; and d) SIVd.

6. Conclusions

This research paper investigates the design of a classical deep beam employing a generative design framework, which integrates Topology Optimization and the Generative Tie Method. This comprehensive investigation has provided insights into the optimization strategies of reinforced concrete deep beams by applying computational simulations based on Finite Element Analysis and rigorous large-scale experimental testing methodologies. The key findings of this study can be summarized as follows:

1. All four large-scale specimens consistently revealed significant reinforcement yielding and notable ductility, with δ_u/δ_y ratios exceeding 2. The specimens SIVa and SIVc, designed with a η_{adm} of 0.5, displayed considerably higher levels of ductility, with δ_u/δ_y ratios of 5.6 and 3.7, respectively. In contrast, the specimens SIVb and SIVd, designed with a η_{adm} of 0.7, exhibited lower ductility ratios of 3.2 and 2.7, respectively. Refer to Table 5, Figures 10, and 19. Hence, in the context of this specific deep beam configuration, employing a η_{adm} value of 0.5 in the GTM showcased a notable enhancement in terms of ductility performance.
2. The specimen SIVb demonstrated the highest ultimate load capacity among the four large-scale specimens, reaching 1616 kN. Remarkably, despite employing the highest amount of reinforcement, SIVb exhibited the maximum P_u/W_{reinf} and P_u/V_{conc} ratios, measuring 14 kN/kg and 1865 kN/m³, respectively. This observation highlights the effective use of materials employed on SIVb, resulting in optimal structural performance and emphasizing the importance of employing generative design principles when designing complex elements to achieve optimal performance and efficient material usage.
3. The experimental results reveal that specimens SIVa and SIVb (TO target mass of 70%) exhibited the lowest cracking levels under the ultimate load, with maximum crack widths of 3.0 mm and 1.9 mm, respectively. Furthermore, the specimens SIVc and SIVd (TO target mass of 55%) demonstrated the highest cracking levels showing maximum crack widths of 3.7 mm and 5.0 mm, respectively. The location of the widest cracks varies between the two groups of specimens. The specimens SIVc and SIVd (55%) displayed the widest cracks at the crack2 position. Whereas SIVa exhibited the widest crack at the crack1 position, and SIVb demonstrated significant cracking at both the crack1 and crack3 positions. Consequently, the shape optimization process plays a crucial role in determining the final performance of this type of deep beam, influencing factors such as cracking location and intensity, and hence stress distribution (Figure 16).
4. Overall, the numerical and experimental results obtained are in close agreement, particularly concerning the prediction of rebar strains presented in Figures 17 and 18, along with the load-displacement curves depicted in Figure 14. This highlights the effectiveness of the employed FEA strategy as a valuable tool in the design of optimized deep beams within the proposed generative design framework. The parallel coordinate plot presented in Figure 19, obtained from experimental results, can be alternatively obtained during the design stage through FE simulations, facilitating the decision-making process for structural designers.
5. The comparative assessment between the specimens investigated in this study and those examined in two other research papers [7,19], as illustrated in Figure 19 and Table 5, demonstrates the superior performance of the GTM-designed specimens in comparison to the specimen designed using the Strut-and-Tie method (SIa) [7]. The specimen designed using the Strut-and-Tie method, SIa, deserves special attention among all the examined specimens (Series I, III, and IV), as it exhibited a significantly low ductility ratio of 1.7. These observations indicate that the GTM functions as an effective tool for designing deep beams of this type, regardless of whether they incorporate Topology Optimization to optimize their shapes or not.

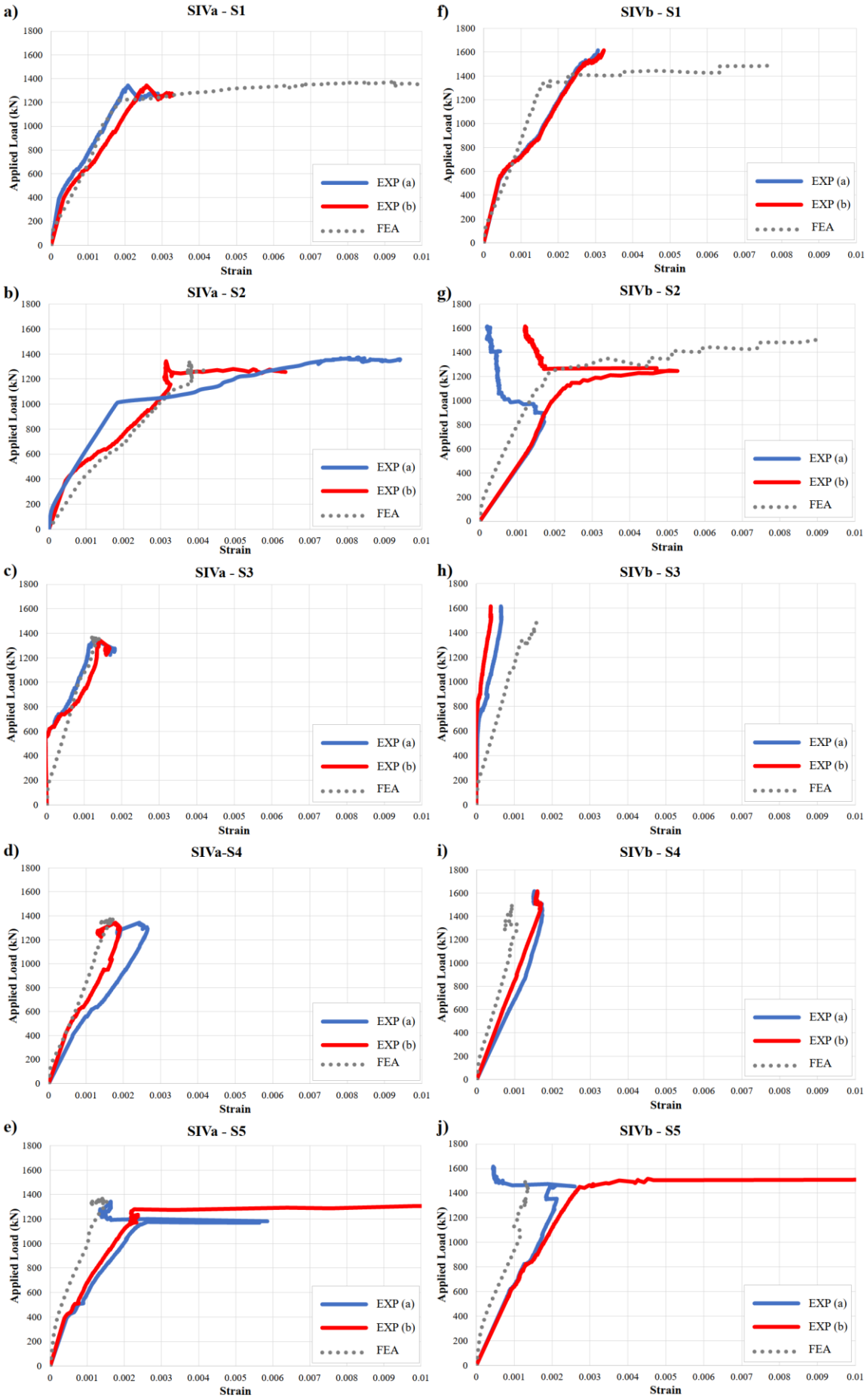

Figure 17 – Applied load *vs.* rebar strain curves obtained through experimental tests and numerical simulations for: a) Specimen SIVa at S1 position; b) Specimen SIVa at S2 position; c) Specimen SIVa at S3 position; d) Specimen SIVa at S4 position; e) Specimen SIVa at S5 position; f) Specimen SIVb at S1 position; g) Specimen SIVb at S2 position; h) Specimen SIVb at S3 position; i) Specimen SIVb at S4 position; and j) Specimen SIVb at S5 position.

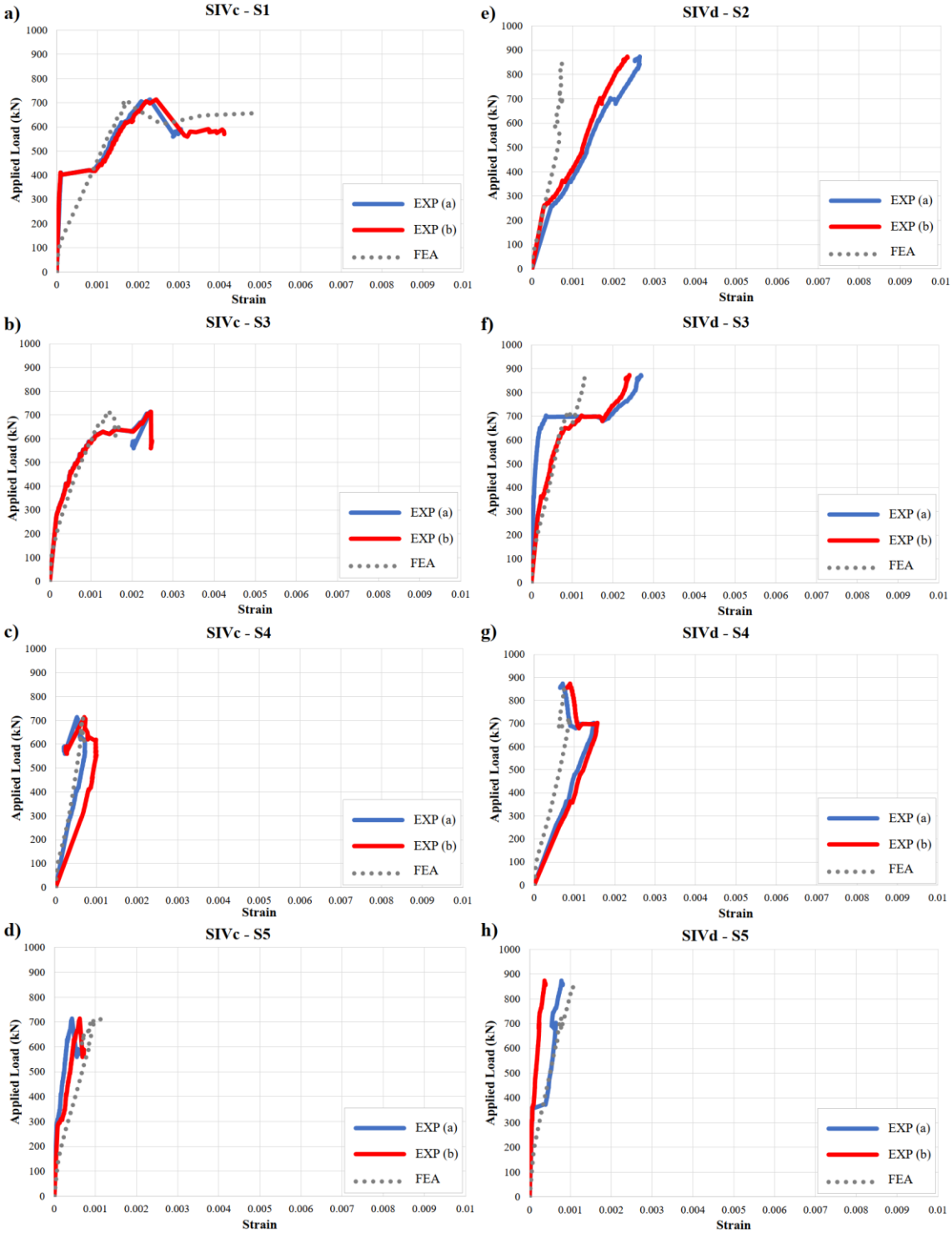

Figure 18 – Applied load vs. rebar strain curves obtained through experimental tests and numerical simulations for: a) Specimen SIVc at S1 position; b) Specimen SIVc at S3 position; c) Specimen SIVc at S4 position; d) Specimen SIVc at S5 position; e) Specimen SIVd at S2 position; f) Specimen SIVd at S3 position; g) Specimen SIVd at S4 position; and h) Specimen SIVd at S5 position.

Table 5 – Comparison between experimental results from Series I, II, and IV. Series I and III results were extracted from Silveira et al. [7,19], respectively.

Sp.	V_{conc} (m³)	η_{adm}	W_{reinf} (kg)	P_u (kN)	$\frac{P_u}{W_{reinf}}$ $\left(\frac{kN}{kg}\right)$	$\frac{P_u}{V_{conc}}$ $\left(\frac{kN}{m^3}\right)$	$\frac{\delta_u}{\delta_y}$	Max. Crack width (mm)
SIa	1.27	-	134.3	1832	13.6	1445	1.7	1.4
SIIIa	1.27	0.5	117.1	1678	14.3	1324	11.0	3.6
SIIIb	1.27	0.7	144.5	1984	13.7	1566	3.7	1.6
SIVa	0.87	0.5	101.7	1344	13.2	1550	5.6	3.0
SIVb	0.87	0.7	115.2	1616	14.0	1865	3.2	1.9
SIVc	0.69	0.5	98.4	714	7.3	1030	3.7	3.7
SIVd	0.69	0.7	103.9	874	8.4	1260	2.7	5.0

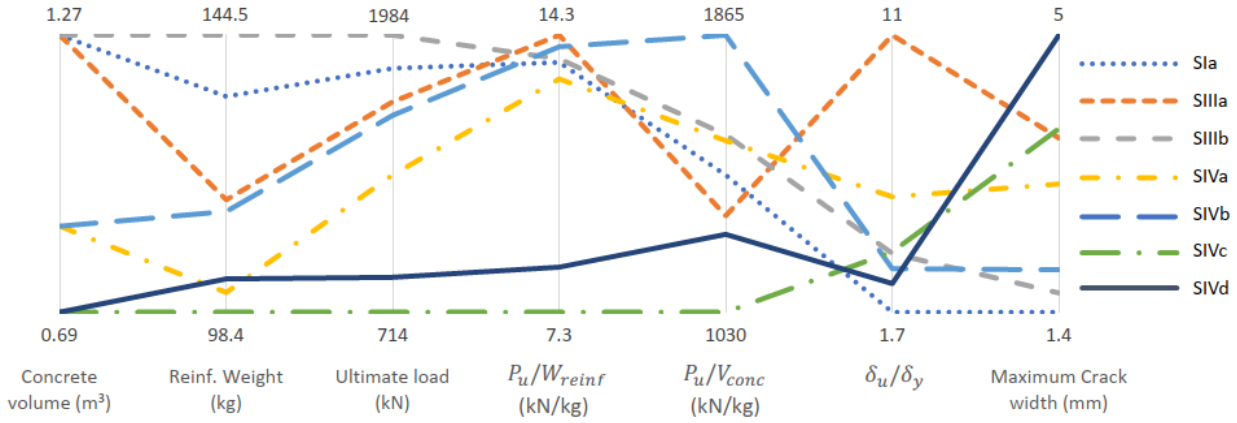

Figure 19 – Parallel coordinate plot for Series I, II, and IV of specimens.

6. The generative design framework presented in this research (Figure 1) has demonstrated promising outcomes, mainly through the integration of Topology Optimization and the Generative Tie Method. By integrating TO for minimizing material wastage with the GTM to generate optimal reinforcement layouts based on FEA, this framework offers a significant opportunity to streamline the decision-making process for structural designers. The balance achieved through this integrated approach allows designers to efficiently address the challenges associated with the design of complex-shaped SC members.

Furthermore, the authors envision that integrating prestressed strands and post-tensioned tendons into the Generative Tie Method holds significant potential for enhancing the design possibilities of complex SC components. Additionally, the applicability of the GTM should be extended to the design of other SC members with discontinuous regions, such as corbels, pile caps, beam-column joints, frame corners, and unconventional shapes obtained through optimization techniques.

7. Acknowledgments

The authors would like to express their gratitude to the Emerging Leaders in the Americas Program (ELAP) for providing Mr. Marcos V. G. Silveira with a scholarship for this research. In addition, the study received partial financial support from the Coordenação de Aperfeiçoamento de Pessoal de Nível Superior – Brasil (CAPES) – Finance Code 001. The experimental work was made possible with the generous support of NSERC through Dr. Sreekanta Das. Dr. Luís A.G. Bitencourt Jr. would like to acknowledge the financial support of the National Council for Scientific and Technological Development – CNPq (Proc. N°: 307175/2022-7). The authors also appreciate the assistance provided by the Structural Engineering Laboratory technical staff members, Mr. Matthew St. Louis and Mr. Jerome Finnerty. Finally, the authors wish to express their gratitude to Autodesk, Inc. for providing the license for Revit® and Fusion360 software.

8. References

[1] J. Schlaich, K. Schaefer, M. Jennewein, Toward a Consistent Design of Structural Concrete, PCI Journal. (1987). https://doi.org/10.15554/pcij.05011987.74.150.

[2] Canadian Standards Association, Design of Concrete Structures CSA A23.3-19, 2019.

[3] American Concrete Institute, 318-19 Building Code Requirements for Structural Concrete and Commentary, American Concrete Institute, 2019. https://doi.org/10.14359/51716937.

[4] Federation internationale du beton fib, fib Model Code for Concrete Structures 2010, Ernst & Sohn, 2013.

[5] Z. Zhang, T. Yarlagadda, Y. Zheng, L. Jiang, A. Usmani, Isogeometric analysis-based design of post-tensioned concrete beam towards construction-oriented topology optimization, Structural and Multidisciplinary Optimization. 64 (2021) 4237–4253. https://doi.org/10.1007/s00158-021-03058-z.

[6] Q.Q. Liang, Y.M. Xie, G.P. Steven, Topology Optimization of Strut-and-Tie Models in Reinforced Concrete Structures Using an Evolutionary Procedure, ACI Struct J. 97 (2000). https://doi.org/10.14359/863.

[7] M.V.G. Silveira, L.A.G. Bitencourt, S. Das, A performance-based optimization framework applied to a classical STM-designed deep beam, Structures. 41 (2022) 488–500. https://doi.org/10.1016/j.istruc.2022.05.035.

[8] H.E. Fairclough, L. He, T.J. Pritchard, M. Gilbert, LayOpt: an educational web-app for truss layout optimization, Structural and Multidisciplinary Optimization. 64 (2021) 2805–2823. https://doi.org/10.1007/s00158-021-03009-8.

[9] H.E. Fairclough, T.J. Pritchard, L. He, M. Gilbert, LayOpt: A truss layout optimization web application, (2020). https://www.layopt.com (accessed June 9, 2023).

[10] X. Yan, D. Bao, Y. Zhou, Y. Xie, T. Cui, Detail control strategies for topology optimization in architectural design and development, Frontiers of Architectural Research. 11 (2022) 340–356. https://doi.org/10.1016/j.foar.2021.11.001.

[11] S.L. Vatanabe, T.N. Lippi, C.R. de Lima, G.H. Paulino, E.C.N. Silva, Topology optimization with manufacturing constraints: A unified projection-based approach, Advances in Engineering Software. 100 (2016) 97–112. https://doi.org/10.1016/j.advengsoft.2016.07.002.

[12] T. Zegard, G.H. Paulino, GRAND3 — Ground structure based topology optimization for arbitrary 3D domains using MATLAB, Structural and Multidisciplinary Optimization. 52 (2015) 1161–1184. https://doi.org/10.1007/s00158-015-1284-2.

[13] T. Zegard, G.H. Paulino, Bridging topology optimization and additive manufacturing, Structural and Multidisciplinary Optimization. 53 (2016) 175–192. https://doi.org/10.1007/s00158-015-1274-4.

[14] L.L. Beghini, A. Beghini, N. Katz, W.F. Baker, G.H. Paulino, Connecting architecture and engineering through structural topology optimization, Eng Struct. 59 (2014) 716–726. https://doi.org/10.1016/j.engstruct.2013.10.032.

[15] Q.Q. Liang, B. Uy, G.P. Steven, Performance-based optimization for strut-tie modeling of structural concrete, Journal of Structural Engineering. (2002). https://doi.org/10.1061/(ASCE)0733-9445(2002)128:6(815).

[16] J. Liu, A. Gaynor, S. Chen, Z. Kang, K. Suresh, A. Takezawa, L. Li, J. Kato, J. Tang, C. Wang, L. Cheng, X. Liang, A. To, Current and future trends in topology optimization for additive manufacturing, Structural and Multidisciplinary Optimization. (2018). https://doi.org/10.1007/s00158-018-1994-3.

[17] J.L. Jewett, J. V Carstensen, Topology-optimized design, construction and experimental evaluation of concrete beams, Autom Constr. 102 (2019) 59–67. https://doi.org/https://doi.org/10.1016/j.autcon.2019.02.001.

[18] M.V.G. Silveira, B. Paini, L.A.G. Bitencourt Jr, S. Das, Design and experimental investigation of deep beams based on the Generative Tie Method, Eng Struct. 255 (2022) 113913. https://doi.org/10.1016/j.engstruct.2022.113913.

[19] M.V.G. Silveira, L.A.G. Bitencourt, S. Das, Experimental and numerical investigation of large-scale reinforced concrete deep beams designed with the Generative Tie Method, [Manuscript Submitted for Publication]. (2023).

[20] A. Muttoni, O. Burdet, N. Kostic, M.F. Ruiz, i-concrete project, Systematic Stress Fields Development for Concrete Structures. (n.d.). https://i-concrete.epfl.ch/ (accessed June 9, 2023).

[21] M.F. Ruiz, A. Muttoni, On development of suitable stress fields for structural concrete, ACI Struct J. 104 (2007) 495–502. https://doi.org/10.14359/18780.

[22] A. Muttoni, M.F. Ruiz, F. Niketic, Design versus assessment of concrete structures using stress fields and strut-and-tie models, ACI Struct J. 112 (2015) 605–615. https://doi.org/10.14359/51687710.

[23] F.J. Vecchio, M.P. Collins, The Modified Compression-Field Theory for Reinforced Concrete Elements Subjected to Shear, ACI Journal. 83 (1986). https://doi.org/10.14359/10416.

[24] F. Alsakka, A. Haddad, F. Ezzedine, G. Salami, M. Dabaghi, F. Hamzeh, Generative design for more economical and environmentally sustainable reinforced concrete structures, J Clean Prod. 387 (2023). https://doi.org/10.1016/j.jclepro.2022.135829.

[25] S. Krish, A practical generative design method, CAD Computer Aided Design. 43 (2011) 88–100. https://doi.org/10.1016/j.cad.2010.09.009.

[26] J. Frazer, Creative Design and the Generative Evolutionary Paradigm, in: Creative Evolutionary Systems, 2002: pp. 253–274. https://doi.org/10.1016/b978-155860673-9/50047-1.

[27] K. Shea, R. Aish, M. Gourtovaia, Towards integrated performance-driven generative design tools, Autom Constr. 14 (2005) 253–264. https://doi.org/10.1016/j.autcon.2004.07.002.

[28] H. Sun, L. Ma, Generative design by using exploration approaches of reinforcement learning in density-based structural topology optimization, Designs (Basel). 4 (2020) 1–20. https://doi.org/10.3390/designs4020010.

[29] C. Sydora, E. Stroulia, Rule-based compliance checking and generative design for building interiors using BIM, Autom Constr. 120 (2020). https://doi.org/10.1016/j.autcon.2020.103368.

[30] V.J.L. Gan, BIM-based graph data model for automatic generative design of modular buildings, Autom Constr. 134 (2022). https://doi.org/10.1016/j.autcon.2021.104062.

[31] D. Gonzalez-Delgado, P. Jaen-Sola, E. Oterkus, Design and optimization of multi-MW offshore direct-drive wind turbine electrical generator structures using generative design

techniques, Ocean Engineering. 280 (2023). https://doi.org/10.1016/j.oceaneng.2023.114417.

[32] J. Zhang, N. Liu, S. Wang, Generative design and performance optimization of residential buildings based on parametric algorithm, Energy Build. 244 (2021) 111033. https://doi.org/10.1016/j.enbuild.2021.111033.

[33] I. Caetano, L. Santos, A. Leitão, Computational design in architecture: Defining parametric, generative, and algorithmic design, Frontiers of Architectural Research. 9 (2020) 287–300. https://doi.org/10.1016/j.foar.2019.12.008.

[34] Autodesk, Fusion 360 Help | Shape optimization study | Autodesk, (n.d.). https://help.autodesk.com/view/fusion360/ENU/?guid=SIM-SHAPE-OPTIMIZATION (accessed June 9, 2023).

[35] Canadian Standards Association, Carbon steel bars for concrete reinforcement CSA G30.18-09, 2019.

[36] L.A.G. Bitencourt, O.L. Manzoli, Y.T. Trindade, E.A. Rodrigues, D. Dias-da-Costa, Modeling reinforced concrete structures using coupling finite elements for discrete representation of reinforcements, Finite Elements in Analysis and Design. 149 (2018) 32–44. https://doi.org/10.1016/j.finel.2018.06.004.

[37] M. Cervera, J. Oliver, O. Manzoli, A RATE-DEPENDENT ISOTROPIC DAMAGE MODEL FOR THE SEISMIC ANALYSIS OF CONCRETE DAMS, Earthq Eng Struct Dyn. 25 (1996) 987–1010. https://doi.org/https://doi.org/10.1002/(SICI)1096-9845(199609)25:9<987::AID-EQE599>3.0.CO;2-X.

[38] L.A.G. Bitencourt, O.L. Manzoli, P.G.C. Prazeres, E.A. Rodrigues, T.N. Bittencourt, A coupling technique for non-matching finite element meshes, Comput Methods Appl Mech Eng. 290 (2015) 19–44. https://doi.org/10.1016/j.cma.2015.02.025.

[39] ASTM International, A370-19e1: Standard Test Methods and Definitions for Mechanical Testing of Steel Products, American Society for Testing and Materials. (2019). https://doi.org/10.1520/A0370-19E01.

[40] ASTM International, C39/C39M-18: Standard Test Method for Compressive Strength of Cylindrical Concrete Specimens, American Society for Testing and Materials. (2018). https://doi.org/10.1520/C0039_C0039M-18.

[41] GOM, GOM Correlate | GOM, (n.d.). https://www.gom.com/3d-software/gom-correlate.html (accessed June 29, 2020).

[42] J. Zohreh Heydariha, S. Das, B. Banting, Effect of grout strength and block size on the performance of masonry beam, Constr Build Mater. 157 (2017) 685–693. https://doi.org/https://doi.org/10.1016/j.conbuildmat.2017.09.130.

[43] D. Corr, M. Accardi, L. Graham-Brady, S. Shah, Digital image correlation analysis of interfacial debonding properties and fracture behavior in concrete, Eng Fract Mech. 74 (2007) 109–121. https://doi.org/https://doi.org/10.1016/j.engfracmech.2006.01.035.

6. General Conclusions

The objective of this Ph.D. research is to develop and evaluate automated-performance-based design methodologies for structural concrete members containing geometric and loading discontinuities. This comprehensive investigation has yielded valuable insights into the optimization strategies for reinforced concrete deep beams, utilizing computational simulations based on FEA and rigorous large-scale experimental testing methodologies. The key findings of this study can be summarized as follows:

1. The proposed method, called Strut-and-Tie Performance-based Optimization, demonstrated notable advantages over existing approaches through the design of specimen SIc. The specimen SIc demonstrated a reduction in material usage while significantly improving structural performance (see Research Paper I). Specimen SIc exhibited a remarkable increase of 14.9% in the relationship between the ultimate load (P_u) and the amount of reinforcement ($W_{reinf.}$) when compared to the STM-designed specimen, SIa.
2. The proposed method, named Generative Tie Method, offers a means of achieving structural concrete members capable of exhibiting ductile failures (refer to Research Paper II). Using FEA results, the GTM increases the area of reinforcement bars within the minimum distributed reinforcement cage to the required amount. This approach ensures the achievement of SC members with the capacity for ductile failure.
3. By manipulating the η_{adm} parameter within GTM, designers gain the capability to establish additional reinforcement positions based on the permissible level of tensile strain in concrete (refer to Research Paper II). This feature enables precise control over the allowable cracking level in a given structural concrete member. As a result, the GTM effectively addresses unique design requirements, particularly in structures exposed to severe environmental conditions where stricter measures for cracking control are imperative.
4. Furthermore, Birrcher et al. [51] performed a comprehensive investigation into the cracking behavior of deep beams within bridge systems. In order to limit crack widths below 0.4 mm under service loads, and thus, they [51] proposed a minimum web reinforcement ratio of 0.3% for deep beams, deviating from the ACI recommendation [1] of 0.25%. Experimental results from Series II indicated maximum crack widths of 0.3 mm (refer to Research Paper II). Hence, the GTM

exhibited the ability to control the cracking levels in deep beams with loading discontinuities, even when adhering to the minimum web reinforcement guideline outlined in ACI 318-19 [1] (0.25%).

5. Specimen SIIIa, designed with a GTM using a η_{adm} value of 0.5, displayed an exceptionally optimized reinforcement layout (see Research Paper III). It achieved the highest P_u/W_{reinf} ratio (14.3) among SIa, SIIIa, and SIIIb specimens while utilizing the least amount of reinforcement (117 kg). The specimen also exhibited notable reinforcement yielding, indicating a ductile behavior. Notably, specimen SIIIa recorded the highest ductility ratio (δ_u/δ_y) of 11.0 among SIa, SIIIa, and SIIIb. These findings highlight the significance of appropriately selecting a suitable η_{adm} value when employing the GTM to design SC deep beams with the capacity to demonstrate ductile failures.
6. Specimen SIIIb showcased remarkable performance in several crucial aspects (see Research Paper III). Firstly, it attained the lowest maximum crack width at the ultimate load (1.6 mm) compared to other examined specimens, SIa and SIIIa. This finding implies that designers can also exercise greater control over acceptable cracking levels in structural elements by selecting the appropriate η_{adm} value when designing deep beams with geometric and loading discontinuities. Additionally, SIIIb achieved the highest ultimate load (1984 kN) among SIa, SIIIa, and SIIIb.
7. All four large-scale specimens from Series IV (designed with TO and GTM) consistently demonstrated significant reinforcement yielding and notable ductility, as evidenced by δ_u/δ_y ratios surpassing 2. Particularly, specimens SIVa and SIVc, designed with a η_{adm} of 0.5, exhibited substantially higher levels of ductility, with δ_u/δ_y ratios of 5.6 and 3.7, respectively. In contrast, specimens SIVb and SIVd, designed with a η_{adm} of 0.7, displayed lower ductility ratios of 3.2 and 2.7, respectively. Therefore, within the context of this specific deep beam configuration, employing a η_{adm} value of 0.5 in the GTM showcased a noteworthy enhancement in terms of ductility performance.
8. Specimen SIVb displayed the highest ultimate load capacity among the Series IV specimens, reaching an impressive 1616 kN (see Research Paper IV). Notably, despite utilizing the greatest amount of reinforcement, SIVb showcased the maximum P_u/W_{reinf} and P_u/V_{conc} ratios, measuring 14 kN/kg and 1865 kN/m³,

respectively. This finding underscores the efficient utilization of materials in SIVb, leading to optimal structural performance. It also emphasizes the significance of employing generative design principles when designing intricate elements to achieve outstanding performance and efficient material usage.

9. Comparisons between Series I, II, and IV specimens revealed that the GTM-designed specimens outperformed the specimen designed using the STM, SIa. Notably, among all the examined specimens (Series I, III, and IV), the specimen designed using the STM, SIa, exhibited the lowest ductility ratio of 1.7. These findings suggest that the GTM is an effective tool for designing deep beams capable of performing ductile failure, regardless of whether TO is used to optimize their shapes or not.
10. The GD framework introduced in this research (see Research Paper IV) has shown promising results by combining TO and GTM. By minimizing material wastage with TO and generating/creating optimal reinforcement layouts based on FEA using GTM, this framework offers a valuable opportunity to simplify the decision-making process for structural designers. The integration of these two techniques enables designers to efficiently address the challenges associated with designing complex-shaped structural concrete members while maintaining a balance between strength and material efficiency.

Furthermore, the authors envision that integrating prestressed strands and post-tensioned tendons into the GTM holds immense potential for enhancing the design possibilities of complex SC components. Moreover, extending the applicability of the GTM to the design of other SC members with discontinuous regions, such as corbels, pile caps, beam-column joints, frame corners, and unconventional shapes obtained through optimization techniques, is crucial. Further investigations are necessary to explore numerical techniques capable of supporting the design process within the GTM and accurately predicting the behavior of SC elements during the post-design stage.

7. References

[1] American Concrete Institute, 318-19 Building Code Requirements for Structural Concrete and Commentary, American Concrete Institute, 2019. https://doi.org/10.14359/51716937.

[2] K.-H. Reineck, Examples for the Design of Structural Concrete with Strut-and-tie Models, American Concrete Institute, 2002. https://books.google.com.br/books?id=795RAAAAMAAJ.

[3] Canadian Standards Association, Design of Concrete Structures CSA A23.3-19, 2019.

[4] Federation internationale du beton fib, fib Model Code for Concrete Structures 2010, Ernst & Sohn, 2013.

[5] Associação Brasileira de Normas Técnicas, ABNT NBR 6118: Projeto de estruturas de concreto - Procedimento, In portuguese, 2014. https://www.abntcatalogo.com.br/norma.aspx?ID=317027.

[6] J. Schlaich, K. Schaefer, M. Jennewein, Toward a Consistent Design of Structural Concrete, PCI Journal. (1987). https://doi.org/10.15554/pcij.05011987.74.150.

[7] B.S. Maxwell, J.E. Breen, Experimental Evaluation of Strut-and-Tie Model Applied to Deep Beam with Opening, ACI Struct J. 97 (2000). https://doi.org/10.14359/843.

[8] B.S. Chen, M.J. Hagenberger, J.E. Breen, Evaluation of Strut-and-Tie Modeling Applied to Dapped Beam with Opening, ACI Struct J. 99 (2002). https://doi.org/10.14359/12113.

[9] M.T. Ley, K.A. Riding, Widianto, S. Bae, J.E. Breen, Experimental Verification of Strut and Tie Model Design Method, ACI Struct J. 104 (2007). https://doi.org/10.14359/18957.

[10] D. Kuchma, Y. Sukit, T. Nagle, J. Hart, H.Hwang. Lee, Experimental Validation of Strut-and-Tie Method for Complex Regions, ACI Struct J. 105 (2008). https://doi.org/10.14359/19941.

[11] K.S. Ismail, M. Guadagnini, K. Pilakoutas, Shear behavior of reinforced concrete deep beams, ACI Struct J. 114 (2017) 87–99. https://doi.org/10.14359/51689151.

[12] L. Zhou, Z. Liu, Z. He, Elastic-to-Plastic Strut-and-Tie Model for Deep Beams, Journal of Bridge Engineering. (2018). https://doi.org/10.1061/(ASCE)BE.1943-5592.0001206.

[13] J.L. Jewett, J. V. Carstensen, Experimental investigation of strut-and-tie layouts in deep RC beams designed with hybrid bi-linear topology optimization, Eng Struct. (2019). https://doi.org/10.1016/j.engstruct.2019.109322.

[14] T.K. Mohammedali, A.M. Jalil, K.S. Abdul-Razzaq, A.H. Mohammed, STM experimental verification for reinforced concrete continuous deep beams, International Journal of Civil Engineering and Technology. 10 (2019) 2227–2239.

[15] H. Chen, L. Wang, J. Zhong, Study on an optimal strut-and-tie model for concrete deep beams, Applied Sciences (Switzerland). 9 (2019). https://doi.org/10.3390/app9173637.

[16] P. Marti, Basic Tools of Reinforced Concrete Beam Design., Journal of the American Concrete Institute. 82 (1985) 46–56. https://doi.org/10.14359/10314.

[17] J. Schlaich, K. Schaefer, Design and detailing of structural concrete using strut-and-tie models, Structural Engineer London. (1991).

[18] T.N. Tjhin, D.A. Kuchma, Computer-Based Tools for Design by Strut-and-Tie Method: Advances and Challenges, ACI Struct J. 99 (2002). https://doi.org/10.14359/12298.

[19] R. Souza, D. Kuchma, J. Park, T. Bittencourt, Adaptable Strut-and-Tie Model for Design and Verification of Four-Pile Caps, ACI Struct J. 106 (2009). https://doi.org/10.14359/56352.

[20] Q.Q. Liang, Y.M. Xie, G.P. Steven, Topology Optimization of Strut-and-Tie Models in Reinforced Concrete Structures Using an Evolutionary Procedure, ACI Struct J. 97 (2000). https://doi.org/10.14359/863.

[21] Z. Zhang, T. Yarlagadda, Y. Zheng, L. Jiang, A. Usmani, Isogeometric analysis-based design of post-tensioned concrete beam towards construction-oriented topology optimization, Structural and Multidisciplinary Optimization. 64 (2021) 4237–4253. https://doi.org/10.1007/s00158-021-03058-z.

[22] Y.M. Xie, G.P. Steven, Technical note a simple approach to Structural Optimization, Comput Struct. 49 (1993) 885–896.

[23] X. Huang, Y.M. Xie, Convergent and mesh-independent solutions for the bi-directional evolutionary structural optimization method, Finite Elements in Analysis and Design. 43 (2007) 1039–1049. https://doi.org/10.1016/j.finel.2007.06.006.

[24] X. Huang, Y.M. Xie, A new look at ESO and BESO optimization methods, Structural and Multidisciplinary Optimization. 35 (2008) 89–92. https://doi.org/10.1007/s00158-007-0140-4.

[25] Q.Q. Liang, B. Uy, G.P. Steven, Performance-based optimization for strut-tie modeling of structural concrete, Journal of Structural Engineering. (2002). https://doi.org/10.1061/(ASCE)0733-9445(2002)128:6(815).

[26] M.F. Ruiz, A. Muttoni, On development of suitable stress fields for structural concrete, ACI Struct J. 104 (2007) 495–502. https://doi.org/10.14359/18780.

[27] A. Muttoni, M.F. Ruiz, F. Niketic, Design versus assessment of concrete structures using stress fields and strut-and-tie models, ACI Struct J. 112 (2015) 605–615. https://doi.org/10.14359/51687710.

[28] D.C. Drucker, On Structural Concrete and the Theorems of Limit Analysis, International Association for Bridge and Structural Engineering (IABSE). (1961) 49–59.

[29] A. Muttoni, J. Schwartz, B. Thürlimann, Design of Concrete Structures with Stress Fields, 1997. https://doi.org/10.1007/978-3-0348-9047-2.

[30] A. Muttoni, O. Burdet, N. Kostic, M.F. Ruiz, i-concrete project, Systematic Stress Fields Development for Concrete Structures. (n.d.). https://i-concrete.epfl.ch/ (accessed June 9, 2023).

[31] F.J. Vecchio, M.P. Collins, The Modified Compression-Field Theory for Reinforced Concrete Elements Subjected to Shear, ACI Journal. 83 (1986). https://doi.org/10.14359/10416.

[32] M.V.G. Silveira, L.A.G. Bitencourt, S. Das, A performance-based optimization framework applied to a classical STM-designed deep beam, Structures. 41 (2022) 488–500. https://doi.org/10.1016/j.istruc.2022.05.035.

[33] H.E. Fairclough, L. He, T.J. Pritchard, M. Gilbert, LayOpt: an educational web-app for truss layout optimization, Structural and Multidisciplinary Optimization. 64 (2021) 2805–2823. https://doi.org/10.1007/s00158-021-03009-8.

[34] H.E. Fairclough, T.J. Pritchard, L. He, M. Gilbert, LayOpt: A truss layout optimization web application, (2020). https://www.layopt.com (accessed June 9, 2023).

[35] X. Yan, D. Bao, Y. Zhou, Y. Xie, T. Cui, Detail control strategies for topology optimization in architectural design and development, Frontiers of Architectural Research. 11 (2022) 340–356. https://doi.org/10.1016/j.foar.2021.11.001.

[36] S.L. Vatanabe, T.N. Lippi, C.R. de Lima, G.H. Paulino, E.C.N. Silva, Topology optimization with manufacturing constraints: A unified projection-based approach, Advances in Engineering Software. 100 (2016) 97–112. https://doi.org/10.1016/j.advengsoft.2016.07.002.

[37] T. Zegard, G.H. Paulino, Bridging topology optimization and additive manufacturing, Structural and Multidisciplinary Optimization. 53 (2016) 175–192. https://doi.org/10.1007/s00158-015-1274-4.

[38] L.L. Beghini, A. Beghini, N. Katz, W.F. Baker, G.H. Paulino, Connecting architecture and engineering through structural topology optimization, Eng Struct. 59 (2014) 716–726. https://doi.org/10.1016/j.engstruct.2013.10.032.

[39] T. Zegard, G.H. Paulino, GRAND3 — Ground structure based topology optimization for arbitrary 3D domains using MATLAB, Structural and Multidisciplinary Optimization. 52 (2015) 1161–1184. https://doi.org/10.1007/s00158-015-1284-2.

[40] F. Alsakka, A. Haddad, F. Ezzedine, G. Salami, M. Dabaghi, F. Hamzeh, Generative design for more economical and environmentally sustainable reinforced concrete structures, J Clean Prod. 387 (2023). https://doi.org/10.1016/j.jclepro.2022.135829.

[41] S. Krish, A practical generative design method, CAD Computer Aided Design. 43 (2011) 88–100. https://doi.org/10.1016/j.cad.2010.09.009.

[42] J. Frazer, Creative Design and the Generative Evolutionary Paradigm, in: Creative Evolutionary Systems, 2002: pp. 253–274. https://doi.org/10.1016/b978-155860673-9/50047-1.

[43] K. Shea, R. Aish, M. Gourtovaia, Towards integrated performance-driven generative design tools, Autom Constr. 14 (2005) 253–264. https://doi.org/10.1016/j.autcon.2004.07.002.

[44] H. Sun, L. Ma, Generative design by using exploration approaches of reinforcement learning in density-based structural topology optimization, Designs (Basel). 4 (2020) 1–20. https://doi.org/10.3390/designs4020010.

[45] C. Sydora, E. Stroulia, Rule-based compliance checking and generative design for building interiors using BIM, Autom Constr. 120 (2020). https://doi.org/10.1016/j.autcon.2020.103368.

[46] V.J.L. Gan, BIM-based graph data model for automatic generative design of modular buildings, Autom Constr. 134 (2022). https://doi.org/10.1016/j.autcon.2021.104062.

[47] D. Gonzalez-Delgado, P. Jaen-Sola, E. Oterkus, Design and optimization of multi-MW offshore direct-drive wind turbine electrical generator structures using generative design techniques, Ocean Engineering. 280 (2023). https://doi.org/10.1016/j.oceaneng.2023.114417.

[48] J. Zhang, N. Liu, S. Wang, Generative design and performance optimization of residential buildings based on parametric algorithm, Energy Build. 244 (2021) 111033. https://doi.org/10.1016/j.enbuild.2021.111033.

[49] I. Caetano, L. Santos, A. Leitão, Computational design in architecture: Defining parametric, generative, and algorithmic design, Frontiers of Architectural Research. 9 (2020) 287–300. https://doi.org/10.1016/j.foar.2019.12.008.

[50] D. Birrcher, R. Tuchscherer, M. Huizinga, O. Bayrak, S. Wood, J. Jirsa, Strength and Serviceability Design of Reinforced Concrete Deep Beams, 2009.

[51] D.B. Birrcher, R.G. Tuchscherer, M. Huizinga, O. Bayrak, Minimum Web Reinforcement in Deep Beams, ACI Struct J. 110 (2013). https://doi.org/10.14359/51684409.

[52] R. Tuchscherer, D. Birrcher, M. Huizinga, O. Bayrak, Distribution of Stirrups across Web of Deep Beams, ACI Struct J. 108 (2011). https://doi.org/10.14359/51664208.

[53] M.V.G. Silveira, B. Paini, L.A.G. Bitencourt Jr, S. Das, Design and experimental investigation of deep beams based on the Generative Tie Method, Eng Struct. 255 (2022) 113913. https://doi.org/10.1016/j.engstruct.2022.113913.